Technical Physics Letters, Vol. 30, No. 12, 2004, pp. 1002–1004. Translated from Pis'ma v Zhurnal Tekhnicheskoĭ Fiziki, Vol. 30, No. 23, 2004, pp. 62–69.

Optical Properties of $(1 - x)PbZn_{1/3}Nb_{2/3}O_3$–$xPbTiO_3$ Single Crystals

L. S. Kamzina[a,*], J. Xu[b], M. Shi[b], and X. Wu[b]

[a] *Ioffe Physicotechnical Institute, Russian Academy of Sciences, St. Petersburg, 194021 Russia*
[b] *Shanghai Institute of Ceramics, Chinese Academy of Sciences, Shanghai, China*
* *e-mail: KAMZIN@AK12758.spb.edu*

Received June 7, 2004

Abstract—The temperature dependence of the optical transmission and small-angle light scattering with and without applied constant electric field was studied in relaxor single crystals of $0.91PbZn_{1/3}Nb_{2/3}O_3$–$0.09PbTiO_3$ (PZN–PT 91/9) and $0.93PbZn_{1/3}Nb_{2/3}O_3$–$0.07PbTiO_3$ (PZN–PT 93/7) solid solutions in the region of two phase transitions: (i) from cubic paraelectric to tetragonal ferroelectric phase at $T = T_c$ and (ii) from tetragonal ferroelectric to rhombohedral ferroelectric phase at $T = T_{rt}$. In the absence of external electric field, only the phase transition at T_c proceeds in both PZN–PT 91/9 and PZN–PT 93/7 crystals according to a percolation mechanism and is accompanied by the appearance of a sharp maximum in the small-angle light scattering intensity curve. In PZN–PT 93/7 crystals, the application of a relatively weak electric field induces an additional percolation-type phase transition at T_{rt}. © *2004 MAIK "Nauka/Interperiodica".*

The physical properties of solids usually exhibit anomalous variation at the interphase boundaries between competitive phases. Typical examples of such behavior are changes in the high-temperature superconductivity and colossal magnetoresistance observed at the metal–insulator interface in metal oxides. Another interesting example is the giant piezoelectric effect observed at the morphotropic phase boundary (MPB) in some Pb-containing ferroelectric materials with perovskitelike structures.

The class of such compounds includes solid solutions of the $(1 - x)PbZn_{1/3}Nb_{2/3}O_3$–$xPbTiO_3$ (PZN–PT) system exhibiting an MPG of the tetragonal ferroelectric order–rhombohedral ferroelectric order type in the vicinity of room temperature. The PZN component possesses a rhombohedral symmetry at room temperature and exhibits a smeared phase transition at ~140°C, while the PT component has a tetragonal symmetry and exhibits the properties of a usual ferroelectric material with long-range order. Solid solutions with the $(1 - x)$PZN–xPT composition are formed for $0 \le x \le 0.2$ and exhibit both relaxor and normal ferroelectric properties [1], with the coefficient of electromechanical coupling at the MPB exceeding 90% and an electric-field induced strain reaching 1.7% [2, 3]. These parameters are about ten times greater than the analogous values in known piezoelectric and electrostrictive ceramics. Such properties are highly attractive from the standpoint of piezoelectric applications, in particular those involving the conversion of electric and magnetic energy into other forms (in medical diagnostic equipment, actuators, high-power ultrasonic transducers, etc.).

In recent years, the nature of the extremely high piezoelectric effects at the MPB has been extensively discussed. This interest is related to the phenomenon of electric-field-induced polarization rotation between the rhombohedral [111] axis and the tetragonal [001] axis via an intermediate state representing either a monoclinic [3] phase or a more complicated state comprising a mixture of orthorhombic and monoclinic phases [4]. It is commonly accepted that the presence of a monoclinic phase is a necessary condition for the giant piezoelectric effect.

In the PZN–PT system under consideration, the most extensively studied and frequently used base composition is PZN–PT 91/9. These compounds are characterized by record values of piezoelectric and electromechanical constants at the MPB and have a Curie temperature of about $T_c \sim 170$–180°C. The morphotropic phase transition from rhombohedral to tetragonal phase is observed at a temperature of $T_{rt} \sim 60$–70°C. However, the piezoelectric constants sharply decrease at temperatures above T_{rt} [5]. In order to obtain PZN–PT crystals with higher T_{rt} values and to expand the working temperature range of applications, it is necessary to reduce the content of titanium ions. Recently, we have grown and characterized such crystals [6]. The obtained PZN–PT crystals exhibited two anomalies in permittivity, which were observed at $T_c \sim 179$°C and $T_{rt} \sim 120$°C.

To our knowledge, the optical properties of PZN–PT crystals have been reported in only a few papers [7, 8] devoted to the domain structure of PZN–PT 91/9. However, optical investigations, including the transmission and small-angle light scattering (SALS) measurements,

are of considerable value for both practical applications and basic science. The results of measurements would provide additional information about the basic properties of the compounds under consideration, since these optical techniques are more sensitive than standard dielectric spectroscopy, especially with respect to evaluation of the dimensions of structural inhomogeneities and their variation in the course of phase transitions. In the case of a phase transition of the percolation type, the average size of clusters of the new phase in the vicinity of the percolation threshold is on the order of a sample size and a large-scale inhomogeneous structure is formed. The phase transition must be accompanied by the appearance of an extremely narrow SALS peak and a minimum in the optical transmission [9].

The aim of our experiments was to study the optical properties of PZN–PT crystals with two compositions: PZN–PT 91/9 and PZN–PT 93/7.

The single crystals of PZN–PT 91/9 and PZN–PT 93/7 were grown using a modified Bridgman method from a melt solution in 50 mol % PbO [6, 10]. The as-grown crystals possessed a rhombohedral symmetry at room temperature and had the maximum dimensions of 30 mm in diameter and 28 mm in length. The single crystal ingots were cut into 1-mm-thick plates oriented perpendicularly to the ⟨001⟩ direction.

During the measurements, an electric field was applied to the samples in the ⟨001⟩ direction while the incident light beam was propagating in the ⟨100⟩ direction. The electric field was applied in the following regimes: cooling in the field (FC) and heating in a zero field after field cooling (ZFHaFC). After application of the field, the samples were depolarized prior to each measurement by heating to a temperature above $T_{\max \varepsilon}$. We have measured the optical transmission and SALS in the transmission geometry [11]. These measurements were performed using He–Ne laser radiation.

Figure 1 shows the temperature dependences of the SALS intensity for a PZN–PT 91/9 sample measured in the cooling and heating modes. As can be seen, the cures exhibit clearly pronounced anomalies and hysteresis in the regions of T_c and T_{rt}. Both phase transitions are of the first order. The hysteresis is much smaller for the high-temperature transition than for the low-temperature one (the hysteresis loop width is ~ 8–10 K at T_c and ~40 K at T_{rt}). Despite a common character of both transitions, there are certain clear distinctions as well. At T_s, narrow peaks in the SALS intensity are observed both in the cooling (at ~170°C) and heating (at ~ 179°C) modes, which are indicative of a percolation character of this phase transition and of the formation of a large-scale inhomogeneous structure in the sample. For the transition from tetragonal to rhombohedral phase at T_{rt}, the SALS intensity shows no such anomalous peak, only a sharp decrease in the intensity.

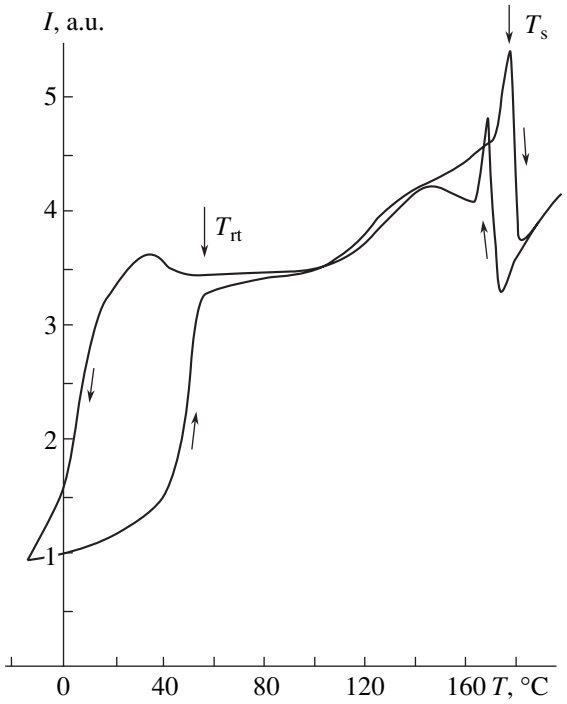

Fig. 1. The temperature dependences of the SALS intensity I for PZN–PT 91/9 crystal measured in the cooling and heating modes (scattering angle, 30′).

This behavior is indicative of the smaller domain size in the rhombohedral phase as compared to that in the tetrahedral phase, where the scattering is still rather high. This evidence of a smaller domain size confirms the assumption made in [1] concerning a microdomain configuration in nonpolarized samples of PZN–PT 91/9 at T_{rt}. The transition at T_{rt} proceeds within a wider temperature interval, the material has a microdomain structure, a percolation cluster is not formed, and the transition does not exhibit a percolation character.

A different pattern was observed in the temperature dependences of the optical transmission and SALS intensity in the PZN–PT 93/7 crystal, which are presented in Fig. 2. The curves exhibit a single anomaly, which is observed at T_s ~ 160 and 178°C in the cooling and heating modes, respectively. The minimum observed in the optical transmission intensity agrees with the position of maximum in the SALS curve. The phase transition in this crystal, as well as that observed in PZN–PT 91/9, possesses a percolation character. The transmission curves measured in both the heating and cooling modes show that the temperature hysteresis width at T_s in these crystals is about 18 K. In the tetragonal phase, the optical transmission between T_s and T_{rt} is very low (the scattering is large) and exhibits no peculiarities (to within the experimental accuracy) upon passage through the T_{rt} point. Apparently, the domain size in the tetragonal and rhombohedral phases is sufficiently large (greater than the light wavelength)

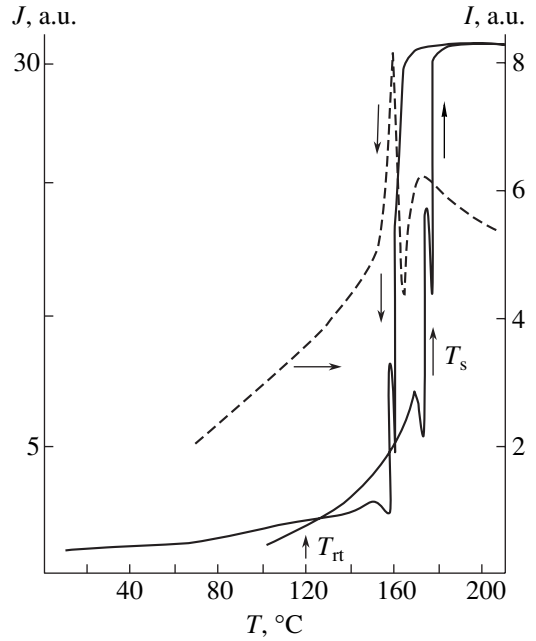

Fig. 2. The temperature dependences of the optical transmission *J* measured in the cooling and heating modes (solid curves) and the SALS intensity *I* (dashed curve) for a PZN–PT 93/7 crystal (scattering angle, 30′).

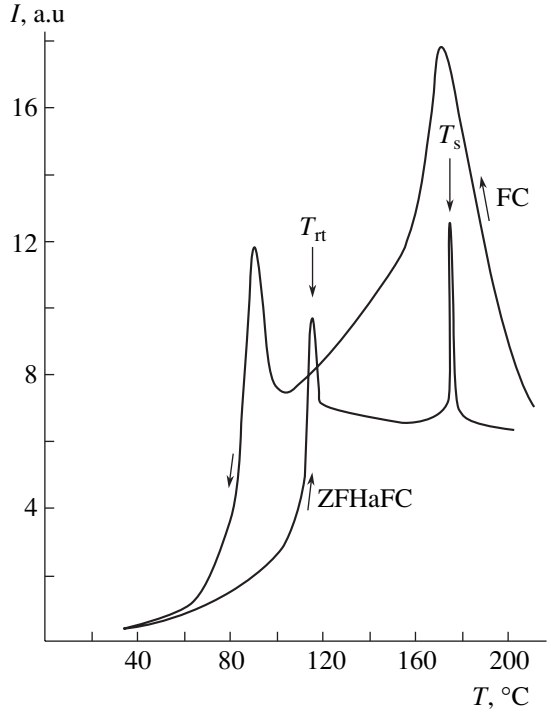

Fig. 3. The temperature dependences of the SALS intensity *I* measured in the FC and ZFHaFC modes for a PZN–PT 93/7 crystal (electric field strength, 2.5 kV/cm; scattering angle, 30′).

and does not significantly change upon the phase transition.

The pattern of light scattering in the PZN–PT 93/7 crystal significantly changes in the presence of an applied electric field. Figure 3 shows the temperature dependences of the SALS intensity in this crystal as measured in the FC and ZFHaFC modes. In the electric field, the SALS intensity exhibits a nearly twofold increase (cf. Figs. 2 and 3), which is evidence of an increase in the domain size. Besides the anomaly at T_s, the SALS curve measured in the field exhibits an additional maximum at T_{rt}, which is evidence of the percolation character of the field-induced transition and of the formation of a large-scale inhomogeneous structure in the sample. The curve measured in the ZFHaFC mode (after cooling the sample in a field of 2.5 kV/cm) also exhibits two clear anomalies at T_{rt} and T_s. As is known [4, 12], the polarization of samples close to the MPB (such as PZN–PT 92/8 and PZT) from high temperatures leads to the formation of a monoclinic phase, which is retained after removal of the applied field, while a tetragonal phase is formed only in strong electric fields. Apparently, our PZN–PT 93/7 crystals studied at very small electric field strengths of 2–3 kV/cm also exhibit the field-induced rhombohedral–monoclinic phase transition of the percolation type. The existence of the irreversible rhombohedral–monoclinic phase transition induced by a weak electric field in the PZN–PT 93/7 crystal suggests that the rhombohedral–monoclinic phase boundary in the phase diagram of nonpolarized $(1 - x)$PZN–xPT samples occurs in the vicinity of $x = 7\%$.

REFERENCES

1. J. Kuwata, K. Uchino, and S. Nomura, Ferroelectrics **37**, 579 (1981).
2. S.-E. Park and T. R. Shrout, J. Appl. Phys. **82**, 1804 (1997).
3. B. Noheda, D. E. Cox, G. Shirane, *et al.*, Phys. Rev. Lett. **86**, 3891 (2001).
4. B. Noheda, Z. Zhong, D. E. Cox, *et al.*, Phys. Rev. B **65**, 224101 (2002).
5. G. Robert, D. Damjanovic, and N. Setter, Ferroelectrics **224**, 97 (1999).
6. J. Khi, J. Tong, M. Shi, *et al.*, J. Cryst. Growth **253**, 274 (2003).
7. Y. Uesu, Y. Yamada, K. Fujishiro, *et al.*, Ferroelectrics **217**, 319 (1998).
8. K. Fujishiro, R. Vlokh, Y. Uesu, *et al.*, Jpn. J. Appl. Phys. **37**, 5246 (1998).
9. L. S. Kamzina and A. L. Korzhenevskiĭ, Pis'ma Zh. Éksp. Teor. Fiz. **50**, 146 (1989) [JETP Lett. **50**, 163 (1989)].
10. J. Xu, S. Fan, B. Lu, *et al.*, Jpn. J. Appl. Phys. **41**, 7000 (2002).
11. L. S. Kamzina, A. L. Korzhenevskiĭ, and O. Yu. Korshunov, Fiz. Tverd. Tela (St. Petersburg) **36**, 479 (1994) [Phys. Solid State **36**, 264 (1994)].
12. R. Guo, L. E. Cross, S. E. Park, *et al.*, Phys. Rev. Lett. **84**, 5423 (2000).

Translated by P. Pozdeev

Technical Physics Letters, Vol. 30, No. 12, 2004, pp. 1005–1008. Translated from Pis'ma v Zhurnal Tekhnicheskoĭ Fiziki, Vol. 30, No. 23, 2004, pp. 70–76.

Ultrasonic Piezoceramic Transducers with a Magnetoacoustic Layer

M. M. Karpuk, D. A. Kostyuk, Yu. A. Kuzavko*, and V. G. Shavrov

Koszalin Technical University, 75-343 Koszalin, Poland
Brest State Technical University, Brest, 224017 Belarus
Institute of Radio Engineering and Electronics, Russian Academy of Sciences, Moscow, 103907 Russia
** e-mail: kuzavko@newmail.ru*

Received May 11, 2004

Abstract—We describe the design and present the results of calculations of the properties of an ultrasonic transducer based on a piezoceramic plate in mechanical contact with a layer of a magnetoacoustic material. The transducer is characterized by strong dependence of the velocities of both transverse and longitudinal waves on the magnetic field. This allows the resonance frequency and the bandwidth to be effectively controlled even in the case of low-Q piezoelectric ceramics and makes it possible to create a tunable frequency standard based on a high-Q piezoelectric material. © *2004 MAIK "Nauka/Interperiodica".*

Introduction. Electromechanical transducers convert electricity into mechanical energy and vice versa. In the range of medium frequencies (1–100 MHz), ultrasonic piezoelectric transducers are used effectively as both sources and detectors of acoustic waves. Using low-Q piezoceramic materials of the RKZ-1 type ($Q \approx 60$), it is possible to obtain short and (with the use of additional matching and damping layers) ultrashort ultrasonic pulses with a duration of $\tau = QT$ (T is the oscillation period). Such signals are widely used, in particular, in systems of nondestructive ultrasonic control and medical echotomoscopy. At the same time, using piezoelectric crystals with high Q ($>10^5$) as electromechanical resonators, it is possible to effectively stabilize the frequency of electric oscillations in radioelectronic equipment. In the case of ultrasonic measurements, it would be very advantageous to provide for the possibility of smooth tuning of the resonance frequency of transmitting and detecting devices [1].

In this paper, we will consider an ultrasonic piezoelectric transducer (UPT) whose substantial topological element is an additional layer made of a so-called magnetoacoustic material (MAM), which is in contact with the piezoelectric layer. By MAM we imply a material characterized by strong dependence of the velocities of both transverse and longitudinal waves on the applied magnetic field **H**. An example is the antiferromagnetic hematite α-Fe_2O_3, for which the experimentally measured decrease in the wave velocity in the vicinity of the orientational phase transition with respect to the magnetic field reaches 10 and 50% for the longitudinal and transverse waves, respectively [2]. This phase transition is observed in the interval of field strengths $0 < H < 2000$ Oe, which is readily achieved using permanent magnets.

Expressions for the velocities of transverse and longitudinal magnetoacoustic waves (MAWs) with allowance for magnetoelastic coupling can be written as [3]

$$\tilde{S}_\mathrm{t} = S_\mathrm{t}(1-\zeta)^{1/2}, \quad \tilde{S}_\mathrm{l} = S_\mathrm{l}(1-t\zeta)^{1/2}, \qquad (1)$$

where $t = S_\mathrm{t}^2/S_\mathrm{l}^2$; $\zeta = 2H_E H_\mathrm{me}[2H_E H_\mathrm{me} + H(H + H_0)]$ is the magnetoelastic coupling parameter; H is the applied magnetic field; and H_E, H_0, H_me are the effective

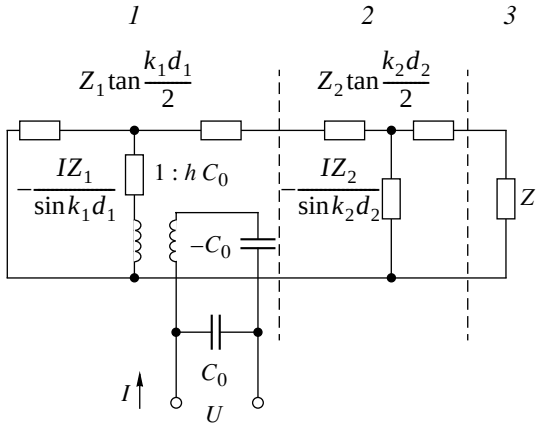

Fig. 1. Equivalent electric circuit of an UPT with a MAM layer, loaded on the medium studied (h is the transformation coefficient): (*1*) piezoelectric element; (*2*) MAM layer; (*3*) object studied (load).

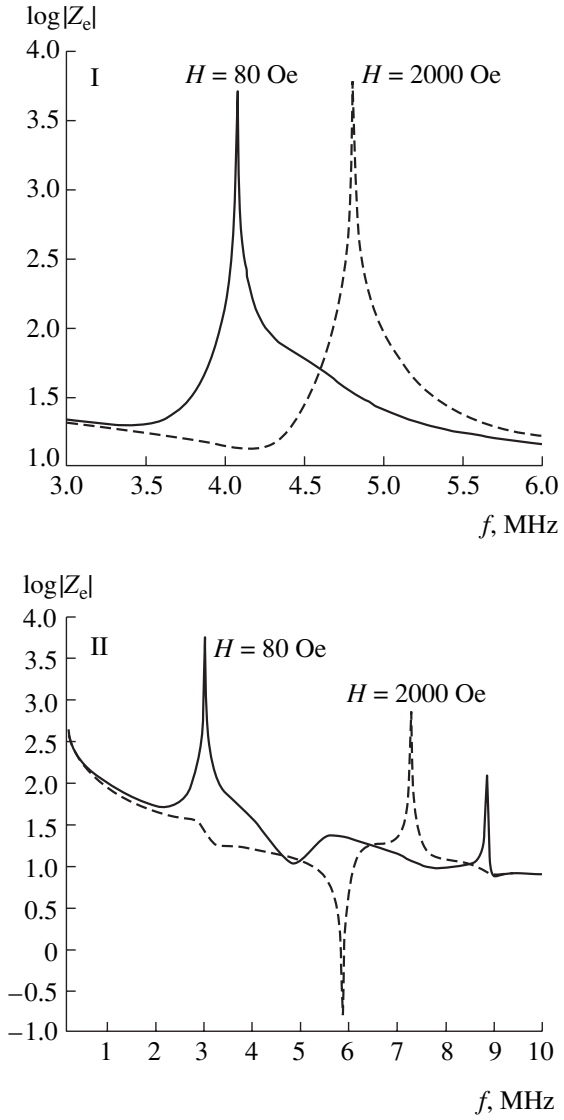

Fig. 2. Plots of the electric impedance $|Z_e|$ versus frequency for an UPT with a MAM layer at various applied magnetic fields H: (I) longitudinal waves; (II) transverse waves.

exchange field, the Dzyaloshinsky field, and the magnetostriction field, respectively [3]. Since the velocities of elastic waves in MAMs depend on the field, the resonance frequency of the layered transducer involving contact between the MAM and piezoelectric layers also becomes field-dependent. Therefore, it is possible to modify the acoustoelectronic parameters of the transducer, including the resonance frequency, bandwidth, amplitude–frequency and phase–frequency characteristics, etc.

Ultrasonic piezoceramic transducer. In order to calculate the characteristics of the proposed UPT with a MAM layer, we use the method of equivalent electric circuit [4] with allowance for a load provided by the medium (Fig. 1). In the case under consideration, an expression for the electric impedance is

$$Z_e = \frac{1}{i\omega C_0}\left[1 - \frac{K^2}{\beta_1} \times \frac{\tan\beta_1 - \frac{Z_2}{2Z_1}\tan 2\beta_2 + i\left(\frac{Z}{Z_2}\tan\beta_1\tan\beta_2 - \frac{Z_0}{2Z_1}\right)}{1 + \frac{Z_2}{Z_1}\cot 2\beta_1\tan 2\beta_2 + i\left(\frac{Z}{Z_2}\tan 2\beta_2 - \frac{Z}{Z_1}\cot 2\beta_1\right)}\right], \quad (2)$$

where $\beta_1 = k_1 d_1/2$, $\beta_2 = k_2 d_2/2$, k is the wavenumber, ω is the circular frequency, C_0 is the UPT capacitance, K is the electromechanical coupling constant, and Z is the acoustic impedance.

The minimum of $\mathrm{Im}\,Z_e$ determines the electric resonance of the UPT (transmission), while its maximum determines the mechanical resonance (detection). The quantities $Z_2 = \rho_2 S_2(H)$ and $\beta_2 = \omega d_2/(2S_2(H))$ depend on the field and, hence, Z_e and the resonance frequencies are also field-dependent. The numerical calculations were performed using a MATLAB program package for longitudinal waves in a ($LiNbO_3$, 36°, *Y*-cut)–(α-Fe_2O_3–SiO_2, 32°, *X*-cut) structure and for transverse waves in a ($LiNbO_3$, 36°, *X*-cut)–(α-Fe_2O_3–SiO_2, 32°, *X*-cut) structure in the frequency range 1–10 MHz. The frequency of the mechanical resonance of the piezoelectric element was 5 MHz, which corresponded to a piezoelectric layer thickness of $d_{1l} = 0.74$ mm and $d_{1t} = 0.48$ mm for the longitudinal and transverse waves, respectively. The thickness of the MAM layer, which also satisfied the condition of the half-wave resonance at the same frequency, was $d_{2l} = 0.68$ mm and $d_{2t} = 0.42$ mm at $H = \infty$ for the longitudinal and transverse waves, respectively.

Figure 2 shows the calculated frequency dependence of the impedance $|Z_e|$, which can be used for determining all the aforementioned acoustoelectronic parameters of the UPZ with a MAM layer. As can be seen, the approach to the orientation phase transition point ($H = 0$) is accompanied by a significant shift of the UPT resonance frequency and by the appearance of new resonances. Using the specially developed program package, it was possible to calculate all the acoustoelectronic parameters of the proposed device.

Frequency stabilizer. If the acoustic impedance Z according to Eq. (2) is zero, the UPT with a MAM layer represents an unloaded transducer. High figure of merit ($Q \geq 10^5$) of the quartz transducers operating as electromechanical resonators allows these devices to perform as stabilizers of the frequency of electric signals. A drift of the resonance frequency relative to a preset value under the action of external factors (temperature, pressure, etc.) can be compensated by changing the mag-

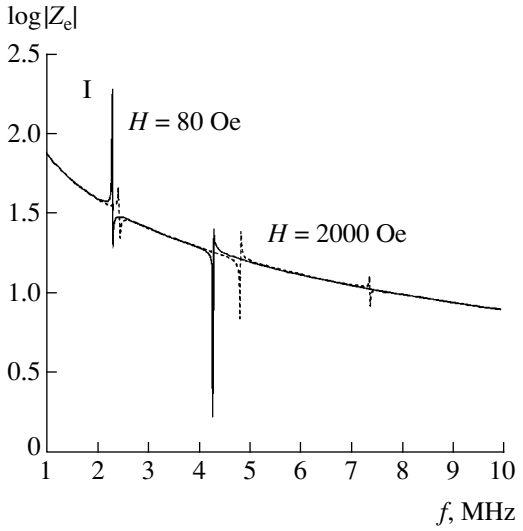

Fig. 3. Plots of the electric impedance $|Z_e|$ versus frequency for a proposed stabilizer at various applied magnetic fields H (longitudinal waves).

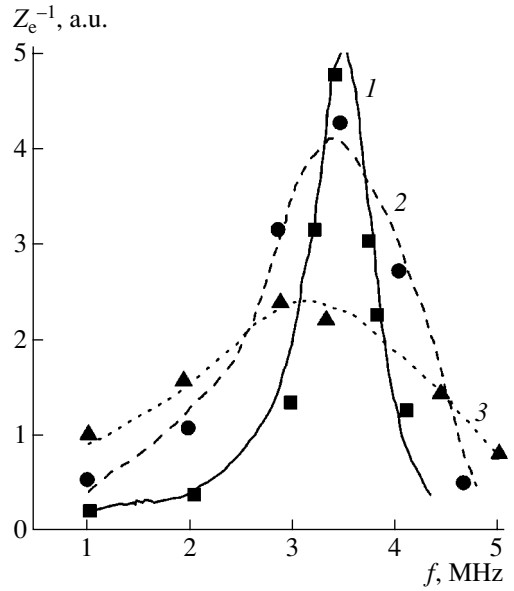

Fig. 4. Amplitude–frequency characteristic of an UPT loaded on water for longitudinal waves at H = 2000 (*1*), 500 (*2*) and 100 Oe (*3*).

netic field. Thus, the proposed scheme of an UPT with a MAM layer allows the frequency to be restored by means of external magnetic field.

Expression (2) was obtained assuming that the absorption of acoustic waves in the UPT materials is negligibly small. In order to take into account a finite absorption of ultrasound in both piezoelectric and MAM layers, it is possible to perform the formal substitution $k_1 \longrightarrow k_1' + ik_1''$ and $k_2 \longrightarrow k_2' + ik_2''$ ($Q_1 = \pi k_1'/k_1''$, $Q_2 = \pi k_2'/k_2''$) in the expression for the electric impedance of the composite UIPT. The coefficient of ultrasound absorption in the MAM layer is determined using the relation $\alpha = k_2''/k_1' = \alpha_0(1 - a\zeta)^{-1/2}$ [3], where $a = 1$ and $a = t$ in the case of transverse and longitudinal waves, respectively.

Figure 3 shows the results of calculations of the frequency dependence of Z_e for a quartz–hematite UPT at various values of the magnetic field **H**. On approaching the point of the orientational phase transition (i.e., upon increasing the MAM layer thickness), the number of resonances increases, in accordance with the dependence $\beta_2 = \dfrac{\omega d_2}{2s_2(H)}$. Thus, by the attachment of the piezoelectric element to a high-Q MAM layer occurring in a magnetic field, it is possible to control the resonance frequency of the transducer, the bandwidth, and other acoustoelectronic parameters.

Experiment. The proposed UPT with a MAM layer was used as a radiator in a medical echotomoscope [5]. It should be noted that ultrasonic tomography predominantly employs longitudinal waves, for which the dependence of the wave velocity in a MAM on the magnetic field is much weaker than for transverse waves [6]. Nevertheless, even in this case the external magnetic field allows the UPT characteristics to be controlled within rather wide limits [7]. Figure 4 shows the typical amplitude–frequency characteristics of the UPT in the detection regime for various values of the magnetic field. By varying the magnetic field, it was possible to control the resonance frequency of the UPT within 20%, while the Q value (and, hence, the working bandwidth) could be changed up to within 70%.

Conclusion. The parameters of the proposed UPT can also be calculated using equations of the theory of elasticity and electrostatics with the corresponding boundary conditions [3]. However, this approach is rather difficult and encounters difficulties in taking into account the presence of additional layers in the transducer structure, since it is necessary to solve the system for all the boundary conditions. The proposed approach based on the method of equivalent electric circuit, being more clear and effective, allows the calculations of the electric impedance and other acoustoelectronic characteristics of the multilayer UPT to be automated using MATLAB program package. By means of the specially developed software, it is possible to determine the acoustoelectronic characteristics of UPTs and frequency stabilizers involving arbitrary piezoelectric elements, MAMs, and other media. This routine can be readily adapted to the description of even more complicated multilayer structures.

Acknowledgments. This study was supported in part by the Foundation for Basic Research of the Republic of Belarus and by the Russian Foundation for

Basic Research (project nos. F04P-080, 04-02-81058, and 03-02-174443).

REFERENCES

1. M. K. Balakirev and I. A. Gilinskiĭ, *Waves in Piezoelectric Crystals* (Nauka, Novosibirsk, 1982) [in Russian].
2. E. A. Andryushchak, N. N. Evtikhiev, S. A. Pogozhev, and V. L. Preobrazhenskiĭ, Akust. Zh. **27**, 170 (1981) [Sov. Phys. Acoust. **27**, 93 (1981)].
3. E. A. Turov and V. G. Shavrov, Usp. Fiz. Nauk **140**, 429 (1983) [Sov. Phys. Usp. **26**, 593 (1983)].
4. G. S. Kino, *Acoustic Waves: Devices, Imaging, and Analog Signal Processing* (Prentice-Hall, Englewood Cliffs, 1987).
5. Yu. A. Kuzavko, V. V. Golovko, and H. Roth, in *Proceedings of the Workshop on Design Methodologies for Signal Processing, Zakopane, 1996*, pp. 131–135.
6. Yu. A. Kuzavko and V. G. Shavrov, Akust. Zh. **39**, 1088 (1993) [Acoust. Phys. **39**, 572 (1993)].
7. M. M. Karpuk and Yu. A. Kuzavko, in *Proceedings of the 7th International Conference on Intermolecular and Magnetic Interactions in Matter, Miedzyzdroje, 2003.*

Translated by P. Pozdeev

Technical Physics Letters, Vol. 30, No. 12, 2004, pp. 1009–1012. Translated from Pis'ma v Zhurnal Tekhnicheskoĭ Fiziki, Vol. 30, No. 23, 2004, pp. 77–84.

The Effect of Surface Waves on the Interaction of Incident Particles with a Solid Surface

M. A. Chertov[a], A. Yu. Smolin[a], G. A. Sapozhnikov[b], and S. G. Psakhie[a]

[a] *Institute of Strength Physics and Materials Science, Siberian Division, Russian Academy of Sciences, Tomsk, 634055 Russia*

[b] *Institute of Theoretical and Applied Mechanics, Siberian Division, Russian Academy of Sciences, Novosibirsk, Russia*

e-mail: maks@usgroups.com; maks@ispms.tsc.ru

Received June 23, 2004

Abstract—The incidence of two particles onto a thin solid plate has been studied by means of computer simulation. The influence of the impact-excited waves on the particle–surface interaction is considered. The waves excited in the target plate produce a significant change in the surface response dynamics. The distribution of surface damage and plastic strain generated by the incident particles is analyzed, and it is established that this distribution is correlated with the surface wave structure. © *2004 MAIK "Nauka/Interperiodica".*

The effects of wave excitations on the process of straining and fracture of solids under dynamical loading conditions are rather difficult to study in experiment because of the dynamic character of such interactions. Recently [1], we numerically modeled the generation of the wave excitation by pulsed impact upon metal plates of various thicknesses. It was established that the impact generates a vortexlike packet of velocities, which retains its structure in the course of subsequent propagation. The configuration of displacements in thin plates is similar to that described by the analytical solution in the form of a Lamb wave, and, in thick plates, in the form of a Rayleigh wave. It was pointed out that such dynamic effects are able to transfer the elastic energy over relatively large distances. The transferred energy can be released at "weak" sites, such as defects and inhomogeneities, which leads to the production and accumulation of damage even at sites remote from the point of impact.

This paper presents the results of an analysis of the effect of surface excitations, caused by the propagation of surface waves, on the response to local impact loading. This problem is of special interest in the context of investigations of the possible mechanisms of superdeep penetration [2] and the formation of highly adhesive hard coatings by means of cold gasdynamic deposition [3]. It is possible to distinguish two main approaches among various explanations of the phenomenon of superdeep penetration. The first is based on the notion of a local loss of the shear strength of the target material as a result of adiabatic heating [4], whereby it is assumed that a self-sustained regime of streamlining of an incident particle may exist and the material surrounding the particle is described in terms of a viscous liquid. In the second approach, emphasis is placed on a local change in the mechanical properties of the target surface [5], whereby the material loses strength as a result of tensile stresses in the lateral direction.

One possible reason for a local decrease in the strength of a target material may be the complex interaction of the surface wave packets [1] with each other and with the projectiles. According to a well-known experimental fact, the adhesive ability increases with the density of the flux of incident particles, which is indicative of an important role of the collective factor in this process. The wave excitation of the surface may also be important in many other processes, for example, in the ultrasonic treatment of materials. And, of course, this kind of surface "mechanoactivation" is also of purely scientific interest.

We consider the problem of the group impact of particles upon a metal plate. The mechanical parameters of both the target plate and the incident particles correspond to aluminum [6]. The interaction was simulated by the method of movable cellular automata (MCA) [7–9].

The velocity of incident particles was directed along the normal to the target surface and set equal to ~200 m/s, so that the energy of impact on the unperturbed surface would be sufficient to generate plastic deformation while not damaging the material. The incident particles were separated in both space and time so that the first particle generated a surface wave and the second particle reached the excited surface region about 17 μs later. Thus, the time between two impacts was fixed, and we varied the distance d between the points of impact to study how the interaction of the second particle with the plate surface changed depending on the mutual arrangement of the propagating surface wave and the projectile.

1063-7850/04/3012-1009$26.00 © 2004 MAIK "Nauka/Interperiodica"

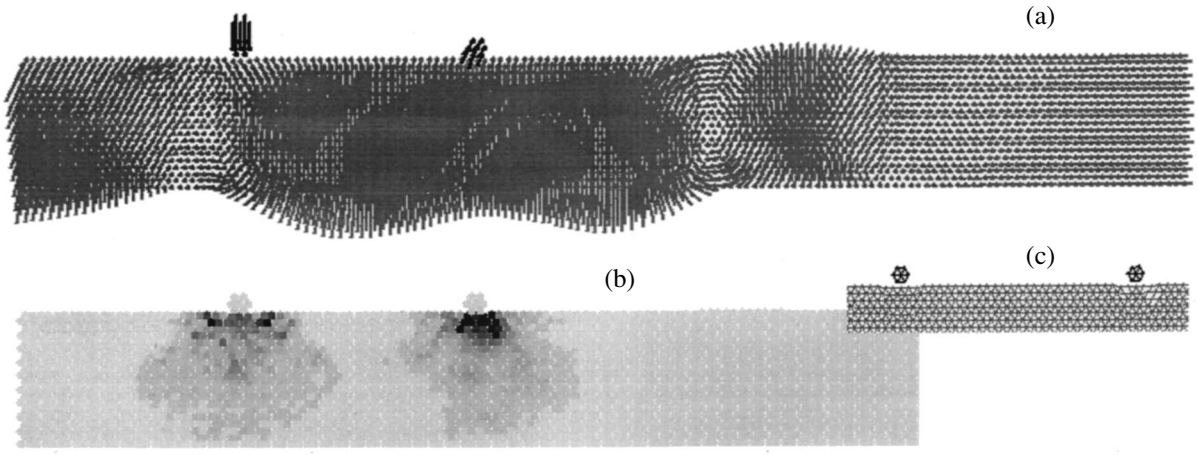

Fig. 1. Patterns of (a) the velocity field, (b) the distribution of plastic work, and (c) the structure of links between automata in the target plate after interaction with two incident particles (32.5 μs after the first impact). The points of impact are spaced by $d = 30$ mm.

The results of the simulation showed that the second impact on the plate in the presence of an elastic surface wave significantly differs from the interaction with the unperturbed target surface. This fact indicates that the dynamic state of the surface may significantly influence both the character and the results of the interaction. In particular, for certain values of d, the second impact may damage the target even for the same velocity of the incident particle.

Figure 1 shows the velocity field, the structure of damage, and the distribution of plastic work upon the rebounding of both particles in the case when the mutual arrangement of the second projectile and the surface wave provides the maximum surface damage. This situation corresponded to $d = 30$ mm. In order to study the efficiency of the impact as a function of the distance between the impact points, it is necessary to analyze the pattern of irreversible changes at the target surface. Initially, this was done in terms of the extent of damage expressed by the number of broken links between automata. However, this characteristic turned out to be inconvenient, because the number of broken links is discrete and changes with a large step. It was found to be more convenient, to use the specific plastic work, which provides an integral characteristic of inelastic straining.

The first particle exhibited rebound strictly along the normal to the surface and left the target ~8.5 μs after arrival. For the second projectile, the surface wave propagating from left to right distorts the symmetry of the stressed state and makes one direction preferred. For this reason, the velocity of the second particle upon rebound significantly deviates from the normal, and the absolute value of this velocity is smaller than that for the first particle. As was pointed out previously [1], the interaction results in the formation and propagation of a vortexlike packet of velocities (Fig. 1a). In this study, it was established that the second impact slightly increases the amplitude of velocities in the initial vortex. Examination of the wave structure at the moment of the second impact at $d = 30$ mm shows that the second particle velocity at the point of impact coincides with the vortex twist direction and, as a result, the second impact increases the vortex energy.

Reduced velocity of the second particle upon rebound, increased inelastic strain, and a greater extent of damage—all these features are indicative of the more inelastic character of the interaction with the excited surface for the given configuration of wave and projectile. In a real experiment, this situation may lead to an increase in the adhesive ability.

Figure 2 shows the case when the second particle is incident at a different site ($d = 43$ mm). Here, the second impact does not produce damage, and the work of inelastic deformation is significantly lower than that in the previous example. The velocity upon rebound also deviates from the normal direction, but the absolute value of this velocity is greater than that for the first particle. Accordingly, the amplitudes of velocities in the initial vortex packet upon the second impact are lower than those in the case considered above. By the same token, we may expect a decrease in the adhesive ability.

Thus, the presence of a surface wave in the target plate leads to a dynamic redistribution of the mechanical response in the plate–particle system, rather than merely strengthening or weakening the particle impact on the target. In order to study the laws of this redistribution, let us plot the values characterizing different variants of the interaction versus the distance d and compare these plots to the plane wave configuration. Such a construction is presented in Fig. 3, where it can be seen that both characteristics—the extent of damage and the plastic work—are quite well correlated with each other and with the velocity distribution in the wave: the maximum damage is localized at the vortex in the velocity field.

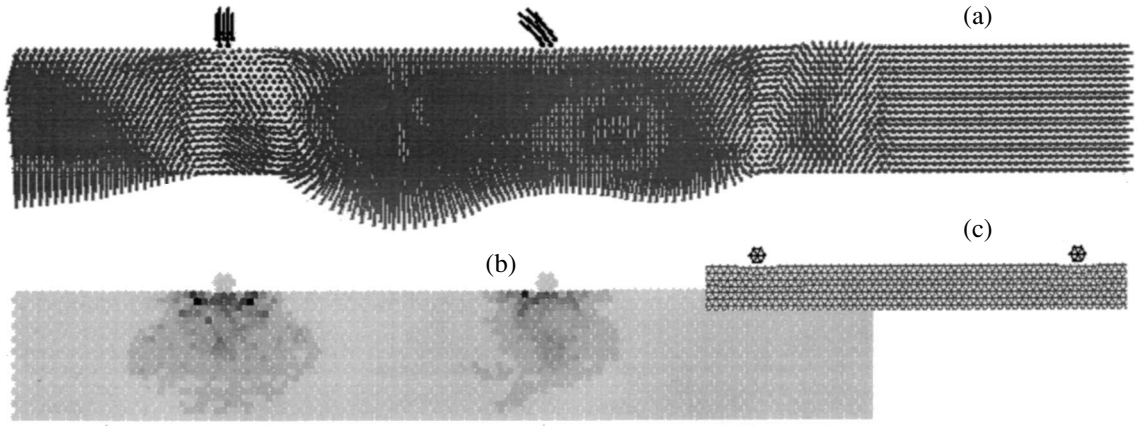

Fig. 2. Patterns of (a) the velocity field, (b) the distribution of plastic work, and (c) the structure of links between automata in the target plate after interaction with two incident particles (32.5 μs after the first impact). The points of impact are spaced by $d = 43$ mm.

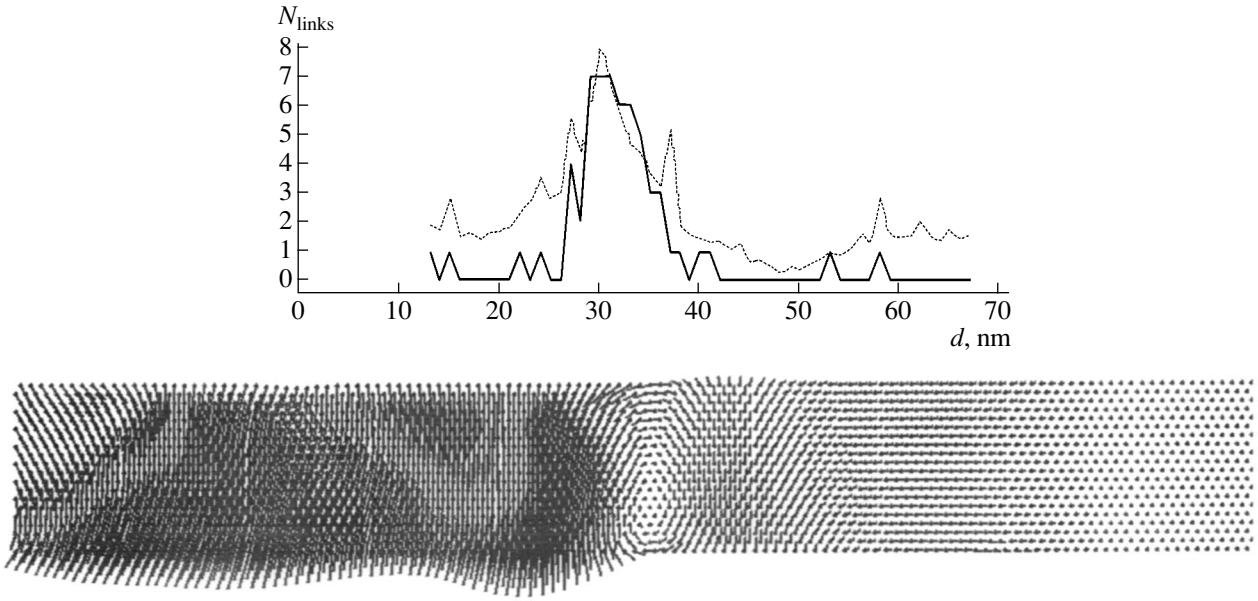

Fig. 3. Plots of the extent of damage (solid curve) and the plastic work (dashed curve) versus the distance between two points of impact in comparison to the surface wave structure.

An analysis of the distribution of strain in the plate showed that, owing to the surface wave, the plate contains a region of tensile stresses directed along the surface. This stressed region propagates from left to right together with the wave, and the maximum damage is observed at the center of this region. It should be noted that this result partly coincides with the data reported in [5], where the presence of tensile stresses was also considered as the main factor of superdeep penetration. However, the appearance of such stresses in [5] was explained by convexity of the particle flux distribution.

In conclusion, the presence of wave excitations significantly modifies the character of the interaction between incident particles and the target surface, depending on the mutual arrangement of the projectile and the surface wave. The surface wave leads to a dynamic redistribution of several properties, including the strength, plasticity, and adhesive ability at the material surface. The proposed mechanism of surface activation may play an important role in some other technological processes, for example, in the ultrasonic treatment of materials and surface coating by gasdynamic and detonation techniques.

Acknowledgments. This study was supported by the Presidential Program of Support for the Leading Scientific Schools in Russia (Scientific School of Academician V.E. Panin, project no. NSh-2324.2003.1) and by the joint project of the Ministry of Education of the

Russian Federation and the US Civilian Research and Development Foundation for the Independent States of the Former Soviet Union (BRHE Program, project no. 016-02).

REFERENCES

1. M. A. Chertov, A. Yu. Smolin, E. V. Shil'ko, *et al.*, Fiz. Mezomekh. **7** (2004).
2. K. I. Kozorezov, V. N. Maksimenko, and S. M. Usherenko, *Selected Problems of Modern Mechanics* (Izd. Mosk. Gos. Univ., Moscow, 1981), Part 1, p. 115.
3. O. P. Solonenko, A. P. Alkhimov, V. V. Marusin, *et al.*, *High-Energy Processes of Material Treatment* (Nauka, Novosibirsk, 2000).
4. S. P. Kiselev and V. P. Kiselev, Int. J. Impact Eng. **27**, 135 (2002).
5. A. E. Rakhimov, Vestn. Mosk. Univ., Ser. 1: Mat., Mekh., No. 5, 72 (1994).
6. *Physical Quantities. Handbook*, Ed. by I. S. Grigor'ev and E. Z. Melikhov (Énergoatomizdat, Moscow, 1991) [in Russian].
7. S. G. Psakhie, Y. Horie, G. Ostermeyer, *et al.*, Theor. Appl. Fract. Mech. **37**, 311 (2001).
8. S. G. Psakh'e, A. Yu. Smolin, E. V. Shil'ko, *et al.*, Zh. Tekh. Fiz. **67** (9), 34 (1997) [Tech. Phys. **42**, 1016 (1997)].
9. S. G. Psakh'e, A. Yu. Smolin, E. M. Tatarintsev, and E. A. Shvab, Pis'ma Zh. Tekh. Fiz. **26** (2), 13 (2000) [Tech. Phys. Lett. **26**, 51 (2000)].

Translated by P. Pozdeev

Technical Physics Letters, Vol. 30, No. 12, 2004, pp. 1013–1016. Translated from Pis'ma v Zhurnal Tekhnicheskoĭ Fiziki, Vol. 30, No. 23, 2004, pp. 85–94.

Determining Parameters of Ferroelectric Crystals by Method of Optimization

P. Yu. Guzenko, S. A. Kukushkin, A. V. Osipov, A. L. Fradkov, and V. V. Spirin

Institute for Problems in Mechanical Engineering, Russian Academy of Sciences, St. Petersburg, 199178 Russia

CICESE Research Center, P.O. Box 434934, San Diego, USA

Received July 14, 2004

Abstract—We propose a method based on the switching current variation for determining the physical parameters of ferroelectric crystals. Algorithms providing for the separate and joint determination of parameters such as the surface tension σ and the kinetic coefficient β_0 are presented. © *2004 MAIK "Nauka/Interperiodica".*

Introduction. Ferroelectric crystals and films are widely used in microelectronics and other technologies [1]. The most important property of ferroelectric materials is polarization reversal capacity [1–6], which gives rise to a switching current [3–7]. The phenomenon of switching in ferroelectrics has been extensively studied in recent years [3–12].

A kinetic theory of switching in ferroelectric crystals with 180° domains, based on the strict theory of first-order phase transitions, was developed in [13, 14]. According to this theory, the process of electric-field-induced domain switching is a first-order phase transition and can be described by a system of kinetic equations formally analogous to those for other phase transitions of the same kind. Formulas obtained as a result of the solution of this system of equations allow the switching current to be calculated as a function of the microscopic and macroscopic parameters and of the structure of the given ferroelectric crystal. In particular, it was established [13, 14] that the switching current is a single-valued function of parameters such as the surface tension and the kinetic coefficient, which characterizes the displacement of atoms from one to another sublattice of the crystal. The most important switching parameters are the switching current and duration [3–7]. These characteristics determine the possibility of using ferroelectric crystals in technical devices of various types. The experimentally measured switching current is usually described in terms of a selected semiempirical model involving a certain number of fitting parameters [6]. Based on such a description, it is possible to judge the mechanisms of switching that operate in various ferroelectric materials. However, this approach does not allow the aforementioned characteristics of a ferroelectric material to be determined because the semiempirical models do not reflect the true nature of the switching process.

One of the important questions still under discussion concerns the surface tension of domain walls in ferroelectric crystals [5], which is a parameter determining the switching kinetics. It is frequently concluded that the classical nucleation theory cannot be used for calculating the nucleation rate in ferroelectric media. Such conclusions are usually based on the fact that the nucleation rate calculated within the framework of the classical nucleation theory is lower than the experimental values. This discrepancy is explained by the use of overstated values of the surface tension and by ignoring the process of nucleation on the crystal defects. The surface tension can be determined using various methods [15], including the well-known technique based on the measurements of a liquid contact angle in air or in vacuum. However, the value of surface tension entering into an expression describing the domain wall nucleation rate [13, 14] differs from that determined by the surface wetting technique. This is related to the fact that, in the course of switching, domains with opposite orientations are in contact with each other and the polarization vector changes at the domain boundary. Therefore, the surface tension determining the switching process is more likely to be equal to the energy of the interface separating domains with opposite polarizations. For this reason, the required surface tension at the interface can be experimentally determined only by measuring the rate of nucleation of the repolarized domains.

The expression for the domain nucleation rate [13, 14] contains, besides the surface tension, several other ambiguously determined parameters, in particular the kinetic coefficient β_0, which depends on the activation energy of atomic displacements in the lattice of a ferroelectric crystal.

Since the expression for the switching current involves the dependence of the domain wall nucleation rate on the surface tension σ and the kinetic coefficient β_0, we suggest that it is possible to solve the inverse problem of determining the rate of nucleation of repolarized domains from the results of experimental measurements of the switching current in a given material exposed to a constant electric field. Once the nucleation

1063-7850/04/3012-1013$26.00 © 2004 MAIK "Nauka/Interperiodica"

rate is known, it is possible to determine the other important parameters of the given material.

In this context, we have studied the possibility of determining parameters such as the surface tension (interfacial energy) and the activation energy of atomic displacements in crystal cells from the results of experimental measurements of the switching current.

Switching current in a ferroelectric crystal. The time variation of the switching current in a ferroelectric capacitor is described by the formula [3]

$$j = -2P_{z10}\frac{d(1-Z)}{dt}, \quad (1)$$

where $d(1 - Z)/dt$ is the rate of variation of the volume fraction $Q = 1 - Z$ of a given ferroelectric material that is still not switched at a given moment of time, P_{z10} is the initial value of spontaneous polarization, and $Z = 1 - Q$ is the degree of filling of the crystal volume by the repolarized domains.

It was demonstrated [13, 14] that the value of Z (and, hence, of the switching current) can be determined by solving the system of equations

$$\left[\frac{1}{\xi}\left(\frac{Z'}{\xi}\right)'\right]' = \frac{2\omega}{t_0^2}I(\xi(t)). \quad (2)$$

Here, $I(\xi(t))$ is the domain nucleation rate [13], $\xi(t) = (\bar{P} - P_{z10})/P_{z10}$ is the degree of repolarization at the given time moment t, P_{z10} is the equilibrium polarization of the given crystal,

$$t_0 = \left(\frac{2\beta_0(\pi H\omega)^{1/2}\omega P_{z10}^2}{k_B T\chi\varepsilon_0}\right)^{-1}$$

is the characteristic growth time [13], χ is the dielectric susceptibility, ε_0 is the permittivity of vacuum, $\beta_0 = N_\nu\nu\exp(-V_0/k_BT)$, V_0 is the energy barrier for reversal of the polarization of the elementary dipole in the cell in the absence of an external field, ν is the frequency of atomic oscillations in the cell, $N_\nu = 1/\omega$ is the number of unit cells per unit crystal volume, ω is the unit cell volume, and the prime denotes differentiation with respect to time.

The above equation can be rewritten as

$$\left[\frac{1}{\xi}\left(\frac{j}{\xi}\right)'\right]' = -\frac{4\pi P_{z10}}{t_0^2}I(\xi). \quad (3)$$

The switching current is given by the formula [13, 14]

$$j = -\frac{2P_{z10}\left(\frac{\varepsilon_0}{\tau} - \frac{\varepsilon}{\tau} - \xi'\right)(1-Z)}{\left(\frac{P_{z2}}{P_{z10}} - 1 - \xi\right)}, \quad (4)$$

where ξ_0 is the initial value of repolarization. Substituting formula (4) into Eq. (3), we obtain

$$\left[\frac{1}{\xi}\left(\frac{\left(\frac{\xi_0}{\tau} - \frac{\xi}{\tau} - \xi'\right)(1-Z)}{\left(\frac{P_{z2}}{P_{z10}} - 1 - \xi\right)\xi}\right)'\right]' = \frac{2\omega}{t_0^2}I(\xi). \quad (5)$$

The initial conditions correspond to zero values of the switching current, its derivatives with respect time, and supersaturation.

The function $I(\xi)$, which was previously determined in the case of switching in ferroelectric crystals with 180° domains and the "normal" mechanism of domain growth [13, 14], can be written as

$$I(\xi) = I_0\xi^{1/2}e^{-\frac{a}{\xi}}, \quad (6)$$

where

$$I_0 = \frac{N_\nu\beta_0\omega P_{z10}\sqrt{H}}{\sqrt{k_BT\chi\varepsilon_0}}, \quad \alpha = \frac{\pi H\sigma^2\chi\varepsilon_0}{2k_BTP_{z10}^2}.$$

Solving the system of equations (3)–(6) and using the results obtained in [13, 14], it is possible to find all the main characteristics of the switching process. Comparing the theoretical and experimental dependences of the switching current, one can determine the constants I_0, t_0, and α entering into the expression for the flux of nuclei $I(\xi)$. From these data, it is possible to determine some parameters of ferroelectric crystals (including the surface tension σ, the kinetic coefficients β_0, etc.). Moreover, the obtained equations allow the flux and number of the switching domains formed in the course of repolarization to be determined as well. This number of domains can be compared to that determined by alternative methods, for example, via direct microscopic examination [3, 4, 8].

Thus, investigation of the polarization currents in ferroelectric materials opens unique possibilities for determining parameters of these media that are difficult to measure by direct methods.

Determining nonmeasurable parameters. In order to formulate the determination algorithm, let us write Eqs. (3)–(6) in the form of a system of ordinary differential equations with the state vector $y(t) = [y_0y_1y_2y_3]^T$:

$$\frac{d}{dt}y(t) = \begin{cases} \xi(0) - y_2y_0\dfrac{P - 1 - y_0}{1 - y_1} + 10^8y_0, \\ y_0y_2, \\ y_0y_3, \\ I_0\sqrt{y_0}\exp\dfrac{-\alpha}{y_0}, \end{cases} \quad (7)$$

where $P = P_{z2}/P_{z10}$, $\xi(0) = \xi_0/\tau$, $y_0 = \xi$, $y_1 = Z$, and $y_2 = \xi'$.

Determining parameter α. Let us denote the unknown value of α by α_* and the corresponding switching current by $j_*(t)$; the values of all other parameters (I_0, ξ_0, etc.) are assumed to be known. Consider the following function J of the argument α:

$$J(\alpha) = \int_0^\infty [j(t) - j_*(t)]^2 dt, \quad (8)$$

where $j(\alpha)$ is the switching current corresponding to α. Evidently, if the initial values in the calculation of $j(t)$ and $j^*(t)$ coincide, the function $J(\alpha)$ reaches its absolute minimum at $\alpha = \alpha_*$: $J(\alpha_*) = 0$. Then, the problem of determining α reduces to the minimization problem,

$$\hat{\alpha} = \arg \min_{\alpha \in [\alpha^-, \alpha^+]} J(\alpha), \quad (9)$$

where the initial segment $[\alpha^-, \alpha^+]$ is selected earlier according to physical considerations.

According to [13], we have

$$\alpha = \frac{\pi H \sigma^2 \chi \varepsilon_0}{2 k_B T P_{z10}^2}.$$

In particular, for TGS crystals at $T = 300$ K, the value of this parameter can vary from 8×10^{-2} to 5×10^{-1} [13].

The minimization problem (9) was solved using the golden section technique [16–19], which is optimum with respect to the criterion of minimization of the number of calculations of the target function. The algorithm was simulated using system (8) with the following parameters: $\alpha = 0.25$; $I_0 = 10^{30}$; $P = 1.2$; $\xi_0 = 1.5 \times 10^6$; $y(t = 0) = [10^{-10}\,0\,0\,0]^T$; integration interval, from 0 to 2×10^{-5}; initial segment, $[\alpha^-, \alpha^+] = [0.15, 0.35]$.

System (7) was integrated using the Euler method with a constant step, which is convenient for overcoming singularities on the right-hand side of these equations. Figure 1 shows the typical process of convergence of the determination algorithm. As can be seen, an accuracy of 10^{-5} is achieved within 35 steps of the minimization algorithm.

Determining parameter I_0. For the same system, let us denote the unknown value of I_0 by I_* and the corresponding switching current by $j_*(t)$; the values of all other parameters (α_0, ξ_0, etc.) are assumed to be known. The minimizing function J of the argument I is defined as

$$J(I) = \int_0^\infty [i(t) - j_*(t)]^2 dt, \quad (10)$$

where $j(t)$ is the switching current corresponding to I. Then, the problem of determining I reduces to the minimization problem

$$\hat{I} = \arg \min_{I \in [I^-, I^+]} J(I), \quad (11)$$

where the initial segment $[I^-, I^+]$ is selected according to physical considerations. The value of I_0 can vary from 1×10^{29} to 1×10^{31}.

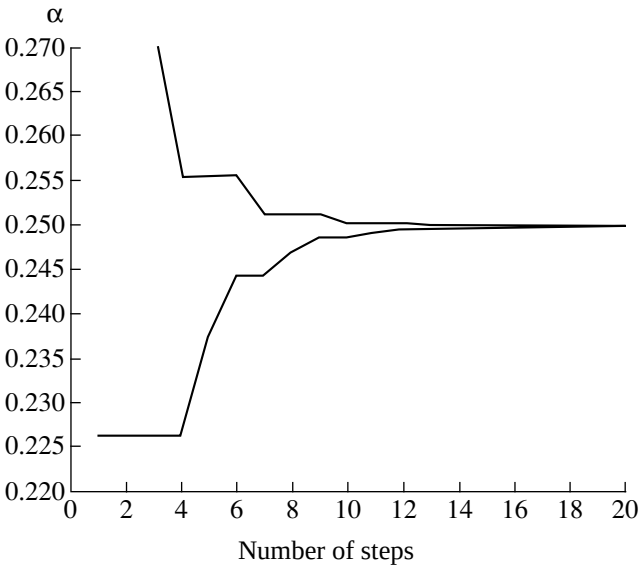

Fig. 1. Convergence of the proposed algorithm: upper and lower boundaries for $\alpha_* = 0.25$.

This minimization problem is also solved using the golden section technique. The solution was modeled for the initial segment, $[I^-, I^+] = [10^{29}, 10^{31}]$ and $I_0 = 10^{30}$. The convergence of the proposed determination algorithm is analogous to that in the preceding case. An accuracy of 10^{-4} is achieved within 40 steps of the minimization algorithm.

Joint determination of parameters α and I_0. For the same system, let us denote the unknown values of α and I_0 by α_* and I_*, respectively, and the value of current corresponding to the pair (α_*, I_*) by $j_*(t)$; the values of all other parameters (ξ_0, etc.) are assumed to be known. The minimizing function J of two arguments, α and I, is defined as

$$J(\alpha, I) = \int_0^\infty [j(t) - j_*(t)]^2 dt, \quad (12)$$

where $j(t)$ is the switching current corresponding to pair (α, I). Then, the problem of determining of I reduces to the minimization problem

$$(\hat{\alpha}, \hat{I}) = \arg \min_{(\alpha, I) \in [\alpha^-, \alpha^+] \times [I^-, I^+]} J(\alpha, I). \quad (13)$$

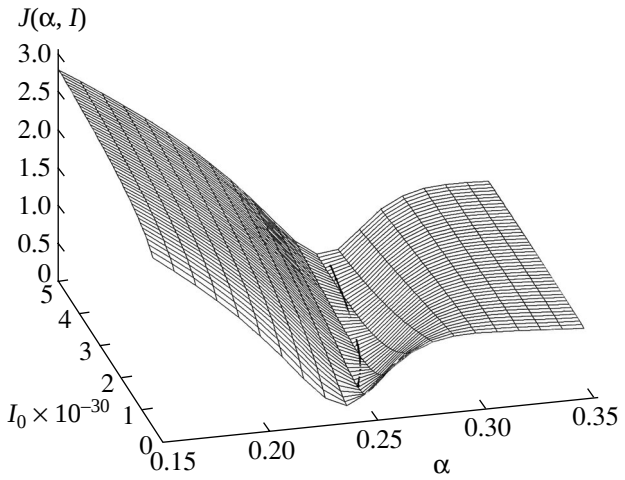

Fig. 2. Plot of the function $J(\alpha, I)$ and convergence of the determination algorithm to the minimum point of the target function for $\alpha_* = 0.25$, $I_0 = 10^{30}$.

The values of α and I_0 can vary in the intervals selected above, and the initial point (α_*, I_*) is chosen in a rectangle indicated in (13).

Investigation of the function $J(\alpha, I)$ shows that this surface is nonconvex and has a valley (Fig. 2). For minimizing this function, we developed a numerical coordinate-valley algorithm based on the coordinate descent method and on the Gelfand–Tseitlin valley technique [17]. The combined algorithm comprises alternating steps of coordinate descent and "valley" steps performed in the direction between two sequential points, resulting in the descent toward a point with a lower value of the target function. The "valley" step magnitude h is selected based on the results of numerical simulations. The best results for the initial value of $I_0 = 5 \times 10^{-30}$ were obtained for $h = -0.4 \times 10^{-30}$.

Figure 2 shows the function $J(\alpha, I)$ and a typical trajectory on this surface. It was established that determination with an error not exceeding 10^{-5} for α and 10^{-3} for I_0 is achieved after about 25 steps of the proposed algorithm.

Once the estimates of α and I_0 are obtained, it is possible to find the surface tension (interfacial energy) σ, the kinetic coefficient β_0, and the corresponding energy barrier V_0 using formulas (6).

In conclusion, it should be noted that, using a similar procedure, these parameters can be determined not only for ferroelectric crystals with 180° domains, but for multiaxial ferroelectrics as well [1, 2].

Acknowledgments. This study was supported in part by the Russian Foundation for Basic Research (project nos. 02-01-00765, 03-01-00574, 03-03-32503), the Federal Special Program "Integration" (project no. B0026), the Basic Research Program No. 19 of the Presidium of the Russian Academy of Sciences (project no. 1.4, "Control of Mechanical Systems"), CONACYT Project No. 32208 (Mexico), and the Foundation for Support of Russian Science.

REFERENCES

1. B. A. Strukov and A. P. Livanyuk, *Physical Principles of Ferroelectric Phenomena in Crystals* (Nauka, Moscow, 1995) [in Russian].
2. F. Jona and G. Shirane, *Ferroelectric Crystals* (Pergamon Press, Oxford, 1962).
3. R. S. Cudney, J. Fousek, M. Zgonik, *et al.*, Phys. Rev. Lett. **72**, 3883 (1994).
4. V. Ya. Shur, E. L. Rumyantsev, and S. D. Makarov, J. Appl. Phys. **84**, 445 (1998).
5. A. K. Tagantsev, I. Stolichnov, E. L. Colla, and N. Setter, J. Appl. Phys. **90**, 1387 (2001).
6. V. Ya. Shur, U. V. Nikolaeva, E. I. Shishkin, *et al.*, Fiz. Tverd. Tela (St. Petersburg) **44**, 2055 (2002) [Phys. Solid State **44**, 2151 (2002)].
7. L. I. Dontzova, N. A. Tikhomirova, and L. A. Shuvalov, Ferroelectrics **97**, 87 (1989).
8. Y. Ishibashi and Y. Takagi, J. Phys. Soc. Jpn. **31**, 506 (1971).
9. H. M. Duiker, P. D. Beale, J. F. Scott, *et al.*, J. Appl. Phys. **68**, 5783 (1990).
10. A. M. Bratkovsky and A. P. Levanyuk, Phys. Rev. Lett. **84**, 3177 (2000).
11. M. Molotskii, R. Kris, and G. Rosenmann, J. Appl. Phys. **88**, 5318 (2000).
12. A. M. Bratkovsky and A. P. Levanyuk, Phys. Rev. Lett. **85**, 4614 (2000).
13. S. A. Kukushkin and A. V. Osipov, Fiz. Tverd. Tela (St. Petersburg) **43**, 80 (2001) [Phys. Solid State **43**, 82 (2001)]; **43**, 88 (2001) [**43**, 90 (2001)]; **43**, 312 (2001) [**43**, 325 (2001)].
14. S. A. Kukushkin and A. V. Osipov, Phys. Rev. B **65**, 174101 (2002).
15. A. I. Rusanov and V. A. Prokhorov, *Interface Strain Gauging* (Khimiya, St. Petersburg, 1994) [in Russian].
16. B. T. Polyak, *Introduction to Optimization* (Nauka, Moscow, 1983) [in Russian].
17. B. G. Karmanov, *Mathematical Programming* (Nauka, Moscow, 1975) [in Russian].
18. S. A. Kukushkin, A. V. Osipov, P. Yu. Guzenko, and V. V. Spirin, in *Proceedings of the International Conference "Physics and Control," St. Petersburg, 2003*, Vol. 3, pp. 937–941.
19. M. A. Zakharov, S. A. Kukushkin, and A. V. Osipov, Fiz. Tverd. Tela (St. Petersburg) **46**, 1238 (2004) [Phys. Solid State **46**, 1277 (2004)].

Translated by P. Pozdeev

Technical Physics Letters, Vol. 30, No. 12, 2004, pp. 1017–1019. Translated from Pis'ma v Zhurnal Tekhnicheskoĭ Fiziki, Vol. 30, No. 24, 2004, pp. 1–6.

Shock Wave Reflection and Diffraction on a Convex Double Wedge

M. K. Berezkina, I. V. Krasovskaya*, and D. Kh. Ofengeim

Ioffe Physicotechnical Institute, Russian Academy of Sciences, St. Petersburg, 194021 Russia

** e-mail: i.kras@pop.ioffe.rssi.ru*

Received July 9, 2004

Abstract—We have numerically simulated the interaction of a shock wave with a convex double angle within the framework of a model of inviscid non-heat-conducting gas. The main attention is paid to the stage of a two-shock diffraction configuration on the second face of the wedge. Special features of flow under various conditions of diffraction are revealed. We also propose an explanation of the appearance and behavior of a purely gasdynamic layer formally resembling the viscous boundary layer. *© 2004 MAIK "Nauka/Interperiodica".*

For a shock wave incident on a solid surface, we can distinguish three regimes of interaction depending on the angle α between the shock wave front and the immobile surface. In the case of $\alpha = 90°$, the shock wave travels along the surface; for $\alpha < 90°$, the shock wave is reflected from the surface; and for $\alpha > 90°$, the shock wave is diffracted or rounds the surface. It should be noted that the process of diffraction takes place only in nonstationary flows.

The phenomenon of shock wave reflection has been rather thoroughly studied and the exhaustive results of both theoretical and experimental investigations are available (see, e.g., monographs [1, 2]). The diffraction of a single shock wave was considered in [1, 3–5].

This paper reports on the results of numerical simulation of the interaction of a shock wave with a convex double wedge. The shock wave exhibits regular reflection on the first face, after which the resulting two-shock configuration exhibits diffraction on the second face of the wedge. The main attention is paid to the latter diffraction stage, since published data concerning this phenomenon [6–9] are by no means sufficient.

The shock wave interaction with the double wedge was described within the framework of a model of the inviscid non-heat-conducting gas with γ = const. The corresponding system of Euler equations was numerically integrated by a method proposed by Fursenko *et al.* [10], using a computational code kindly provided by Voinovich [11]. The results will be presented for three variants with different conditions of wave interaction on the second face. In all variants, the incident shock wave had a Mach number of $M = 2.09$ and the incidence angle was $\alpha_1 = 42°$ for $\gamma = 1.29$; the variants differed in α_2, which was 90° (variant 1), 114° (variant 2), and 180° (variant 3).

Figures 1a–1c show the temperature field isolines at the time $t = 1.5$ for variants 1–3, respectively, and Figs. 1d–1f present the fragments of these patterns on a greater scale. The time is measured from the moment when the incident shock wave passes the vertex of the double wedge ($x = 0$). At this moment ($t = 0$), the components of the two-shock configuration simultaneously diffract so as to form a new, three-shock configuration. An analysis of this pattern using the Landau concept of the "directed" shock wave showed that the latter configuration should be assigned the "confluence" type, since it comprises two *incoming* waves (*I*, *R*) and one *outgoing* wave (*M*), rather than the "reflection" type [7]. The geometric characteristics of the three-shock configuration in the vicinity of the triple point *T* for all three variants are the same, whereas the shape of the diffracted wave *M* changes from one variant to another. In addition to the triple point *T*, which is considered the first diffraction point, the front of wave *R* contains the second diffraction point *D* separating the diffracted and unperturbed regions of the reflected shock wave. Point *D* is the origin of a relatively weak tangential discontinuity, which is defined by inflections of the isotherms and is schematically depicted by a dashed line in Figs. 1a–1c.

The flow structure inside the perturbed region at $t > 0$ is determined by two processes: (i) gas compression in the shock waves forming the outer boundary of the perturbed region and (ii) gas expansion in the rarefaction wave emanating the wedge vertex. Expanded in the rarefaction fan, the flow either moves along the second face of the wedge (Fig. 1a) or is separated from this face by a region of the gas entrained by wave *M* (Fig. 1c). The results of calculations show that the boundary of the gas passing via the Prandtl–Mayer fan possesses a clear layer structure (Figs 1d–1f). The appearance of this layer can be explained as follows: although the flow parameters in the rarefaction wave continuously vary, the passage through the Prandtl–Mayer fan center (which a singular point) can be considered analogous to crossing the "rarefaction shock wave." As a result of the gas passage in the vicinity of

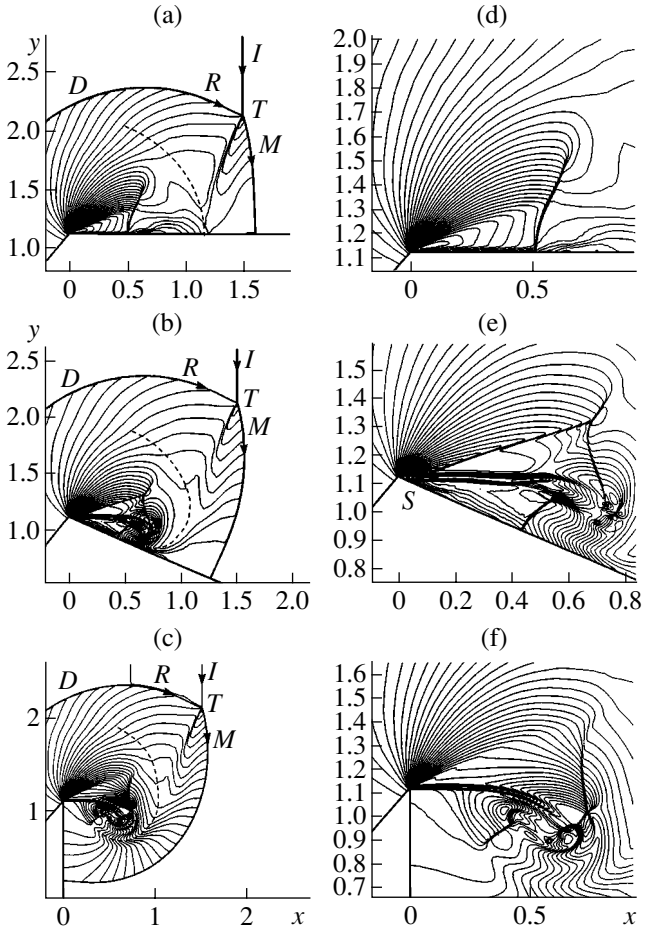

Fig. 1. The temperature field isolines near the surface of a double wedge under various conditions of shock wave diffraction corresponding to (a, d) variant 1, (b, e) variant 2, and (c, f) variant 3 (see the text for explanations).

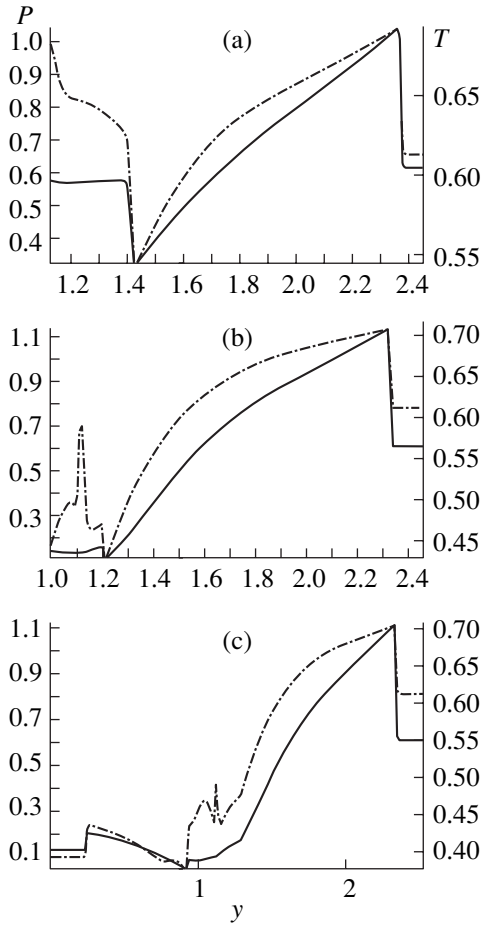

Fig. 2. The profiles of temperature T (dash–dot lines) and pressure P (solid lines) in a perturbed flow field in (a) variant 1 ($x = 0.6$), (b) variant 2 ($x = 0.34$), and (c) variant 3 ($x = 0.3$).

this fan, a special region having the shape of a layer appears at the output and is clearly manifested in the temperature field isolines (Fig. 1). This layer may be conditionally called the *TU* layer, in contrast to the boundary layer formed in a viscous gas.

Variant 1 is characterized by the minimum curvature of the diffracted shock wave. The gas flow in the vicinity of the horizontal surface of the wedge is close to one-dimensional. After acceleration in the rarefaction wave, the flow is retarded in a single curvilinear shock wave propagating downstream, which is perpendicular to the wedge near its surface, so that the *TU* layer spreads out along the wedge surface. Figures 2a–2c show the distributions of pressure P and temperature T in the cross sections at $x = 0.6$, 0.34, and 0.3 for variants 1–3, respectively. In variant 1, the section crosses the *TU* layer, the curvilinear part of the retarding shock, the nonuniform rarefaction region, and the reflected shock wave.

In variant 2, the curvature of the diffracted shock wave is greater than in variant 1. Here, the shock-wave-compressed flow rolls up and drives the *TU* layer away from the surface (Fig. 1e) at point *S*, where an oblique shock is settled. The free end of the deviating layer is also twisted to form a circular flow region with a center (determined from the velocity vector field) indicated by a circle in Fig. 1e. Instead of a single retarding shock as in variant 1, variant 2 features shock-wave structures situated both above and below the *TU* layer. A three-shock configuration appears above the layer, with an additional triple point nucleated on one (rightmost) of these shock waves. A retarding shock appears below the layer, with one end being perpendicular to the wedge surface and the other featuring another three-shock wave configuration (Fig. 1e). These peculiarities in the flow structure are confirmed by the corresponding features of the $T(y)$ and $P(y)$ profiles at $x = 0.34$ (Fig. 2b).

In variant 3, the flow behind the diffracted shock wave becomes even more nonuniform: the intensity of the front of wave *M* decreases, while the flow twist in the central region increases. The layer separates from the wedge surface immediately at the vertex (Figs. 1c and 1f). The free end of this layer twists into a well-pronounced vortex centered at the point (0.57, 0.91), the

sublayer shock is "suspended" in the flow, and the three-shock wave configuration degenerates into a single shock wave. Interacting with the layer, the latter shock wave forms a new irregular five-shock configuration with two triple points (Fig. 1f). It can be seen from the pressure and temperature profiles in the section at $x = 0.3$ (Fig. 2c) that, because of circulative motion, the sublayer shock retards the counterflow and turns so as to face the front of the diffracted wave *M*.

In conclusion, the results of the numerical simulation of the diffraction pattern in the system under consideration allowed us to consider the formation and behavior of a new gasdynamic phenomenon called *TU* layer. This layer, despite apparent similarity to the viscous boundary layer, is determined entirely by gasdynamic phenomena. More detailed data on this nonstationary process will be reported in subsequent publications.

REFERENCES

1. T. V. Bazhenova and L. G. Gvozdeva, *Nonstationary Interactions of Shock Waves* (Nauka, Moscow, 1977) [in Russian].
2. G. Ben-Dor, *Shock Wave Reflection Phenomena* (Springer-Verlag, New York, 1991).
3. B. W. Skews, J. Fluid Mech. **29**, 705 (1967).
4. R. Hillier, in *Proceedings of the 19th International Symposium on Shock Waves, Marseille, 1995*, Ed. by R. Brun and L. Z. Dumitrescu (Springer-Verlag, Berlin, 1995), pp. 17–26.
5. H. Kleine, E. Ritzerfeld, and H. Crönig, in *Proceedings of the 19th International Symposium on Shock Waves, Marseille, 1995*, Ed. by R. Brun and L. Z. Dumitrescu (Springer-Verlag, Berlin, 1995), pp. 117–122.
6. H. Shardin, J. Photogr. Sci. **5**, 19 (1957).
7. B. W. Skews, in *Proceedings of the 9th International Symposium on Shock Tubes, Stanford, 1973*, pp. 546–553.
8. D. L. Zhang and I. I. Glass, Int. J. Eng. Fluid Mech. **3**, 383 (1990).
9. S. M. Chang and K. S. Chang, Shock Waves **10**, 333 (2000).
10. A. Fursenko, D. Sharov, and E. Timofeev, in *Proceedings of the 19th International Symposium on Shock Waves, Marseille, 1995*, Ed. by R. Brun and L. Z. Dumitrescu (Springer-Verlag, Berlin, 1995), Vol. 1, pp. 371–376.
11. P. Voinovich, *Two-Dimensional Locally Adaptive Unstructured Unsteady Euler Code* (Advanced Technology Center, St. Petersburg, 1993).

Translated by P. Pozdeev

Technical Physics Letters, Vol. 30, No. 12, 2004, pp. 1020–1022. Translated from Pis'ma v Zhurnal Tekhnicheskoĭ Fiziki, Vol. 30, No. 24, 2004, pp. 7–11.

Influence of the Insulator Thickness Inhomogeneity on the Current–Voltage Characteristics of Tunneling MOS Structures

S. E. Tyaginov, M. I. Vexler, A. F. Shulekin*, and I. V. Grekhov

Ioffe Physicotechnical Institute, Russian Academy of Sciences, St. Petersburg, 194021 Russia

** e-mail: shulekin@pop.ioffe.rssi.ru*

Received June 29, 2004

Abstract—The current–voltage (*I–V*) characteristics of $Al/SiO_2/Si$ metal–oxide–semiconductor (MOS) tunnel structures have been modeled with allowance for the lateral inhomogeneity of the oxide layer thickness. It is established that considerable dispersion of the insulator thickness modifies the *I–V* curve shape. Values of the current dispersion are determined in a broad range of linear dimensions of the MOS device. The modeling has been performed using the most recent data on the parameters of tunneling, which provides for quantitative accuracy of the results. © *2004 MAIK "Nauka/Interperiodica".*

For thin metal–oxide–semiconductor (MOS) structures, important characteristics of the oxide layer include, in addition to the nominal thickness d_n, the rms (standard) deviation σ_d (or dispersion) of this parameter. It is naturally expected that σ_d must be on the order of SiO_2 monolayer thickness (0.31 nm), and the best commercial MOS structures are characterized by $\sigma_d \sim$ 0.15 nm [1]. It is also clear that the local thickness of the oxide layer cannot exhibit arbitrarily sharp variations in lateral directions. In other words, significant variations in the *d* value may take place over a certain distance λ, which is referred to below as the characteristic inhomogeneity scale. This scale may prove to be both smaller and greater than the linear size *L* of a sample. The general trends of miniaturization [2] lead to situations when the condition $L \gg \lambda$ is not evident a priori.

The aim of this study was to evaluate the effect of dispersion of the oxide layer thickness on the current–voltage (*I–V*) characteristics of Al/SiO_2(2.5–4.0 nm)/*n*-Si tunnel structures in a broad range of variation of the L/λ ratio.

The MOS device current has been calculated assuming that the thickness of the SiO_2 layer obeys a normal distribution (truncated at $d < 0$) with the parameters $\langle d \rangle = d_n$ and σ_d. For the sake of simplicity, we considered *d* as constant within a certain region with dimensions determined by the characteristic length λ. The calculations were performed on a square grid with the step λ, which was randomly displaced relative to the device boundaries. Each $\lambda \times \lambda$ cell centered at a given lattice node was assigned the corresponding value of *d*. Then, the local current densities in the cells were calculated [3–5] and the average current density *I*/*S* in the device was determined.[1]

Using the above model, we obtained the *I–V* curves corresponding to the oxide thickness profiles constructed by generating random sets of *d* values. In the general case, the *I*/*S* value for a given applied voltage varies from one device to another. This scatter is characterized by the standard deviation $\sigma_{I/S}$ of the *I*/*S* ratio from its mean value $\langle I/S \rangle$.

In the limit of $L \gg \lambda$, the local current densities exhibit natural averaging. The *I–V* curves of MOS structures fabricated in a single technological cycle must not exhibit scatter, although each device is characterized by its own profile of the SiO_2 layer thickness. Therefore, the dispersion of current is negligibly small and the current is equal to the mean value, which exceeds the current in the structure with the same d_n and $\sigma_d = 0$. Devices with inhomogeneous insulator thickness profiles for $L \gg \lambda$ are sometimes characterized by the effective thickness $d_{eff} \approx d_n - 0.5\sigma_d^2$ (all values expressed in ångströms). This estimate is obtained by roughly approximating the local current density as $j \sim \exp(-\alpha d)$ (where $\alpha = 2\hbar^{-1}(2m_{ox}\Phi)^{1/2}$), averaging this *j* over the normal oxide thickness distribution, and taking $\Phi \sim 2.5$ eV for the characteristic average tunneling barrier height. Using this approach, it is possible to roughly predict the current in a MOS tunnel structure with $\sigma_d \neq 0$.

[1] Calculations were performed for tunneling in the *z* axis direction with the following parameters: $m^e_{z,\,Si} = 0.432$, $m^e_{\perp,\,Si} = 2.044$, $m_{ox} = 0.4$ [6] (all in m_0 units); conduction band discontinuity at the Si/SiO_2 interface, $\chi_e = 3.15$ eV; Al/SiO_2 barrier, $\chi_m = 3.17$ eV.

1063-7850/04/3012-1020$26.00 © 2004 MAIK "Nauka/Interperiodica"

Figure 1 shows the families of calculated *I–V* curves corresponding to three values of the effective oxide layer thickness. For a fixed dispersion σ_d, the d_n values were selected so as to provide that the corresponding d_{eff} (and, roughly, the corresponding currents) were the same for each family of the *I–V* curves. As can be seen, the current–voltage characteristics of MOS structures with large σ_d values significantly deviate from the *I–V* curve of the device with zero dispersion of the oxide thickness. It is large σ_d values (and, hence, large differences between d_{eff} and d_n) that may account for the fact that the mutual arrangement of experimental and theoretical *I–V* curves in many cases (see, e.g., [7]) is such that the experimental currents exceed theoretical ones in the region of relatively small voltages, whereas theoretical values are greater than experimental ones in the region of high voltages.

Figure 1 also presents two experimental curves. The measurements were performed for MOS structures of two types: (i) with a relatively thick oxide layer having a nominal thickness $d_n \approx 3.8$ nm and dispersion $\sigma_d \approx 0.5$ nm (by transmission electron microscopy data), so that $d_{eff} \approx 2.5$ nm; (ii) with a relatively thin insulator such that $d_n \approx 2.7$ nm, $\sigma_d \approx 0.3$ nm, and $d_{eff} \approx 2.3$ nm. Thin oxide was grown in a dry O_2(20%)–N_2 mixture at 700°C. The MOS device area was $S = 1.26 \times 10^{-3}$ cm^2. As can be seen, the experimental curve for the sample with a greater dispersion exhibits a significantly smoother behavior.

Let us proceed to the other limiting case of $L \ll \lambda$. For this relation between the spatial scales, the *I–V* curves strongly vary from one device to another. Note that the $\langle I/S \rangle$ value is the same as that for $L \gg \lambda$, since it is independent of the stage at which the averaging is performed: either in the step of summing currents passing through the areas with local oxide thicknesses *d* or in the step of statistical analysis of a sample batch of devices with randomly distributed SiO_2 thickness profiles. Thus, $\langle I/S \rangle$ is constant in the entire range of L/λ ratios.

In contrast, the dispersion $\sigma_{I/S}$ is strongly dependent on L/λ. Indeed, it was indicated above that $\sigma_{I/S}$ is zero for $L \gg \lambda$. On the contrary, for $L \ll \lambda$, this dispersion acquires a certain nonzero value that can be numerically evaluated. When the characteristic inhomogeneity scale is greater than the size of a device, we may assume that the entire device has the same oxide thickness *d*. In the batch of devices, this thickness is distributed according to the normal law, and the current density *I*/*S* (for a preset value of the applied voltage) is a function of *d*. Using the apparatus of probability theory, it is possible to calculate the probability density for *I*/*S* and the corresponding dispersion.

Figure 2 shows the plots of $\sigma_{I/S}$ versus L/λ for the entire range of this ratio in the accumulation regime. As can be seen, the dispersion of the current density tends to zero for large values of the L/λ ratio. In the region of

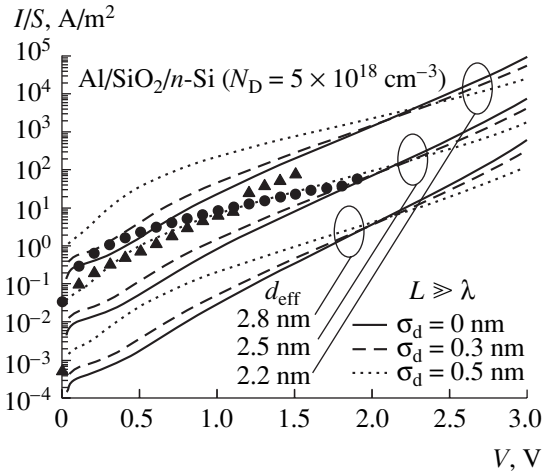

Fig. 1. The current-voltage characteristics of MOS tunnel structures of large area with inhomogeneous oxide thickness. Curves show the results of calculations for various dispersions σ_d; symbols present the experimental results for $d_n \approx 3.8$ nm, $\sigma_d \approx 0.5$ nm (circles) and $d_n \approx 2.7$ nm, $\sigma_d \approx 0.3$ nm (triangles).

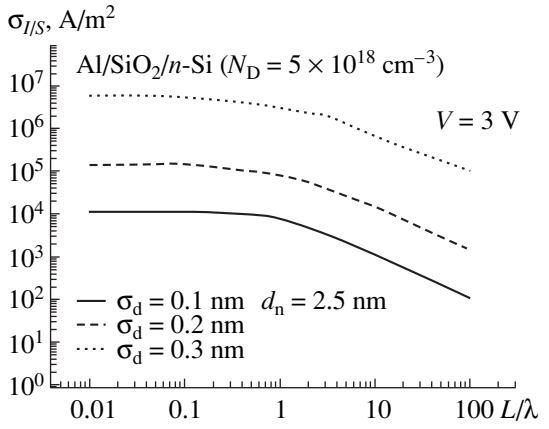

Fig. 2. Plots of the average current density dispersion $\sigma_{I/S}$ versus ratio L/λ of the device size to the characteristic scale λ of the oxide thickness inhomogeneity for various dispersions σ_d.

$L/\lambda \sim 1$, the behavior of $\sigma_{I/S}$ changes and exhibits a transition to another stationary value corresponding to the limit of small L/λ. The latter stationary value depends on σ_d. Indeed, the values of $\sigma_{I/S}$ (in the limit $L/\lambda \ll 1$) calculated for $\sigma_d = 0.2$ and 0.3 nm differ by almost two orders of magnitude and exceed the current density in a device with $d_n = 2.5$ nm and $\sigma_d = 0$ by a factor of 20 and ~1000, respectively.

In addition, the data in Fig. 2 show that the width of the transition region increases with increasing dispersion of the oxide layer thickness. For example, in the case of $\sigma_d = 0.2$ nm, a sharp decay in the current dispersion begins at $L/\lambda \sim 0.2$, while for $\sigma_d = 0.1$ nm this decay begins at $L/\lambda \sim 1$.

We have no experimental data of our own for the situation with $L \ll \lambda$, but a considerable scatter of current in such a case, with the resulting fluctuations in the threshold voltage of field-effect transistors, was reported in [8].

The picture described above on a qualitative level might seem rather obvious even without calculations, probably, except for the of *I–V* curve transformation revealed at large oxide thickness dispersions σ_d. However, we believe that the results are important from the quantitative standpoint. The opportunity for quantitative calculation appeared only quite recently, when the numerical values of parameters for the correct modeling of tunneling currents through SiO_2 were reliably determined.

Acknowledgments. The authors gratefully acknowledge the support from the program "Physics and Technology of Low-Dimensional Structures," the Presidential Program of Support for Leading Scientific Schools in Russia (project no. NSh-758.2003.2), the Russian Science Support Foundation, and the Soros Foundation.

REFERENCES

1. H. S. Momose, S. Nakamura, T. Ohguro, *et al.*, IEEE Trans. Electron Devices **45**, 691 (1998).
2. *SEMATECH: The International Technology Roadmap for Semiconductors*; http://public.itrs.net.home.htm (2001).
3. W. A. Harrison, Phys. Rev. **123**, 85 (1961).
4. M. I. Vexler, Solid-State Electron. **47**, 1283 (2003).
5. N. Asli, PhD Thesis (Kiel Univ., Germany, 2004).
6. N. Houssa, S. de Gendt, P. de Bokx, *et al.*, Microelectron. Eng. **48**, 43 (1999).
7. Khairurrijal, M. Mizubayashi, and M. Hirose, J. Appl. Phys. **87**, 3000 (2000).
8. M. Koh, K. Iwamoto, W. Mizubayashi, *et al.*, Tech. Dig. Int. Electron Devices Meet. 919 (1998).

Translated by P. Pozdeev

Technical Physics Letters, Vol. 30, No. 12, 2004, pp. 1023–1026. Translated from Pis'ma v Zhurnal Tekhnicheskoĭ Fiziki, Vol. 30, No. 24, 2004, pp. 12–19.

Analytical Solution of the Problem of Concentration Jump during Evaporation of a Binary Mixture

A. V. Latyshev and A. A. Yushkanov*

Moscow State Regional University, Moscow oblast, Russia

** e-mail: yushkanov@mtu-net.ru*

Received June 18, 2004

Abstract—An analytical solution of the problem of concentration jump during evaporation of a binary mixture from a flat surface is obtained and analyzed. © *2004 MAIK "Nauka/Interperiodica".*

In recent years, there has been growing interest in solving problems related to the influence of the evaporation coefficient on the process of thermal diffusion in air-dispersed systems [1, 2]. It should be noted that this phenomenon involving a concentration jump at the gas–condensed phase interface has been also considered in a somewhat different aspect [3, 4]. Previously, the concentration jump for a binary gas mixture was calculated by approximate methods [5, 6], while analytical solution of the corresponding mathematical problem was not obtained. An analytical solution was only reported for a single-component gas [7], but this solution does not provide adequate description in some practical applications.

Different variants of boundary conditions have been used for the analysis of evaporation into a binary gas mixture [1–4]. These variants employ different dependences on the evaporation coefficient. In order to clarify this situation, it is necessary to develop an exact quantitative theory for the kinetic coefficients, which would provide a correct description of the dependence of these values on the evaporation coefficient.

In this study, we consider the process of evaporation from a flat surface into a binary gas mixture, assuming that the concentration n_1 of the evaporating component is much smaller than that (n_2) of component retained on the surface: $n_1 \ll n_2$. This condition is valid in most important practical applications.

The Boltzmann equation for a binary gas mixture can be written as [8]

$$\frac{\partial f_i}{\partial t} + \mathbf{v}_i \frac{\partial f_i}{\partial \mathbf{r}_i} = J_{ii} + J_{ij}, \quad i \neq j, \quad i, j = 1, 2, \qquad (1)$$

where $\mathbf{r}_i$ and $\mathbf{v}_i$ are the radius vector and velocity of molecules of the ith component of the gas mixture, respectively; f_i is the corresponding distribution function; and J_{ii} and J_{ij} are the integrals of collisions of molecules of the ith component with like molecules and with those of the jth component:

$$J_{ij} = \int v_{ij}(f_i' f_j' - f_i f_j) d\sigma_{ij} d^3 p_j. \qquad (2)$$

In these expressions, f_i' is the distribution function of the ith component after collision, p_j is the momentum of the jth component, $d\sigma_{ij}$ is the differential scattering cross section for molecules of the ith and jth components, and $v_{ij} = |\mathbf{v}_i - \mathbf{v}_j|$. It should be noted that $J_{11} \sim n_1^2$ and $J_{12} \sim n_1 n_2$ because $f_i \sim n_i$.

A small parameter in the system under consideration is $\varepsilon = n_1/n_2 \ll 1$, and it is obvious that $|J_{11}|/|J_{12}| \sim \varepsilon$. For this reason, to the first approximation with respect to ε, we may ignore J_{11} in comparison to J_{12}. In this approximation, we may also neglect the influence of the second component on the distribution function of the first component. Therefore, in the problem under consideration, the distribution function of the first component can be described by the equilibrium Maxwell function with an average velocity $\mathbf{U}_1 = 0$ and the given temperature T and concentration n_1.

The value of J_{12} can be approximated in terms of a kinetic model of the Bhatnagar–Gross–Krook type [9]. Then, taking into account Eqs. (1) and (2), the kinetic equation for the first component takes the form

$$\frac{\partial f_1}{\partial t} + \mathbf{v}_1 \frac{\partial f_1}{\partial \mathbf{r}_1} = \nu_1 (f_1^0 - f_1), \qquad (3)$$

where

$$f_1^0 = n_1 \left(\frac{\beta_1}{\pi}\right)^{3/2} \exp(-\beta_1 v_1^2), \quad \beta_1 = \frac{m_1}{2kT}$$

is the equilibrium Maxwell function of the first component, k is the Boltzmann constant, ν_1 is the effective collision frequency for molecules of the first component, and n_1 is the local concentration of these molecules:

$$n_1 = \int f_1 d^3 v_1.$$

1063-7850/04/3012-1023$26.00

It can be shown that the effective collision frequency ν_1 is related to the diffusion coefficient as

$$D_{12} = \frac{kT}{\nu_1 m_1}.$$

Consider a Cartesian coordinate system with the origin on the surface from which evaporation take place, and let x_1 axis be perpendicular to this surface. In the course of evaporation, a constant gradient of concentration of the first component is established far from the surface: $g_n^1 = (dn_1/dx_1)_\infty$. Let us assume that the evaporation is slow, so that a relative change in concentration of the first component over the mean free path length l is much smaller than unity: $|g_n^1| l/n_{1s} \ll 1$. Under these conditions, the problem admits linearization, whereby the distribution function can be represented in the following form:

$$f_1 = f_s(1+\psi), \quad f_s = n_{1s}\left(\frac{\beta_1}{\pi}\right)^{3/2} \exp(-\beta_1 v_1^2). \quad (4)$$

Here, n_{1s} is the saturation concentration of the first component on the surface of evaporation occurring at the temperature T (evidently, $\psi = \psi(x_1, \mathbf{v}_1)$). Taking into account that the problem is stationary and using expression (4), Eq. (3) can be rewritten as

$$v_{1s}\frac{\partial \psi}{\partial x} = \nu_1\left(\frac{\delta n_1}{n_{1s}} - \psi\right), \quad \delta n_1(x) = n_1(x) - n_{1s}, \quad (5)$$

where

$$\frac{\delta n_1(x)}{n_{1s}} = \left(\frac{\beta_1}{\pi}\right)^{3/2} \int \exp(-\beta_1 v^2)\psi(x, v_{1x}) d^3 v_1$$

$$= \frac{1}{\sqrt{\pi}} \int_{-\infty}^{\infty} \exp(-\mu'^2)\psi(x, \mu') d\mu', \quad \mu = C_{1x} = \sqrt{\beta_1} v_{1x}.$$

Now let us consider the boundary condition on the evaporation surface for molecules of the first component, in which the influence of this surface on the process is described by the evaporation coefficient α [10–12]:

$$f_1(0, \mathbf{v}_1) = \alpha f_s(n_{1s}, v_1) + (1-\alpha) f_0(n_0, v_1), \quad v_{1x} > 0. \quad (6)$$

In this expression,

$$f_0 = n_0\left(\frac{\beta_1}{\pi}\right)^{3/2} \exp(-\beta_1 v_1^2)$$

and the quantity n_0 is determined from the condition of nonpercolation for the molecules reflected from the surface without condensation (the probability of this process is $1 - \alpha$),

$$(1-\alpha)\int v_{1x}[f_0(n_0, v_1)\theta_+(v_{1x}) + f(0, \mathbf{v}_1)\theta_+(-v_{1x})] d^3 v_1 = 0,$$

where $\theta_+(x)$ is the Heaviside function [$\theta_+(x) = 1$, $x > 0$; $\theta_+(x) = 0$, $x < 0$].

Using relations (4), the boundary condition (6) can be rewritten as

$$\psi(0, \mathbf{v}_1) = (1-\alpha)\frac{n_0 - n_{1s}}{n_{1s}}, \quad v_{1x} > 0. \quad (7)$$

Then, the form of Eq. (5) and the boundary condition (7) show that function ψ depends only on the component of velocity $\mathbf{v}$ along the x axis: $\psi = \psi(x, v_{1x})$. Introducing the dimensionless coordinate $x = x_1 \nu_1 \sqrt{\beta_1}$ and dimensionless velocity $\mu = \sqrt{\beta_1} v_{1x}$, it is possible to transform Eq. (5) as

$$\mu\frac{\partial \psi}{\partial x} + \psi(x, \mu) = \frac{1}{\sqrt{\pi}} \int_{-\infty}^{\infty} \exp(-\mu'^2)\psi(x, \mu') d\mu', \quad (8)$$

and rewrite the boundary condition on the surface (7) as

$$\psi(0, \mu) = (1-\alpha)a, \quad a = \frac{n_0 - n_{1s}}{n_{1s}}, \quad \mu > 0. \quad (9)$$

Far from the evaporation surface (i.e., outside the Knudsen layer with a thickness on the order of the free path length l), function ψ can be represented in the Chapman–Enskog approximation [8]

$$\psi_0 = G_n(x - \mu) + \varepsilon_n, \quad G_n = \left(\frac{dn_1}{dx}\right)_\infty \frac{1}{n_1 \nu_1 \sqrt{\beta_1}}, \quad \varepsilon_n = \frac{n_1(0) - n_{1s}}{n_{1s}}. \quad (10)$$

Here, $\varepsilon_n = \delta n_1(0)/n_{1s}$ is the relative jump of the concentration of molecules of the first component, $n_1(0)$ is the first component concentration extrapolated to the surface from the solution of hydrodynamic equations, and $\delta n_1(0) = n_1(0) - n_{1s}$.

The quantity a is determined from the nonpercolation condition

$$\int_{-\infty}^{\infty} \exp(-\mu^2)\mu[a\theta_+(\mu) + \psi(0, \mu)\theta_+(-\mu)] d\mu = 0,$$

which yields

$$a\int_0^{\infty} \exp(-\mu^2)\mu d\mu + \int_{-\infty}^{0} \exp(-\mu^2)\mu\psi(0, \mu) d\mu = 0.$$

Replacing function ψ in the second integral by the asymptotic value ψ_{as}, we obtain

$$a = \frac{n_0 - n_{1s}}{n_{1s}} = \frac{\sqrt{\pi}}{\alpha} G_n.$$

Searching for a solution to Eqs. (8)–(10) in form of

$$\psi_\eta(x, \mu) = \exp\left(-\frac{x}{\eta}\right)\Phi(\eta, \mu),$$

we obtain the characteristic equation

$$(\eta - \mu)\Phi(\eta, \mu) = \frac{1}{\sqrt{\pi}}\eta, \quad \int_{-\infty}^{\infty} \exp(-\mu^2)\Phi(\eta, \mu)d\mu = 1.$$

For $\eta \in (-\infty, +\infty)$, the eigenfunctions of this characteristic equation are as follows (see [13]):

$$\Phi(\eta, \mu) = \frac{1}{\sqrt{\pi}}\eta P\frac{1}{\eta - \mu} + \exp(\eta^2)\lambda(\eta)\delta(\eta - \mu),$$

where $\lambda(z)$ is Cercignani's dispersion function [9]:

$$\lambda(z) = 1 + z\frac{1}{\sqrt{\pi}}\int_{-\infty}^{\infty} \frac{\exp(-\tau^2)d\tau}{\tau - z}.$$

Let us represent the solution to Eqs. (8)–(10) in the form of expansion in eigenfunctions $\Phi(\eta, \mu)$,

$$\psi(x, \mu) = \varepsilon_n + G_n(x - \mu) + \int_0^{\infty} \exp\left(-\frac{x}{\eta}\right)\Phi(\eta, \mu)A(\eta)d\eta, \quad (11)$$

where $A(\eta)$ is an unknown function (a coefficient of the continuous spectrum). Substituting the above eigenfunctions into expansion (11), we obtain a singular integral equation with the Cauchy kernel [14]

$$(1 - \alpha)a = \varepsilon_n - G_n\mu + \frac{1}{\sqrt{\pi}}\int_0^{\infty} \frac{\eta A(\eta)d\eta}{\eta - \mu} + \exp(\mu^2)\lambda(\mu)A(\mu) = 0, \quad 0 < \mu < 1.$$

Introducing an auxiliary function

$$N(z) = \frac{1}{\sqrt{\pi}}\int_0^{\infty} \frac{\eta A(\eta)d\eta}{\eta - z}$$

and using the boundary values of $N(z)$ and the dispersion function $\lambda(z)$ on the real semiaxis, we reduce the above singular integral equation to an inhomogeneous boundary-value problem [15]

$$\lambda^+(\mu)[N^+(\mu) + \varepsilon_n - G_n\mu - (1 - \alpha)a] = \lambda^-(\mu)[N^-(\mu) + \varepsilon_n - G_n\mu - (1 - \alpha)a], \quad \mu > 0.$$

For the corresponding homogeneous problem,

$$\frac{X^+(\mu)}{X^-(\mu)} = \frac{\lambda^+(\mu)}{\lambda^-(\mu)}, \quad \mu > 0$$

the solution is [15]

$$X(z) = \frac{1}{z}\exp V(z), \quad V(z) = \frac{1}{\pi}\int_0^{\infty} \frac{\zeta(\tau)d\tau}{\tau - z},$$

$$\zeta(\tau) = \frac{\pi}{2} - \arctan\frac{\lambda(\tau)}{\sqrt{\pi}\tau\exp(-\tau^2)}.$$

Using the homogeneous equation, the inhomogeneous problem can be reduced to determining an analytical function from the nonzero jump at the section:

$$X^+(\mu)[N^+(\mu) + \varepsilon_n - G_n\mu - (1 - \alpha)a] = X^-(\mu)[N^-(\mu) + \varepsilon_n - G_n\mu - (1 - \alpha)a], \quad \mu > 0.$$

The general solution to this problem is

$$N(z) = -\varepsilon_n + G_n z + (1 - \alpha)a + \frac{d_0}{X(z)},$$

where d_0 is an arbitrary constant. For the condition $N(\infty) = 0$, we obtain $d_0 = -G_n$ and $\varepsilon_n = \frac{1}{2}C_n(\alpha)G_n$, where

$$C_n(\alpha) = 2\left[\sqrt{\pi}\frac{1 - \alpha}{\alpha} + V_1\right],$$

$$V_1 = -\frac{1}{\pi}\int_0^{\infty} \zeta(\tau)d\tau = 11.016191.$$

Upon return to the dimensional quantities, we obtain

$$\delta n_1(0) = C_n(\alpha)\sqrt{\beta_1}D_{12}g_n^1, \quad \delta n_1(0) = n_1(0) - n_{1s}. \quad (12)$$

In most investigations, the boundary condition is formulated in a form equivalent to relations (12) [3, 5, 6]. This condition takes into account corrections in the Knudsen number for the hydrodynamic description of the evaporation process. At the same time, other descriptions [1, 2, 11] employ the boundary condition for a concentration jump of type (12) written in an alter-

native form, whereby the left and right sides of Eq. (12) exchange places:

$$D_{12}g_n^1 = \frac{1}{\sqrt{\beta_1}}K_n(\alpha)\delta n_1(0),$$
$$K_n(\alpha) = \frac{\alpha}{2[\sqrt{\pi} + (V_1 - \sqrt{\pi})\alpha]}. \quad (13)$$

In the case of $n_1 \ll n_2$, the boundary condition (13) is formally equivalent to the that used in [1, 2], where (see also [11, 12]) the coefficient $K_n(\alpha)$ (denoted below as $K_n^1(\alpha)$) is expressed as

$$K_n^1\alpha = \frac{\alpha}{2\sqrt{\pi}}. \quad (14)$$

The boundary condition (13) with the coefficient given by formula (14) is called the Hertz–Knudsen boundary condition [11].

Finally, let us compare the obtained analytical solution to the Hertz–Knudsen boundary condition (14). For $\alpha = 1$, the latter condition yields $K_n^1(1) = 0.282095$, while the analytical solution (13) gives $K_n(1) = 0.492044$. As $\alpha \longrightarrow 0$, we have $K_n(\alpha) = \frac{\alpha}{2\sqrt{\pi}}$. Therefore, the values of $K_n(\alpha)$ and $K_n^1(\alpha)$ coincide in the case of small evaporation coefficients.

Acknowledgments. One of the authors (A.V. L.) gratefully acknowledges financial support from the Russian Foundation for Basic Research, project no. 03-01-00281.

REFERENCES

1. G. Yu. Yalamov, Zh. Tekh. Fiz. **74** (2), 41 (2004) [Tech. Phys. **49**, 183 (2004)].
2. Yu. I. Yalamov and A. S. Khassanov, Zh. Tekh. Fiz. **74** (7), 13 (2004) [Tech. Phys. **49**, 818 (2004)].
3. E. R. Shchukin, Yu. I. Yalamov, and Z. L. Shulimanova, *Selected Problems of Physics of Aerosols* (Moscow Pedagogical University, Moscow, 1992) [in Russian].
4. Yu. I. Yalamov, O. N. Zenkina, and M. F. Barinova, Inzh.-Fiz. Zh. **73**, 1295 (2000).
5. E. I. Alekhin and Yu. I. Yalamov, Teplofiz. Vys. Temp. **34**, 487 (1996).
6. E. I. Alekhin and Yu. I. Yalamov, *Mathematical Grounds of the Solution of Boundary Problems in the Kinetic Theory of Multicomponent Gases in the Vicinity of Condensed Phase* (MOPI, Moscow, 1991) [in Russian].
7. A. V. Latyshev and A. A. Yushkanov, Inzh.-Fiz. Zh. **73**, 542 (2000).
8. V. P. Silin, *Introduction to Kinetic Gas Theory* (Nauka, Moscow, 1971) [in Russian].
9. C. Cercignani, *Theory and Application of the Boltzmann Equation* (American Elsevier, New York, 1975).
10. M. N. Kogan, *Dynamics of Rarefied Gases: Kinetic Theory* (Nauka, Moscow, 1967) [in Russian].
11. A. V. Kozyrev and A. G. Sitnikov, Usp. Fiz. Nauk **171**, 765 (2001) [Phys. Usp. **44**, 725 (2001)].
12. J. P. Hirth and G. M. Pound, *Condensation and Evaporation: Nucleation and Growth Kinetics* (Pergamon Press, Oxford, 1963).
13. V. S. Vladimirov and V. V. Zharinov, *Equations of Mathematical Physics* (Fizmatlit, Moscow, 2000) [in Russian].
14. F. D. Gakhov, *Boundary Value Problems* (Nauka, Moscow, 1977; Addison-Wesley, Reading, 1966).
15. A. V. Latyshev and A. A. Yushkanov, *Analytical Solution of Boundary Value Problems of Kinetic Theory* (MGOU, Moscow, 2004) [in Russian].

Translated by P. Pozdeev

Technical Physics Letters, Vol. 30, No. 12, 2004, pp. 1027–1029. Translated from Pis'ma v Zhurnal Tekhnicheskoĭ Fiziki, Vol. 30, No. 24, 2004, pp. 20–25.

Hydrodynamic Modification of Microscopic Biological Objects

G. A. Baranov, A. A. Belyaev, S. B. Onikienko, S. A. Smirnov, and V. V. Khukharev

Efremov Institute of Electrophysical Equipment, St. Petersburg, Russia
State Military-Medical Academy, St. Petersburg, Russia
e-mail: laser@mail.rcom.ru

Received May 26, 2004

Abstract—Hydrodynamic processes leading to transformations of microscopic biological objects have been experimentally studied and numerically simulated. © *2004 MAIK "Nauka/Interperiodica".*

Previously [1, 2], we reported the results of experimental and theoretical investigations of the hydrodynamic and gasdynamic processes induced in aqueous media under the action of laser radiation. The treatment was aimed at destruction of the molecules of dissolved polysaccharides with the formation of molecular fragments possessing high activity in the immunology of infectious and oncological diseases [3]. It was established that there exist both a lower threshold of the laser beam power, corresponding to the onset of depolymerization of large amylopectin molecules, and the upper limit, above which this process ceases.

The macroscopic and microscopic hydrodynamic characteristics were related via a parameter representing the rate of deformation of the liquid medium, $\varepsilon = [(\partial u/\partial x)^2 + (\partial v/\partial y)^2 + (\partial w/\partial z)^2]^{0.5}$. Large molecules occurring in the liquid may change their shape when this parameter acquires a critical value [4]

$$\varepsilon_{cr} = \frac{kT}{\mu \langle h^2 \rangle^{3/2}},$$

where $\langle h^2 \rangle^{1/2}$ is the rms distance between free ends of a molecule, k is the Boltzmann constant, T is the absolute temperature, and μ is the dynamic viscosity. For amylopectin molecules with $\langle h^2 \rangle^{1/2} \approx 0.214$ μm, the critical deformation rate according to formula (1) is on the order of $\varepsilon_{cr} = 500$ s^{-1}. Under conditions studied previously [1, 2], this level was achieved in the waves of compression and rarefaction generated in a liquid medium upon absorption of laser radiation incident on the surface.

In developing a technological process for the laser treatment of polysaccharides, we have determined the range of radiation intensities ensuring the maximum yield of the target product fraction (oligosaccharides). Data presented in the table show a change in the molecular composition of fractions in an Iceland moss solution under laser action, whereby polysaccharides (with molecular weights from 80000 to 400000 amu) are replaced by oligosaccharides of lower molecular weight (from 20000 to 60000 amu). It should be noted that a laser power density above 1 kW/cm^2 leads to burning of a considerable amount of organic compounds, which is usually unacceptable. Adding a polymerization inhibitor into the medium can prevent the reverse process, whereby the modified product spontaneously polymerizes into the initial polymer. This additive may significantly increase the efficiency of utilization of both the radiation power and the initial natural compound. The role of a polymerization inhibitor was performed by ethyl alcohol, which is well compatible with most drugs (for which ethyl alcohol usually is a preservative). It was experimentally established that a 10-vol % additive of ethyl alcohol effectively prevents the polymerization of oligosaccharides formed upon laser-induced degradation of polysaccharides contained in an Iceland moss solution.

In continuation of the previous investigations, we have studied the process of transformation of amylopectin molecules in a flow of water featuring large deformation rates created with the aid of a cone-shaped nozzle. Considerable destructive potential of the cavitation processes taking place in strongly deformed liquid media can be illustrated by severe erosion of propellers and by the loss of micloflora in milk upon cavitation processing. These effects are related to the formation of

Variation of the molecular composition of fractions in an Iceland moss solution under the action of laser radiation

Laser power density, kW/cm^2	Composition of biomaterial, mol %	
	oligosaccharides	polysaccharides
0	24.94	75.05
0.2	24.95	75.04
0.6	30.92	68.06
0.9	34.74	64.49

1063-7850/04/3012-1027$26.00

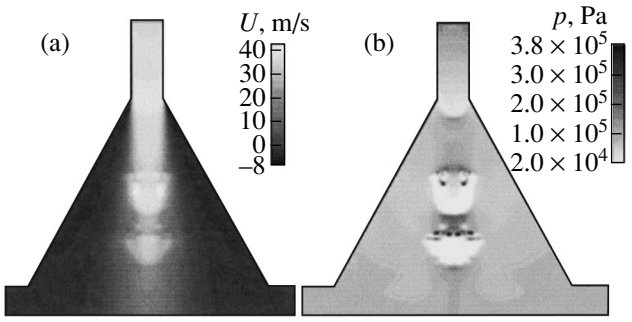

Fig. 1. Numerically calculated distributions of (a) the axial velocity U and (b) the static pressure p in a liquid passing through a cone-shaped nozzle.

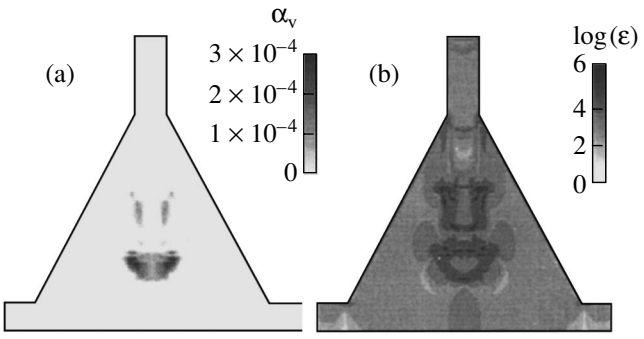

Fig. 2. Numerically calculated distributions of (a) the vapor volume fraction $\alpha_v = 1 - \alpha_1$ and (b) the logarithm of deformation rate $\log(\varepsilon)$ in a liquid passing through a cone-shaped nozzle.

bubbles in the regions of rarefaction in the liquid, followed by their collapse in the regions of compression, which leads to the development of large local pressures. The deformation and splitting of such cavitation bubbles may also lead to the appearance of uncompensated local discharges initiating sonochemical reactions [4, 5].

In this study, hydrodynamic processes were described within the framework of a macroscopic model of the two-phase medium featuring a cavitating axisymmetric flow [6]. The structure of the medium on the scale of cavitation bubbles is not considered.

The experiments were performed using nozzles comprising the initial cylindrical channel with a length of 3 mm and a diameter of 0.5–2 mm followed by a cone with an opening angle of $\alpha = 60°$. In the experimental setup, the nozzle was connected to a vessel containing an aqueous solution of amylopectin. The pressure in the liquid container was controlled using a pipeline with a manometer, valves, and a reducer, connected to a high-pressure vessel containing nitrogen. After admitting nitrogen to a preset excess pressure ranging within 1–10 bar, the aqueous solution was allowed to pass through the nozzle. The discharge was collected and analyzed with respect to molecular fractions.

The mathematical model included a system of nonstationary Navier–Stokes equations,

$$\frac{\partial}{\partial t}(\rho_m u_i) + \frac{\partial}{\partial x_j}(\rho_m u_i u_j) = -\frac{\partial p}{\partial x_j} + \frac{\partial}{\partial x_j}\left[(\mu + \mu_t)\left(\frac{\partial u_i}{\partial x_j} + \frac{\partial u_j}{\partial x_i}\right)\right], \quad (1)$$

the equation of continuity

$$\frac{\partial \rho_m}{\partial t} + \frac{\partial(\rho_m u_i)}{\partial x_i} = 0, \quad (2)$$

and the equation of transfer of the liquid volume fraction

$$\frac{\partial \alpha_1}{\partial t} + \frac{\partial}{\partial x_i}(\alpha_1 u_i) = (m^+ - m^-), \quad (3)$$

$$\rho_m = \rho_1 \alpha_1 + \rho_v(1 - \alpha_1), \quad (4)$$

where t is the time; x is the coordinate; $u_{i,j}$ are the velocity components; p is the pressure; ρ_m is the effective density; ρ_1 is the liquid density; ρ_v is the vapor density; μ is the dynamic (laminar) viscosity; μ_t is the turbulent viscosity; α_1 is the liquid volume fraction; m^+ is the rate of evaporation; and m^- is the rate of condensation [6]. In contrast to [6], where the turbulent viscosity was calculated using the nonequilibrium k–ε turbulence model, we used the k–ω model [7], which provides for a more satisfactory description of flows featuring free turbulence zones:

$$\mu_t = \frac{C_\mu \rho_m k}{\omega},$$
$$\frac{\partial \rho_m k}{\partial t} + \frac{\partial \rho_m u_i k}{\partial x_i} = P\rho_m - \rho_m \omega k + \nabla\left[\left(\mu + \frac{\mu_t}{\sigma_k}\right)\nabla k\right], \quad (5)$$

$$\frac{\partial \rho_m \omega}{\partial t} + \frac{\partial \rho_m u_i \omega}{\partial x_i} = C_{\omega_1}\frac{\rho_m P \omega}{k} - C_{\omega_2}\rho_m \omega^2 + \nabla\left[\left(\mu + \frac{\mu_t}{\sigma_\omega}\right)\nabla \omega\right]. \quad (6)$$

Here, P is the turbulent energy source, k is the kinetic turbulent energy, ω is the specific rate of dissipation of the turbulent energy, and $C_\mu = 0.09$, $C_{\omega_2} = 0.833$, $C_{\omega_1} = 0.555$, and $\sigma_k = \sigma_\omega = 2.0$ are constant coefficients.

Figures 1 and 2 show the results of numerical calculations of instantaneous distributions of the axial flow velocity U, the static pressure p, the vapor phase volume fraction $\alpha_v = 1 - \alpha_1$, and the logarithm of the deformation rate ε. The nonstationary problem was solved for a nozzle with a cylindrical channel diameter of 0.5 mm, an excess pressure of 7×10^5 Pa at the cone entrance, and an initial pressure of 10^5 Pa in the nozzle.

As can be seen, two zones with strongly inhomogeneous gasdynamic parameters are formed in the cone section, featuring anomalously high local axial velocity and strong rarefaction ($\sim 2 \times 10^4$ Pa) (Fig. 1). The pressure distribution is consistent with the vapor phase distribution (Fig. 2a). Calculations with neglect of the cavitation lead to the appearance of negative pressures. In the regions of cavitation, the deformation rate reaches maximum values (Fig. 2b), which are three to four orders of magnitude higher than the values obtained previously in the calculations for water under the action of laser radiation [1, 2]. Therefore, it can be expected that, even in the relatively simple system under consideration, the cavitating flow will ensure highly effective modification of microscopic biological objects in the liquid phase.

In the experimental setup created on the basis of model calculations, we used a nozzle with a 0.5-mm-diameter entrance cylinder and a 60°-divergent cone. The results of experiments confirmed the possibility of modification of microscopic biological objects. In particular, it was established that there is an interval of optimum excess pressures (4–6 bar) in front of the nozzle, which provided for a 1.5-fold increase in the biological activity of yeast species in the reaction of inhibition of leukocyte migration with antigens of the yeast culture supernatant, as well as an increase in the yeast culture mass and in the yield of metabolites (carbon monoxide and ethyl alcohol). The mechanism of yeast transformation is analogous to that for polysaccharides, whereby the modification is caused by intense mechanical action upon the yeast cell. However, the mechanical action in this case induces normal cell response to stress, manifested by activation of metabolic processes, rather than leading to degradation of the molecular structure.

Conclusions. (i) We have constructed a model describing nonstationary axisymmetric flow of a two-phase cavitating liquid in a system of the water–vapor–noncondensing gas type. (ii) Numerical calculation of the deformation field in the cavitation regions shows the presence of extremely high deformation rate zones in water. (iii) It has been experimentally established that there is an interval of the optimum excess pressures in liquid in front of the nozzle, which provides for an increase in the biological activity of a yeast culture that passes through the nozzle.

Acknowledgments. This study was supported by the Russian Foundation for Basic Research, project no. 01-01-00325.

REFERENCES

1. G. A. Baranov, A. A. Belyaev, S. B. Onikienko, *et al.*, Pis'ma Zh. Tekh. Fiz. **28** (17), 25 (2002) [Tech. Phys. Lett. **28**, 719 (2002)].
2. G. A. Baranov, A. A. Belyaev, S. B. Onikienko, *et al.*, Pis'ma Zh. Tekh. Fiz. **29** (13), 57 (2003) [Tech. Phys. Lett. **29**, 554 (2003)].
3. G. A. Baranov, S. B. Onikienko, V. V. Khukharev, *et al.*, in *Proceedings of the 8th International Congress of European Medical Laser Association (EMLA) and the 1st Russian Congress of Medical Laser Association, Moscow, 2001*, pp. 15–16.
4. G. K. Batchelor, in *Proceedings of the 14th International IUTAM Congress* (Mir, Moscow, 1979), pp. 136–187.
5. M. A. Margulis, Usp. Fiz. Nauk **170**, 263 (2000) [Phys. Usp. **43**, 259 (2000)].
6. I. Senocak and W. A. Shyy, in *Proceedings of the 31st AIAA Fluid Dynamics Conference & Exhibit, Anaheim, 2001,* AIAA Pap. No. 2001–2907.
7. D. C. Wilcox, *Turbulence Modeling for CFD* (DCW Industries, California, 1998).

Translated by P. Pozdeev

Technical Physics Letters, Vol. 30, No. 12, 2004, pp. 1030–1032. Translated from Pis'ma v Zhurnal Tekhnicheskoĭ Fiziki, Vol. 30, No. 24, 2004, pp. 26–30.

Simultaneous Interface and Interband Lasing in InAs/InAsSbP Heterostructures Grown by Metalorganic Vapor Phase Epitaxy

A. P. Astakhova, N. D. Il'inskaya, A. N. Imenkov, S. S. Kizhaev, S. S. Molchanov, and Yu. P. Yakovlev

Ioffe Physicotechnical Institute, Russian Academy of Sciences, St. Petersburg, 194021 Russia

e-mail: serguie@mail.ru

Received July 14, 2004

Abstract—Coherent radiation sources have been manufactured based on double heterostructures of the InAs/InAsSbP type grown by metalorganic vapor-phase epitaxy. The mode composition of the lasing spectrum is determined by simultaneous induced recombination at the heteroboundary and in the bulk of the active region, as well as nongenerated modes with intermediate frequencies. Additional optical losses at the intermediate modes decrease the slope of the laser intensity dependence on the current. © *2004 MAIK "Nauka/Interperiodica".*

Middle-IR radiation sources emitting in the wavelength interval 3–4 μm can be used in numerous applications. As is known, the molecules of hydrocarbons and many other industrial and natural gases (such as CO, CO_2, H_2S, SO_2, NO, and NO_2) exhibit optical absorption in the indicated spectral range. Therefore, the above IR radiation sources can serve as a basis for the development of effective methods of gas analysis for technological process control and environmental monitoring. Although spontaneous radiation sources can stably operate in the indicated spectral range at room temperature, some special applications (such as high-resolution molecular spectroscopy, coherent signal processing, etc.) require radiation with a narrow spectrum width (10^{-3}–10^{-2} Å). This study opens a systematic investigation into the properties of coherent radiation sources based on heterostructures synthesized by metalorganic vapor-phase epitaxy (MOVPE).

Previously, Baranov *et al.* [1] reported on the electroluminescent characteristics of lasers based on GaInAsSb/GaAlAsSb type I and II heterostructures, Aidaraliev *et al.* [2] studied the mechanisms of radiative recombination in lasers based on InGaAsSb/InAsSbP type I and II heterostructures, and Krier *et al.* [3] observed interface electroluminescence in light-emitting diodes based on InAs/InAsSbP heterostructures. This paper presents the results of investigation of the spectral characteristics of coherent radiation generated by diodes based on double heterostructures of the InAs/InAsSbP type grown by MOVPE.

The epitaxial layers were grown at atmospheric pressure in a horizontal reactor on substrates mounted in a molybdenum substrate holder equipped with a resistive heater. The substrates were (100)-oriented InAs plates (no. AR-388) with a hole density of $p = (5–9.4) \times 10^{18}$ cm^{-3}. The epitaxial heterostructure comprised a zinc-doped barrier layer of $InAs_{0.53}Sb_{0.15}P_{0.32}$ with $p = 2 \times 10^{18}$ cm^{-3}, followed by an undoped InAs active region and undoped $InAs_{0.53}Sb_{0.15}P_{0.32}$ barrier. The charge carrier density in the active region was $n = 2 \times 10^{16}$ cm^{-3} and in the undoped barrier, $n = 1.3 \times 10^{17}$ cm^{-3}. The epitaxially grown active region had a thickness of 3.3 μm, and each of the two barrier layers was 3.5 μm thick.

Radiation sources with a double-channel mesastripe design were manufactured using conventional photolithographic and wet etching technology. Fabry–Perot resonators with a length of 350 μm in the chips were manufactured by cleavage. The distance between grooves was 20 μm, while the contact strip width was 5–6 μm. The ohmic contacts on the *p*- and *n*-regions were formed by vacuum deposition of a multilayer metal composition (Cr–Au–Ni–Au). The optimum insulating material was selected using a series of samples coated with photoresist, polyamide, and silicon nitride. A comparison of the diode characteristics showed that the best results were obtained with Si_3N_4 layer with a thickness of ~1000–1100 Å.

The spectral characteristics of diodes were studied at 77 K. The diodes were powered by a pulsed current with a pulse width of $\tau = 500$ ns and a pulse repetition rate of $f = 2$ kHz. The output radiation was analyzed by grating monochromator and detected by an InSb photodiode cooled with liquid nitrogen. The radiation intensity was measured using a lock-in detection scheme.

1063-7850/04/3012-1030$26.00 © 2004 MAIK "Nauka/Interperiodica"

Figure 1 shows a schematic energy band diagram of the heterostructure under consideration. As is known, the presence of each heterobarrier in a light-emitting structure leads to the formation of new channels of both radiative and nonradiative recombination. It can be expected that one possible mechanism of radiative recombination in semiconductor structures with type II heterojunctions is related to the electron–hole interaction at the *N*-InAsSbP/*n*-InAs heteroboundary. According to Baranov *et al.* [4–6], application of a direct bias voltage greater than E_g/e leads to the formation of self-consistent spatially separated potential wells for electrons and holes in *n*-InAs near the *n*-InAs/*N*-InAsSbP heteroboundary. In such a system, coherent lasing is provided by radiative transitions between quantum states in the potential wells.

Figure 2 shows the emission spectra of a diode with $L = 350$ μm measured for various diode currents. The inset presents a plot of the emission intensity versus diode current. As can be seen, the threshold current is $I_{th} = 0.425$ A. At a current of $I = 0.51$ A, the spectrum consists of a single mode with $\lambda \sim 3.097$ μm. An increase in the diode current leads to the appearance of a new mode with $\lambda \sim 3.087$ μm, which becomes predominant at $I = 0.55$ A and above. As the current grows further ($I = 0.73$ A), an additional mode arises at $\lambda \sim 3.094$ μm. The slope of the plot of emission intensity versus diode current in the interval 0.425–0.55 A is eight times greater than in the interval 0.55–1.5 A (see insert in Fig. 2). This behavior indicates that the efficiency of diodes operating at currents $I < 0.55$ A is higher than the efficiency for $I > 0.55$ A. A decrease in slope of the emission intensity versus current plot correlates with the appearance of a new laser mode with $\lambda \sim 3.087$ μm (the long-wavelength emission mode with $\lambda \sim 3.097$ μm is also retained).

The phenomenon of lasing with an intermediate wavelength of $\lambda = 3.094$ μm is rather unusual. The long-wavelength mode probably corresponds to the radiative recombination the interface, since it appears at the maximum of the spontaneous band. The short-wavelength mode with $\lambda = 3.084$ μm is apparently related to interband transitions. A sharp decrease in the rate of the emission intensity growth with increasing diode current at $I > 0.55$ A can be explained by the interaction between modes of the interface and interband radiative recombination. The presence of intermediate modes can be also assigned to the interaction of interface and interband modes. A correlation between the observed decrease in the slope of the total emission intensity and the appearance of the interband and intermediate modes can be related to strong absorption of the nongenerated intermediate modes.

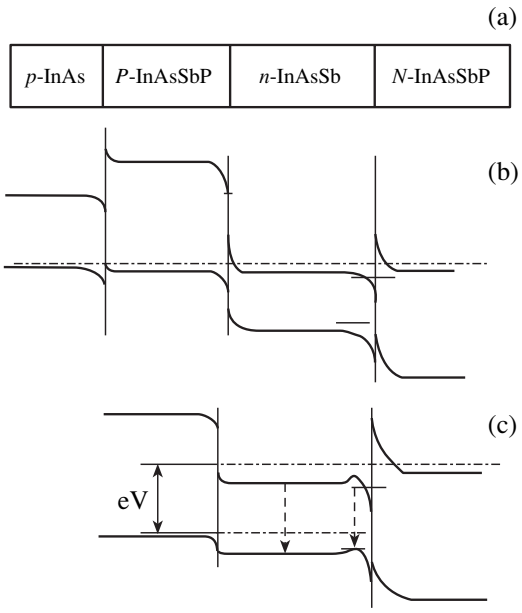

Fig. 1. Diodes based on InAs/InAsSbP heterostructures: (a) schematic diagram of layers; (b, c) energy band diagrams of diode structures in the zero-bias and lasing regime, respectively.

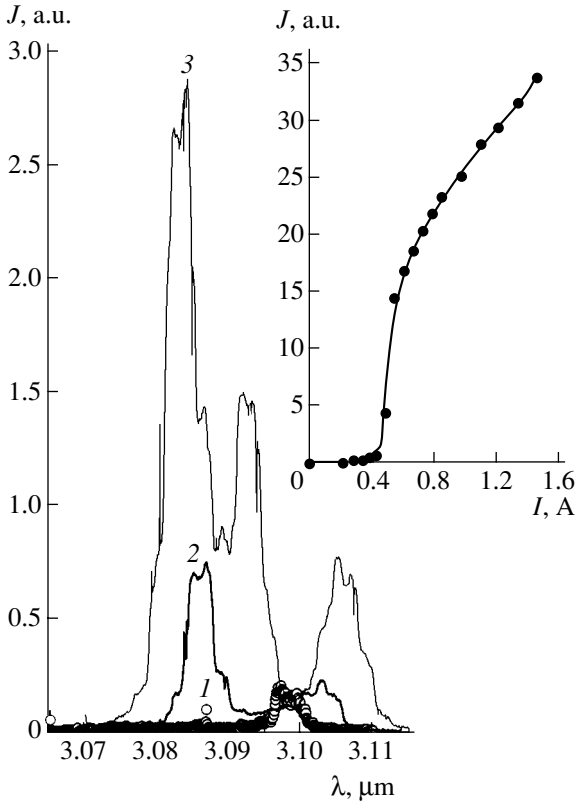

Fig. 2. Electroluminescence spectra of diodes measured at 77 K for various diode currents *I* (A): (*1*) 0.51; (*2*) 0.55; (*3*) 0.73. The insets show a plots of the emission intensity *J* versus diode current.

Acknowledgments. This study was supported by the Russian Foundation for Basic Research (project no. 02-02-17633) an by the US Civilian Research and Development Foundation for the Independent States of the Former Soviet Union (CRDF grant no. RPO-1407-ST-03).

REFERENCES

1. A. N. Baranov, B. E. Dzhurtanov, A. N. Imenkov, *et al.*, Pis'ma Zh. Tekh. Fiz. **13**, 517 (1987) [Sov. Tech. Phys. Lett. **13**, 213 (1987)].
2. M. Aĭdaraliev, N. V. Zotova, S. A. Karandashev, *et al.*, Fiz. Tekh. Poluprovodn. (St. Petersburg) **33**, 233 (1999) [Semiconductors **33**, 200 (1999)].
3. A. Krier and V. V. Sherstnev, J. Phys. D **33**, 101 (2000).
4. A. N. Baranov, B. E. Dzhurtanov, A. N. Imenkov, *et al.*, Pis'ma Zh. Tekh. Fiz. **12**, 664 (1986) [Sov. Tech. Phys. Lett. **12**, 275 (1986)].
5. A. N. Baranov, B. E. Dzhurtanov, A. N. Imenkov, *et al.*, Fiz. Tekh. Poluprovodn. (Leningrad) **20**, 2217 (1986) [Sov. Phys. Semicond. **20**, 1385 (1986)].
6. A. N. Baranov, T. N. Danilova, O. G. Ershov, *et al.*, Pis'ma Zh. Tekh. Fiz. **18** (22), 6 (1992) [Sov. Tech. Phys. Lett. **18**, 725 (1992)].

Translated by P. Pozdeev

Technical Physics Letters, Vol. 30, No. 12, 2004, pp. 1033–1035. Translated from Pis'ma v Zhurnal Tekhnicheskoĭ Fiziki, Vol. 30, No. 24, 2004, pp. 31–37.

Photoluminescence of GaAsP/GaInAsP Type-II Heterojunctions

D. A. Vinokurov*, S. A. Zorina, V. A. Kapitonov, A. V. Murashova, D. N. Nikolaev, A. L. Stankevich, M. K. Trukan, V. V. Shamakhov, and I. S. Tarasov

Ioffe Physicotechnical Institute, Russian Academy of Sciences, St. Petersburg, 194021 Russia

** e-mail: dmitry.vinokurov@pop.ioffe.rssi.ru*

Received July 15, 2004

Abstract—We have studied the photoluminescence of heterostructures based on solid solution systems of the GaInP/GaAsP/GaInAsP type grown by metalorganic chemical vapor deposition method. It is established that $GaAs_{0.77}P_{0.23}$ and $Ga_{0.74}In_{0.26}As_{0.53}P_{0.47}$ solid solutions form a type-II heterojunction. The conduction band offset at the $GaAs_{0.77}P_{0.23}/Ga_{0.74}In_{0.26}As_{0.53}P_{0.47}$ heteroboundary amounts to 90 meV, which makes the quaternary solid solution a preferred material for the active region of a laser heterostructure operating at λ = 780 nm. © *2004 MAIK "Nauka/Interperiodica".*

High-power laser diodes operating in the 730–810 nm wavelength range are usually fabricated using heterostructures with active regions based on GaAsP [1, 2] or GaInAsP [3, 4] solid solutions. The output power of such diodes is limited primarily by the thermal injection of charge carriers from quantum wells (QWs) into waveguide regions. The efficiency of the thermal injection of carriers is determined by the depth of the energy levels in QWs for electrons and holes relative to the waveguide energy level. This injection process is especially important for electrons, which possess much lower effective masses than holes. Thus, in cases when it is possible to use various solid solutions as base materials for the active regions providing for the same working wavelength, it can be recommended to take into account the depth of energy levels for charge carriers in QWs relative to the selected waveguide.

This paper reports on the results of investigation of the photoluminescence (PL) of type-II heterojunctions formed by $GaAs_{0.77}P_{0.23}$ and $Ga_{0.74}In_{0.26}As_{0.53}P_{0.47}$ solid solutions, which can be used as materials for the active region of a laser heterostructure operating at λ = 780 nm. The study was aimed at determining the conduction band offset at the heteroboundary between the two materials.

The samples for the PL investigation were prepared in an Encore GS3100 metalorganic chemical vapor deposition (MOCVD) system with a vertical reactor. The growth was performed at a reduced pressure (77 Torr), a substrate holder rotation rate of 1000 rpm, and a substrate temperature of 700°C. The sample heterostructures grown on (100)-oriented *n*-GaAs substrates represented strained single QWs of $GaAs_{0.77}P_{0.23}$ ($\Delta a/a$ = –0.8%) or $Ga_{0.74}In_{0.26}As_{0.53}P_{0.47}$ ($\Delta a/a$ = 0.2%) solid solutions, or $GaAs_{0.77}P_{0.23}/Ga_{0.74}In_{0.26}As_{0.53}P_{0.47}/GaAs_{0.77}P_{0.23}$ *W*-type QWs confined between the layers of wide-bandgap solid solution $Ga_{0.51}In_{0.49}P$. The thickness of single QWs ($GaAs_{0.77}P_{0.23}$ and $Ga_{0.74}In_{0.26}As_{0.53}P_{0.47}$) was ~100 Å, and the thickness of *W*-type QWs was about 300 Å (three 100-Å-thick layers).

The results of our previous calculations using a model developed by Krijn [5] showed that QWs formed by the quaternary solid solution $Ga_{0.74}In_{0.26}As_{0.53}P_{0.47}$ in a waveguide layer of $Ga_{0.51}In_{0.49}P$ are characterized by a greater depth of energy levels as compared to that for analogous QWs based on the ternary solid solution $GaAs_{0.77}P_{0.23}$ [6]. The results of calculations were confirmed by the experimentally measured PL spectra [6], which showed that the intensity of emission from a QW formed by the quaternary solid solution $Ga_{0.74}In_{0.26}As_{0.53}P_{0.47}$ is about three times that for the analogous QW formed by the ternary solid solution $GaAs_{0.77}P_{0.23}$. The calculations also suggested that these solid solutions in contact must form a type-II heterojunction. In order to confirm this hypothesis, we performed experiments with heterostructures containing *W*-type QWs.

Figure 1 shows a schematic diagram of the energy band structure of the experimental heterostructure with a *W*-type QW and indicates the dimensional quantization levels and the possible optical transitions in this system, calculated for strained QWs using the model [5]. The bandgap widths at 77 K were calculated using the interpolation relations [7]. The results of calculations showed that this QW may feature both radiative interband transitions corresponding to a single QW (*A*-type transitions) with a photon energy of 1.67 eV (77 K) and indirect (tunneling) radiative transitions at the $GaAs_{0.77}P_{0.23}/Ga_{0.74}In_{0.26}As_{0.53}P_{0.47}$ type-II heterojunction (*B*-type transitions) with a photon energy of 1.6 eV (77 K), which is significantly smaller than the bandgap

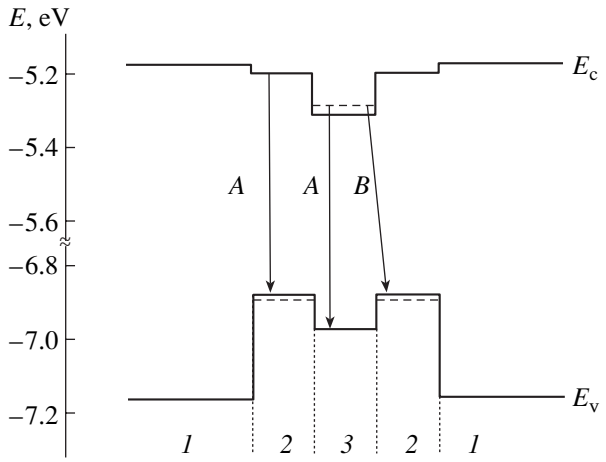

Fig. 1. Schematic energy band diagrams of a double heterostructure comprising a wide-bandgap waveguide and a *W*-type QW: (*1*) $Ga_{0.51}In_{0.49}P$; (*2*) $GaAs_{0.77}P_{0.23}$; (*3*) /$Ga_{0.74}In_{0.26}As_{0.53}P_{0.47}$. Dashed lines show the levels of dimensional quantization; arrows indicate (*A*) the interband radiative transitions corresponding to a single QW and (*B*) indirect (tunneling) radiative transitions at the GaAsP/GaInAsP type-II heterojunction.

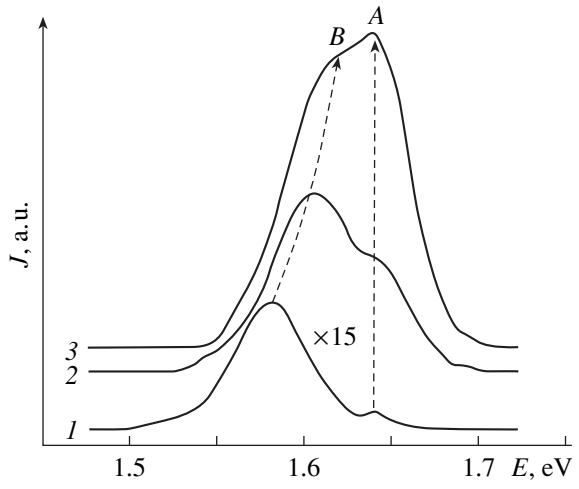

Fig. 2. PL spectra of a heterostructure with the *W*-type QW measured at 77 K for various excitation intensities (W/cm^2): (*1*) 1.5; (*2*) 7; (*3*) 10. Arrows indicate the bands of radiative transitions of the *A* and *B* types.

width of solid solutions forming the heteroboundary. Electrons localized in the QW of $Ga_{0.74}In_{0.26}As_{0.53}P_{0.47}$ recombine with light holes localized in the QW of $GaAs_{0.77}P_{0.23}$. The presence of light holes is related to the fact that $GaAs_{0.77}P_{0.23}$ is compression-strained relative to the GaAs substrate.

Figure 2 shows transformation of the PL spectrum of a *W*-type QW depending of the optical excitation intensity (1.5–15 W/cm^2) at 77 K. As can be seen, the PL spectrum measured at a low excitation level (1.5 W/cm^2) exhibits two clearly separated peaks. One of these, corresponding to a photon energy of 1.655 eV, is due to *A*-type interband radiative transitions (Fig. 1). The emission peak caused by the *A*-type transitions (peak *A*) is shifted toward lower energies relative to the PL peaks in the spectra of single QWs $GaAs_{0.77}P_{0.23}$ and $Ga_{0.74}In_{0.26}As_{0.53}P_{0.47}$ (with an experimental photon energy of 1.68 eV at 77 K). This is related to the fact that *W*-type QWs, in contrast to the corresponding single QWs, contain no dimensional quantization levels in the valence band of $Ga_{0.74}In_{0.26}As_{0.53}P_{0.47}$ and in the conduction band of $GaAs_{0.77}P_{0.23}$. The second peak (peak *B*) corresponds to transitions with a photon energy of 1.59 eV and is related, in our opinion, to indirect radiative transitions at the $GaAs_{0.77}P_{0.23}/Ga_{0.74}In_{0.26}As_{0.53}P_{0.47}$ type-II heterojunction (*B*-type transition in Fig. 1). The relatively high intensity of these transitions is explained by the localization of charge carriers in the vicinity of type-II heterojunctions due the Coulomb attraction between electrons and holes [8]. The maximum of the PL band related to the *B*-type transitions is shifted by 65 meV toward lower energies relative to the band of the *A*-type transitions. This shift corresponds to the energy difference between the bottom of the conduction band of $GaAs_{0.77}P_{0.23}$ and the dimensional quantization level for electrons in $Ga_{0.74}In_{0.26}As_{0.53}P_{0.47}$. The same difference (65 meV) is observed between the top of the valence band of $Ga_{0.74}In_{0.26}As_{0.53}P_{0.47}$ and the dimensional quantization level for holes in $GaAs_{0.77}P_{0.23}$. The conduction band offset at the heteroboundary between $GaAs_{0.77}P_{0.23}$ and $Ga_{0.74}In_{0.26}As_{0.53}P_{0.47}$ can be evaluated as a sum of the energy difference between *A*- and *B*-type transitions (estimated at 65 meV) and the energy of the quantization level for electrons in $Ga_{0.74}In_{0.26}As_{0.53}P_{0.47}$ (according to our calculations, about 25 meV). Thus, the conduction band offset at the heteroboundary is about 90 meV (to within the error of determination of the quantization energy for electrons). As the pumping intensity increases, the position of peak *A* remains virtually unchanged, whereas peak *B* shifts toward higher energies and approaches the former peak. The observed blue shift is characteristic of type-II heterojunctions [9]. It should be also noted that, as the excitation intensity grows, the height of peak *B* increases at a slower rate than does peak *A*, so that beginning with a certain excitation level (about 15 W/cm^2) the latter transitions predominate in the PL spectrum.

We have also studied the behavior of the PL spectra of single QWs ($GaAs_{0.77}P_{0.23}$ and $Ga_{0.74}In_{0.26}As_{0.53}P_{0.47}$) and the *W*-type QWs depending on the temperature in the interval from 77 to 300 K. Figure 3 shows the PL spectrum of a *W*-type QW measured at various temperatures for a constant optical excitation intensity of 3 W/cm^2. An increase in the temperature is accompanied by redistribution of the relative peak intensities in the PL spectrum. The intensity of peak *B* related to the transitions at the type-II heterojunction decreases with

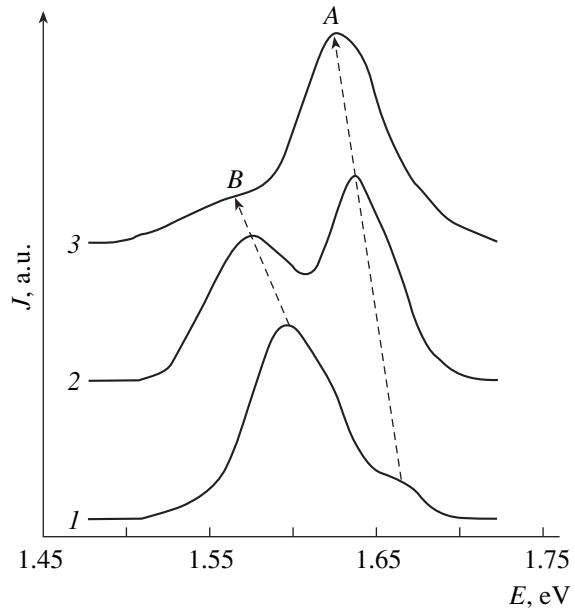

Fig. 3. PL spectra of a heterostructure with the *W*-type QW measured for the same excitation intensity (3 W/cm^2) at various temperatures (K): (*1*) 77; (*2*) 120; (*3*) 210. Arrows indicate the bands of radiative transitions of the *A* and *B* types.

increasing temperature, whereas the intensity of peak *A* related to the radiative transitions in a single QW increases. Peak *B* vanishes at 260°C. At this temperature, the position of peak *A* changes in the same manner as the position of PL peaks in the spectra of single QWs ($GaAs_{0.77}P_{0.23}$ and $Ga_{0.74}In_{0.26}As_{0.53}P_{0.47}$). We believe that the disappearance of peak *B* reflects a drop in the probability of the corresponding radiative transitions. This is related to a decrease in the degree of charge carrier localization at the $GaAs_{0.77}P_{0.23}/Ga_{0.74}In_{0.26}As_{0.53}P_{0.47}$ type-II heterojunction, which is caused by a decrease in the Coulomb interaction between electrons and holes with increasing temperature.

To summarize, the results of our PL measurements showed that $GaAs_{0.77}P_{0.23}$ and $Ga_{0.74}In_{0.26}As_{0.53}P_{0.47}$ solid solution form a type-II heterojunction. The conduction band offset at the $GaAs_{0.77}P_{0.23}/Ga_{0.74}In_{0.26}As_{0.53}P_{0.47}$ heterojunction is about 90 meV. It was concluded that the QW for electrons formed by the quaternary solid solution $Ga_{0.74}In_{0.26}As_{0.53}P_{0.47}$ is deeper than that formed by the ternary solid solution $GaAs_{0.77}P_{0.23}$ relative to any selected waveguide material. For this reason, said quaternary material is a preferred material for the active region of a laser heterostructure operating at λ = 780 nm from the standpoint of suppression of the process of carrier injection from QWs into the waveguide region.

Acknowledgments. This study was supported by the Russian Foundation for Basic Research, project no. 04-02-17641.

REFERENCES

1. G. Elbert, F. Bugge, A. Knauer, *et al.*, IEEE J. Sel. Top. Quantum Electron. **5**, 780 (1999).
2. F. Agahi, K. M. Lau, H. K. Choi, *et al.*, IEEE Photonics Technol. Lett. **7**, 140 (1995).
3. L. J. Mawsi, S. Rusli, A. Al-Muhanna, and J. K. Wade, IEEE J. Sel. Top. Quantum Electron. **5**, 785 (1999).
4. J. Diaz, H. J. Yi, M. Razeghi, and G. T. Burnham, Appl. Phys. Lett. **71**, 3042 (1997).
5. M. P. C. M. Krijn, Semicond. Sci. Technol. **6**, 27 (1991).
6. D. A. Vinokurov, S. A. Zorina, V. A. Kapitonov, *et al.*, Fiz. Tekh. Poluprovodn. (St. Petersburg) **37**, 1473 (2003) [Semiconductors **37**, 1421 (2003)].
7. S. S. Strel'chenko and V. V. Lebedev, *III–V Group Compounds: A Handbook* (Metallurgiya, Moscow, 1984) [in Russian].
8. A. Joullie, E. M. Skouri, M. Garcia, *et al.*, Appl. Phys. Lett. **76**, 2499 (2000).
9. K. D. Moiseev, B. Ya. Mel'tser, V. A. Solov'ev, *et al.*, Pis'ma Zh. Tekh. Fiz. **24** (12), 50 (1998) [Tech. Phys. Lett. **24**, 477 (1998)].

Translated by P. Pozdeev

Technical Physics Letters, Vol. 30, No. 12, 2004, pp. 1036–1038. Translated from Pis'ma v Zhurnal Tekhnicheskoĭ Fiziki, Vol. 30, No. 24, 2004, pp. 38–42.

The Surface Energy Deposited into Gas during Initiation of a Pulsed Plasma Sheet Discharge

I. A. Znamenskaya, A. E. Lutskiĭ, and I. V. Mursenkova

Department of Physics, Moscow State University, Moscow, 119899 Russia

Keldysh Institute of Applied Mathematics, Russian Academy of Sciences, Moscow, 125047 Russia

e-mail: @phys.msu.ru; @kiam.ru

Received July 1, 2004

Abstract—Gasdynamic perturbations arising during the initiation of a pulsed surface (plasma sheet) discharge have been experimentally studied in a shock tube. The evolution of flow was also numerically simulated within the framework of a thermal energy deposition model. Experimental values of the velocity of perturbations well agree with the results of calculations obtained assuming that about 50% of the energy deposited in the surface layer is converted into heat in the stage of energy supply. *© 2004 MAIK "Nauka/Interperiodica".*

By initiating a pulsed surface discharge of the plasma sheet type (comprising a system of channels sliding over a dielectric surface) in a gasdynamic flow, it is possible to model and study in experiment the process of pulsed energy deposition in the boundary layer of a gas flow [1, 2]. This type of discharge is used, for example, as plasma electrode in gas-discharge and excimer lasers [3, 4] and offers a good distributed source of UV radiation ensuring homogeneous preionization of the main discharge volume.

In order to take into account the influence of the surface energy supply on the flow in the boundary layer, it is necessary to analyze the dynamics of gas heating after initiation of the plasma sheet discharge. The mechanism of conversion of the electric energy of a pulsed discharge into the enthalpy of flow is related to a complicated, ambiguously determined kinetics of the nonequilibrium excited plasma region.

Irrespective of the method of excitation of pulsed discharge in a medium, there arise gasdynamic excitations caused by rapid energy deposition in a finite volume. Investigations of the medium in the discharge gap of a CO_2 laser with two plasma electrodes showed that perturbations in the form of weak shock waves with a Mach number of M = 1.2–1.3 appeared after initiation of the plasma sheet discharge [5]. Interferometric measurements revealed smooth fronts of the shock waves at a considerable width of the wave front, which could result from a large optical path of the probing beam in the perturbed region (800 mm): the direction of optical probing was perpendicular to the direction of propagation of the sliding discharge.

The aim of this study was to evaluate the fraction of energy directly introduced into gas near the surface during initiation of a pulsed plasma sheet discharge. This task was solved by studying the dynamics of shock waves generated in the system.

Experimental study of the dynamics of perturbations arising during the initiation of a sliding surface (plasma sheet) discharge. We have experimentally studied the dynamics of perturbations generated by plasma sheets formed by pulsed discharges sliding along the surface. The process was monitored in a gasdynamic channel along the axis parallel to the direction of propagation of the sliding discharge. The experiments were performed in a shock tube with a discharge chamber (working unit). The inner region of the discharge chamber was a continuation of the low-pressure chamber of the shock tube with a 24×48 mm cross section. In a 17-cm-long portion of the tube, the opposite walls were made of plane-parallel quartz plates flush mounted so that the channel cross section remained unchanged.

Plasma sheets with dimensions 35×100 mm were initiated on the opposite walls of the working unit and were spaced 24 mm from each other. A pulsed voltage with an amplitude of 30 kV was applied to the electrodes of sliding discharges. The working gas was air at an initial pressure of about 100 Torr. The shock waves arising from plasma sheets near electrodes were visualized and their dynamics was monitored using the shadow and schlieren images of the discharge gap obtained at various moments of time past the sliding discharge initiation. The probing radiation beam was generated by a multimode pulsed ruby laser operating at λ = 0.6943 nm, E = 0.64 J, and $\tau_{1/2}$ = 20 ns. The scheme of synchronization provided probing of the discharge volume with a delay time controlled within 0–100 μs relative to the current pulse initiating the sliding discharge, with simultaneous monitoring of the pulse of discharge current.

1063-7850/04/3012-1036$26.00 © 2004 MAIK "Nauka/Interperiodica"

An analysis of the experimental data showed that an energy of ~0.6 J is deposited in each plasma sheet within a 100-ns-long period of time. The pressure jump initiates a system of hemicylindrical shock waves on the surface. The fronts of these shock waves interfere with each other for ~10 μs to form a smooth quasi-flat front of the shock wave envelope. Figure 1 presents a shadow image of this perturbed region 12 μs after initiation of the surface discharge. Distortions of the wave front correspond to hemicylindrical shock wave fronts from some (most intense) sliding discharges.

The dynamics of motion of the wave fronts was revealed by means of digital processing and analysis of the shadow and schlieren images obtained with the known time delay after initiation of the plasma sheet. The positions of the quasi-flat front of the shock wave envelope from each plasma sheet were averaged over the imaged field. Black points in Fig. 2 show experimental positions of the quasi-flat front of the shock wave envelopes from surface discharges initiated on the opposite walls of the working unit. The positions of plasma sheets at $t = 0$ corresponds to the coordinates $y = \pm 1.2$ cm. The waves start moving away from electrodes at a velocity of ~800 m/s; 15–20 μs after the discharge, the wave velocity is $V \approx 450$ m/s. Then, the counterpropagating shock waves originating from two plasma sheets exhibit interaction and decay within the following period of 10–20 μs. A systematic delay in the positions of waves coming from the upper and lower plasma sheets (for an equal wave velocity) is probably explained by asymmetry of the sliding discharge development in the direction along the probing beam and in the opposite direction. In Fig. 2, the time is normalized to the parameter $L/U = L\sqrt{(\rho/p)}$, where $L = 10^{-2}$ m, $\rho = 0.17$ kg/m^3, and $p = 1.32 \times 10^4$ Pa.

Numerical simulation of the flow during pulsed surface energy deposition. We have simulated a two-dimensional pattern of flow rising upon the pulsed surface energy deposition. The numerical calculations were performed using the Godunov generalized difference scheme with a piecewise-linear representation of the fields of gasdynamic functions. The mathematical model represented a system of Euler's equations (viscosity and heat conductivity were ignored). The energy introduction was modeled in accordance with a real pattern of the process. The gasdynamic pattern of perturbations moving from a 1-mm-thick region of energy deposition was calculated and compared to the experimental data on perturbations generated by plasma sheets at various levels of the deposited energy.

Figure 2 shows the results of calculations of the pressure dynamics during the motion of perturbations from the discharge region under the conditions of uniform energy deposition over the surface. For the sake of comparison, the *y*–*t* diagram of pressure for the counterpropagating shock waves is matched with the corresponding experimental positions of the shock waves. The calculations were performed assuming that about 50% of the energy deposited in the surface layer is converted into heat at the stage of energy supply. This assumption provided a good coincidence of the calculated and experimental data.

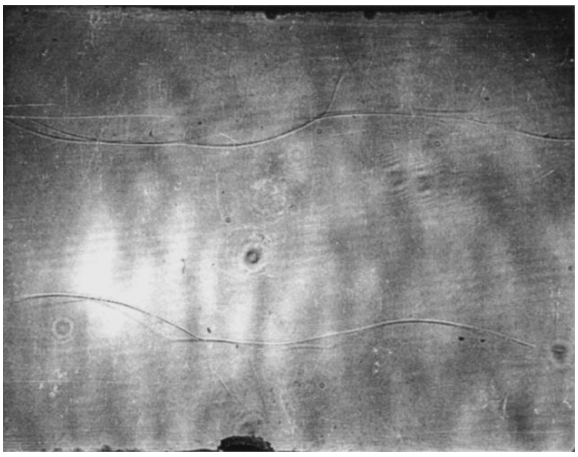

Fig. 1. A shadow image of the perturbed flow region 12 μs after initiation of the surface discharge (see the text for explanations).

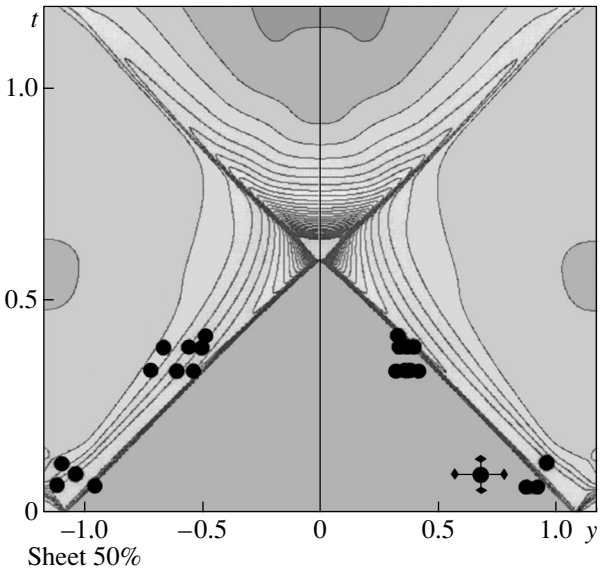

Fig. 2. The pattern of the pressure dynamics during the motion of perturbations from the discharge region (calculated assuming a 50% conversion of the deposited energy) in comparison to the experimental positions (black points) of the quasi-flat front of the shock wave envelopes from surface discharges initiated on the opposite walls of the working unit.

Thus, our analysis of the results of investigation of the flow development within the framework of a thermal energy deposition model allows the fraction of

energy immediately introduced into gas near the surface during initiation of a pulsed plasma sheet discharge to be estimated at 45–55%.

Acknowledgments. This study was supported by the Program of the Russian Academy of Sciences "Interaction of Plasma with High-Velocity Gas Flows."

REFERENCES

1. P. Kuz'min, I. M. Minaev, and A. A. Rukhadze, Teplofiz. Vys. Temp. **40**, 515 (2002).
2. I. A. Znamenskaya and A. E. Lutskiĭ, in *Proceedings of the 5th Symposium on Magnetic and Plasma Aerodynamics in Aerospace Applications, Moscow, 2003.*
3. N. V. Karlov, G. P. Kuz'min, and A. M. Prokhorov, Izv. Akad. Nauk SSSR, Ser. Fiz. **48**, 1430 (1984).
4. V. Yu. Baranov, V. M. Borisov, and O. B. Khristoforov, Kvantovaya Élektron. (Moscow) **8**, 165 (1981).
5. S. I. Andreev, I. A. Znamenskaya, I. O. Kovalev, *et al.*, in *Proceedings of the 3rd All-Russia Meeting "Physics and Gasdynamics of Shock Waves," Vladivostok, 1996* (Moscow, 1996), Part 2, pp. 68–73.

Translated by P. Pozdeev

Technical Physics Letters, Vol. 30, No. 12, 2004, pp. 1039–1041. Translated from Pis'ma v Zhurnal Tekhnicheskoĭ Fiziki, Vol. 30, No. 24, 2004, pp. 43–48.

Highly Efficient High-Power Quasi-Continuous Diode Laser Bars for Pumping Solid-State Lasers Based on Yb-Containing Active Media

N. I. Katsavets*, V. A. Buchenkov, D. M. Demidov, R. V. Leus, M. O. Iskandarov, A. A. Nikitichev, and A. L. Ter-Martirosyan**

"Semiconductor Devices" Joint-Stock Company, St. Petersburg, Russia
Institute of Laser Physics, St. Petersburg, Russia
*e-mail: * n_katsavets@mail.ru; ** ter@atc.rfntr.ru; mak@ilph.spb.su*
Received June 7, 2004

Abstract—Highly efficient high-power quasi-continuous diode laser bars (DLBs) emitting in the region of $\lambda = 0.95$ μm have been developed for pumping solid-state lasers based on Yb-containing active media. The parameters of DLBs and the results of long-term tests are presented. The proposed DLBs are implemented in a solid-state laser based on an Yb–Er glass operating in the 1.5 μm range. © *2004 MAIK "Nauka/Interperiodica".*

Diode-pumped solid-state lasers (DPSSLs) are widely used in various fields of science and technology. Of special interest are DPSSLs based on Yb -containing active media, because ytterbium ions, possessing an intense and broad absorption band in the spectral range of about 0.95 μm, are capable of effectively sensitizing the ions of other rare earth elements (Er, Ho, Tm). Owing to the large lifetime of the metastable laser level, such DPSSLs generate high-power optical pulses in a spectral range of 1.5–2.0 μm safe for the human eye [1].

In order to create the inverted population of levels in rare earth ions with large lifetimes (1–10 ms) of a metastable level, it is necessary to develop highly effective pumping sources. The role of such pumps is successfully performed by quasi-continuous diode laser bars (DLBs) with a laser pulse width of several milliseconds, which is about ten times the effective pumping pulse width in widely used neodymium-based DPSSLs [2].

However, the relatively large width of the optical pulse of DLBs creates increased cyclic thermal loading of the laser structure and poses additional requirements with respect to minimization of the mechanical stresses induced in laser chips in the course of DLB fabrication and assembly. This is related to the fact that excess mechanical stresses under the conditions of increased heating of the laser structure significantly reduce the lifetime of DLBs [3, 4].

This Letter reports on the development of highly efficient high-power DLBs with an optical pulse width of up to 5 ms, emitting in the 940–960 nm spectral range and intended for the optical pumping of ytterbium-based DPSSLs.

The diode laser chips were fabricated from low-threshold $In_{0.1}Ga_{0.9}As/AlGaAs$ heterostructures grown by molecular beam epitaxy (MBE) in a domestic system of the EP1203 type. The heterostructure design, and special features of the growth setup and the growth technology were described previously [5]. Each chip comprised an array of 50 optically decoupled diode lasers [6] with a period of 200 μm and a 160-μm-wide emitting region. The total resonator length was 1000 ± 50 μm. The front and back faces of the resonator were covered by reflection and antireflection coatings with a reflection coefficient of 95 and 5%, respectively.

The diode lasers were assembled into DLBs using a special setup ensuring positioning of the chips with an accuracy of ±1 μm. The chips were soldered with *p*-side to a copper heat sink by means of an indium-containing solder. The solder layer thickness was optimized so as to reduce the level of residual mechanical stresses.

The DLB output optical power was measured using a LaserMate (Coherent Co.) calibrated bolometric power meter. The optical output power (P_{out}) in the pulse was calculated as $P_{out} = P_{av}\nu$, where P_{av} is the power time-averaged by the bolometer and ν is the duty factor of the laser pulse sequence. Oscillograms of the laser output pulses were recorded using a reverse-biased silicon photodiode equipped with a special attenuating filter based on doped GaP. The spectral measurements were performed using an automated complex setup based on an MDR-23 grating monochromator.

Figure 1 shows the typical plots of the optical output power P_{out} and the total efficiency (defined as the ratio of the output power at the front mirror to the total consumed electric power) versus the pumping current for DLBs operating at different heat sink temperatures. An

1063-7850/04/3012-1039$26.00 © 2004 MAIK "Nauka/Interperiodica"

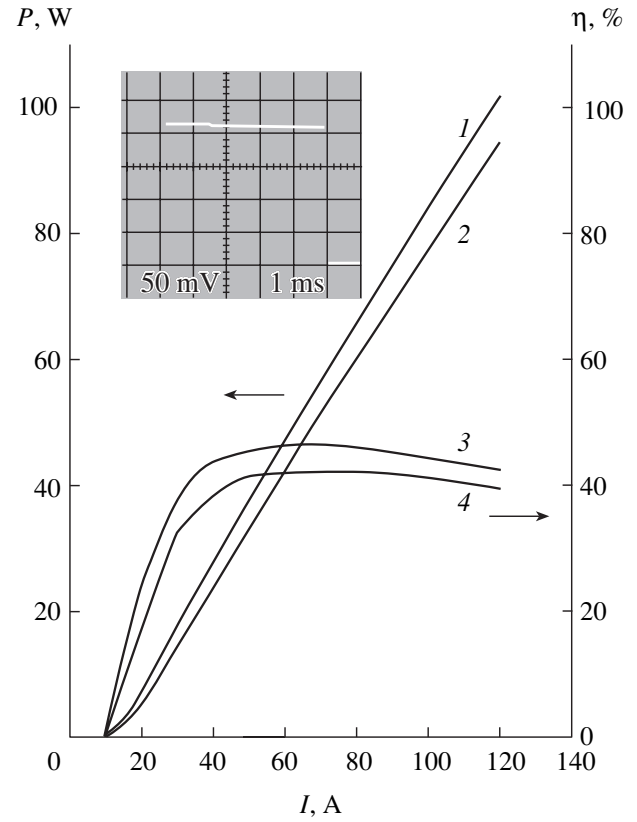

Fig. 1. Typical plots of the (*1*, *2*) optical output power *P* and (*3*, *4*) total efficiency η versus pumping current *I* for DLBs operating at a heat sink temperature of 25°C (*1*, *3*) and 55°C (*2*, *4*). Laser pulse width, 5 ms; repetition rate, 10 Hz. The inset shows an oscillogram of the laser output pulse.

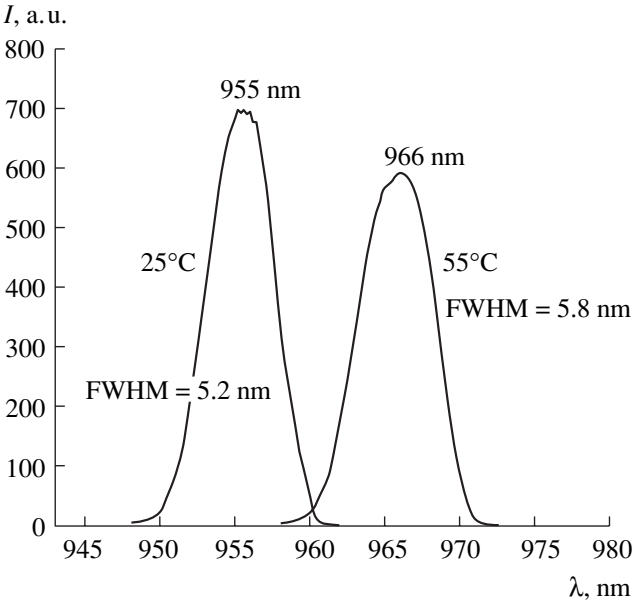

Fig. 2. The typical emission spectra of DLBs operating at different heat sink temperatures. Pumping current, 120 A; laser pulse width, 5 ms; repetition rate, 10 Hz.

analysis of these data shows that the maximum DLB efficiency is 47 and 42%, and the differential quantum efficiency is 72 and 66% for a heat sink temperature of 25 and 55°C, respectively. The critical temperature T_0 determined from the dependence of the threshold current on the heat sink temperature is 180°C.

The inset in Fig. 1 shows a typical oscillogram of the output optical pulse measured at a pumping current of 120 A. As can be seen, decay in the optical output power during the pulse does not exceed 5%. A comparison of the P_{out} values obtained for the two heat sink temperatures shows that additional heating of the DLB active region during the pumping pulse does not exceed 20°C (this estimate is obtained assuming a linear relation between P_{out} and the temperature).

Figure 2 shows the typical DLB emission spectra measured at different heat sink temperatures. Small width (FWHM, ~5 nm) of the emission band is evidence of high homogeneity of the DL chips and good quality of DLB assembly. The combination of the narrow DLB emission spectrum with a relatively broad absorption spectrum of ytterbium ions ensures effective pumping of DLBs in a wide range of working temperatures.

The proposed DLBs were subjected to long-term tests in the regime of stabilized constant pumping current (I = 100 A) and a constant pulse width (FWHM, 5 ms). The samples tested at a heat sink temperature of T = 25°C showed no evidence of any decrease in P_{out} over a series of 3×10^7 pulses. When the working temperature was increased to 55°C, the DBL power degradation was 1–2% over 10^7 pulses. Thus, using a linear extrapolation of $P_{out}(t)$ to $P_{out}(t_0) = 0.8P_{out}(0)$, the expected lifetime of DLBs at T = 55°C can be estimated as corresponding to $t_0 = 10^8$ pulses. On the other hand, assuming that an increase in the working temperature by 30°C leads to a tenfold increase in the rate of degradation (as is usually suggested in accelerated testing methods [7]), the results of the high-temperature test indicate that the expected lifetime of DLBs at T = 25°C corresponds to $t_0 = 10^9$ pulses.

The DLBs developed in this study were implemented in a solid-state laser based on an Yb–Er glass. The laser with two DLBs operated in the 1.5 μm range and generated 20-ns pulses with a pulse energy of up to 10 mJ at a repetition rate of up to 10 Hz. The laser output energy in the free lasing regime was 60 mJ at a differential efficiency of 18%.

In conclusion, we have developed, characterized, and tested highly efficient high-power DLBs with an optical pulse width (FWHM) of not less than 5 ms, intended for pumping solid-state lasers based on Yb-containing active media.

Acknowledgments. The authors are grateful to É.G. Sokolov and T.A. Sashnikova for their help in postgrowth operations.

REFERENCES

1. V. A. Buchenkov and A. A. Nikitichev, Lazer-Inform., No. 13–14, 268 (2003).
2. G. M. Zverev and Yu. D. Gulyaev, *Crystal Lasers and Their Applications* (Radio i Svyaz', Moscow, 1994) [in Russian].
3. E. Martin, J. P. Landesman, J. P. Hirtz, *et al.*, Appl. Phys. Lett. **75**, 2521 (1999).
4. M. Voss, C. Lier, U. Menzel, *et al.*, J. Appl. Phys. **79**, 1170 (1996).
5. S. V. Aleksandrov, A. N. Alekseev, D. M. Demidov, *et al.*, Pis'ma Zh. Tekh. Fiz. **28** (16), 71 (2002) [Tech. Phys. Lett. **28**, 696 (2002)].
6. D. M. Demidov, A. N. Ivkin, N. I. Katsavets, *et al.*, Pis'ma Zh. Tekh. Fiz. **27** (2), 36 (2001) [Tech. Phys. Lett. **27**, 58 (2001)].
7. N. C. Casey, Jr. and M. B. Panish, *Heterostructure Lasers* (Academic, New York, 1978).

Translated by P. Pozdeev

Technical Physics Letters, Vol. 30, No. 12, 2004, pp. 1042–1044. Translated from Pis'ma v Zhurnal Tekhnicheskoĭ Fiziki, Vol. 30, No. 24, 2004, pp. 49–55.

Spectroscopic Diagnostics of the Laser Erosion Plasma of Lead

A. K. Shuaibov, M. P. Chuchman, and L. L. Shimon

Uzhgorod National University, Uzhgorod, Ukraine

e-mail: ishev@univ.uzhgorod.ua

Received June 24, 2004

Abstract—Time-averaged emission spectra of a laser erosion plasma formed during the action of a neodymium laser [$W = (3–5) \times 10^8$ W/cm^2, $\lambda_g = 1.06$ μm, $\tau = 20$ ns, $f = 12$ Hz] on a lead target were measured for laser torch regions spaced by $r = 1$ and 7 mm from the target. The spatial dynamics of population of the excited states and the electron temperature in the laser torch are analyzed. © *2004 MAIK "Nauka/Interperiodica".*

Emission spectroscopy is widely used for plasma diagnostics and for the optimization of laser deposition processes. This method provides information about the temperature and density of electrons in the erosion plasma torch, the velocity of the plasma front propagation, the dynamics of physical processes in laser plasmas, the energy balance, and the composition of radiating particles in the plasma [1, 2].

In order to characterize the laser erosion plasma of lead—the metal widely used in microelectronics in the form of multicomponent compounds—we have performed optical diagnostics of the plasma torch formed at a laser-eroded lead target.

The laser plasma was generated by the beam of a pulsed-periodic neodymium laser [$W = (3–5) \times 10^8$ W/cm^2, $\lambda_g = 1.06$ μm, $\tau = 20$ ns, $f = 12$ Hz] focused on the surface of a target made of a special-purity lead. The target was placed into a vacuum chamber evacuated to a residual pressure not exceeding 5–10 Pa. The primary laser radiation beam was focused on the target, and the secondary optical emission from the laser plasma was collected with the aid of lenses with focal distances of 50 and 11 cm, respectively. The intensity of emission from the laser plasma was measured in the spectral range from 200 to 600 nm. The signal intensity was corrected for the relative spectral sensitivity k_λ of the detection system comprising an MDR-2 monochromator, a FEU-106 photomultiplier, and a KSP-4 recorder-amplifier. The emission intensity was measured with an error not exceeding 10%. The spectra were interpreted and the plasma parameters were determined using the data from [3–6].

Based on the optical characteristics obtained, we determined the distribution of populations N_j of the energy states using a formula indicative of inhomogeneity of the electron temperature:

$$\frac{N_j}{g_j} = \sum_k \frac{\lambda_{jk} I_{jk}}{A_{jk} g_j}, \quad (1)$$

where λ is the radiation wavelength, A is the transition probability, I is the intensity, and g is the statistical weight. The population of the upper jth level was determined taking into account all radiative decay channels.

The electron temperature T_e was calculated using the linearized energy distribution of the populations of excited states, which was analyzed by solving an overdetermined system of equations describing all experimental points (j):

$$\ln\left(\frac{N_j}{g_j}\right) = \ln\left(\frac{N_0}{g_0}\right) + \frac{E_j}{kT_e}, \quad (2)$$

where E_j is the energy of the jth level, k is the Boltzmann constant, and index 0 refers to the ground state. As a result, we obtained a line corresponding to the minimum sum of deviations from the given points and occurring within the given confidence interval of populations. When necessary, the distribution was divided into groups of points corresponding to preset conditions. The experimental method and procedure were described in detail elsewhere [7, 8].

Investigation of the time-averaged spectra of emission from the laser plasma showed that the spectral intensity distribution significantly changes depending on the conditions of irradiation of the target. This result stimulated us to tabulate the percentage contributions of the emission intensities of particular spectral lines to the total intensity of the linear emission spectrum of the laser erosion plasma torch. The total intensity exhibited no significant variations and could be strongly distorted only upon multiply repeated laser actions at the same point of the target.

1063-7850/04/3012-1042$26.00 © 2004 MAIK "Nauka/Interperiodica"

An analysis of data in the table shows that the most intense emission from the laser erosion plasma of pure lead corresponds to electron transitions from the lower states of ions and atoms and from the levels close to the bottleneck of the recombination flux of the atomic component of plasma. The bottleneck of the recombination flux for lead atoms is situated at $E_1 = 6.5$ eV, while the ionization energy is $E_i = 7.417$ eV. For lead ions, the bottleneck of the recombination flux is at $E_1 = 21.55$ eV, while the energy of ionization of a singly charged ion amounts to 22.45 eV.

When the distance from the target was increased, no change in the bottleneck position was observed, whereas the energies of atomic levels corresponding to the maximum emission exhibited a decrease. Indeed, at $r = 1$ mm, the intensity of the spectral lines with $\lambda =$ 261.4, 280.2, 405.7 nm ($E_{up} = 5.71$, 5.74, 4.37 eV) accounted for 31.7% of the total intensity, while at $r =$ 7 mm, the intensity of the spectral lines with $\lambda = 364$, 368.3, 405.7 nm ($E_{up} = 4.37$, 4.34, 4.37 eV) amounted to 45.3% of the total intensity. The emission from ions with the spectral line wavelengths 220.4 and 560.9 nm ($E_{up} = 14.79$ eV and 17 eV) at $r = 1$ and 7 mm accounted for 12.3 and 8.7%, respectively.

The percentage contribution of the intensity of emission from PbII ions for the transitions from levels close to the bottleneck of the recombination flux increases with the distance from the target to the zone of radiation takeoff from the plasma. However, this contribution is still on a level of 1%, which indicates that the plasma contains a negligibly small proportion of doubly charged lead ions (in comparison to the numbers of atoms and singly charged ions), the more so that the double charged ions much more readily recombine [7]. Therefore, a specific feature of the laser erosion plasma of lead is the formation of singly charged ions in highly excited states.

In order to study the time-integrated spatial dynamics of processes in the laser erosion plasma, we constructed the energy distributions of populations of the excited states (see figure, where we also plotted the populations of excited states formed upon repeated irradiation of the target: the spectra were sequentially recorded at t_1 and t_2). Clear separation of the experimental points in this plot is provided by different values of the photomultiplier voltage (U_{PM}) for the spectra measured over various time intervals.

Upon expansion of the laser erosion plasma, the scattered points more clearly fit to the lines constructed using the maximum likelihood method. These straight lines are indicative of inhomogeneity of the electron temperature, inversion of the population for PbII ions, and considerable population of the upper excited states of PbI atoms. In the case of repeated irradiation of the target surface, the electron temperature exhibits a more pronounced decrease at smaller distances from the target. The difference between the electron temperatures in the torch formed by laser erosion of a fresh target surface and that formed upon multiply repeated irradiation for $r = 7$ mm amounts to about 10% of the difference observed for $r = 1$ mm. Therefore, evolution of the laser erosion plasma at large distances from the target proceeds rather independently of the initial conditions. As the plasma expands, the population and its inversion for the excited states of PbII (see figure) exhibit a significant decrease, whereas the population of the upper excited states of lead increases. A straight line drawn for the upper excited states of atoms shows that the degree of inversion increases with distance from the

Percentage contributions of the main spectral components to the total intensity of linear spectrum of the laser erosion plasma of lead

λ, nm	Atom, ion	Upper level	E, eV	$\Delta I/k_\lambda$, % $r = 1$ mm	$\Delta I/k_\lambda$, % $r = 7$ mm
220.4	Pb II	$7s^2S_{1/2}$	14.79	9.3	4.7
224.7	Pb I	$p7d^3D_2$	6.48	1.7	1.6
239.4	Pb I	$p7d^3F_3$	6.5	1.5	1.6
244.4	Pb I	$p8s^3P_0$	6.04	1.2	0.8
244.6	Pb I	$p8s^3P_1$	6.036	1.4	0.5
247.6	Pb I	$p7s^3P_2$	5.97	1.5	0.6
257.7	Pb I	$p7s^1P_1$	6.13	3.0	1.2
261.4	Pb I	$p6d^3D_2$	5.71	9.7	5.6
266.3	Pb I	$p7s^3P_2$	5.97	4.7	1.5
280.2	Pb I	$p6d^3F_3$	5.74	12.4	7.4
283.3	Pb I	$p7s^3P_1$	4.37	6.5	3.1
287.3	Pb I	$p6d^3F_2$	5.63	5.0	3.8
326.1	Pb II	$10s^2S_{1/2}$	21.29	1.6	0.3
357.3	Pb I	$p7s^1P_1$	6.13	4.2	5.8
364	Pb I	$p7s^3P_1$	4.37	4.8	9.6
368.3	Pb I	$p7s^3P_0$	4.34	5.1	14.5
374	Pb I	$p7s^3P_2$	5.97	3.7	1.7
401.9	Pb I	$p6d^3F_3$	5.74	1.0	0.4
405.7	Pb I	$p7s^3P_1$	4.37	9.6	21.2
427.5	Pb II	–	18.89	2.2	1.53
438.7	Pb II	–	18.89	1.6	1.0
478.8	Pb II	–	–	0.2	0.5
500.5	Pb I	$p7s^1P_1$	6.13	0.3	0.6
520.1	Pb I	$p8s^3P_1$	6.04	0.8	2.3
530.7	Pb II	–	21.55	0.5	0.6
536.7	Pb II	–	18.88	0.9	0.4
560.9	Pb II	–	17	3.0	4.0
571.4	Pb II	–	21.39	0.6	1.2
576.8	Pb II	–	21.34	0.9	1.7
298.7	Pb II	–	20.79	1.2	0.2

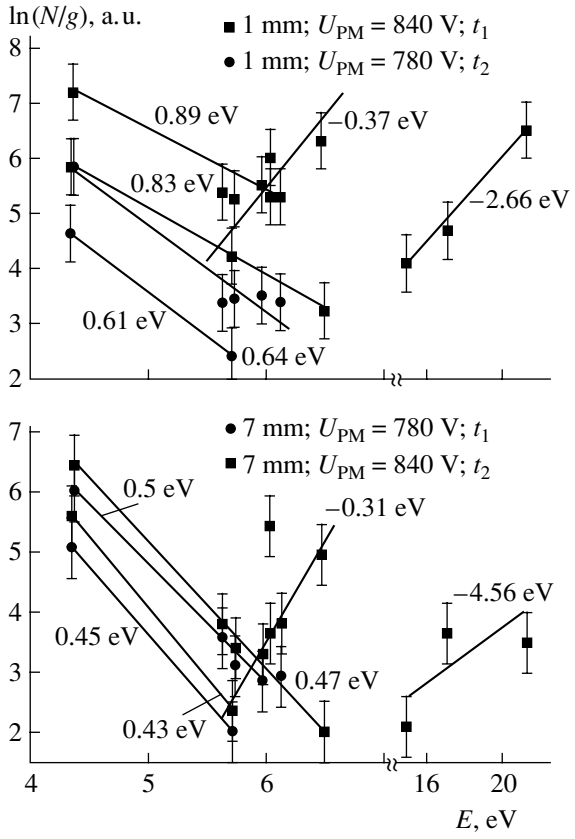

The energy distributions of the time-averaged populations of the excited states formed during laser erosion of a lead target and their variation with time (t_1, t_2) at different distances from the target (r = 1 and 7 mm). Figures at the lines indicate the electron temperature.

target. This is indicative of the effective recombination of ions in the laser erosion plasma. In the course of expansion, a peak in the formation of excited states shifts toward lower energies for both atoms and ions.

As can be also seen from the figure, inhomogeneity of the conditions of laser erosion leads to variations in the relative emission intensity within 20–30% for r = 1 mm and below 10% for r = 7 mm.

As the distance from the target increases from 1 to 7 mm, the electron temperature decreases from ~0.86 to ~0.48 eV. The T_e value is well correlated with the position of the bottleneck in the recombination flux of atomic and ion components of the laser erosion plasma:

$$E_i - E = 3/2kT_e. \quad (3)$$

The existence of several directions of lines in the figure is indicative of a variety of mechanisms involved in the formation of excited states in atoms and ions. Judging from the distribution of populations, the operative mechanisms of the formation of such excited states are characterized by considerable selectivity. We believe that such a form of the distribution is probably caused by addition of the recombination component (involving differently charged ions) to the thermal component. This is favored by specific features of the laser erosion process and by the spatiotemporal inhomogeneity of the plasma composition and structure [7].

Thus, during the laser deposition of compounds containing lead, an important role is played by ion reactions and the related features of energy balance in the laser plasma. The influence of the nonstationary character of the laser erosion plasma (related to variation of the conditions of laser ablation) on the results of investigations and in practical applications can be decreased by using an emission takeoff region more distant from the target surface. The composition of plasma is determined predominantly by lead atoms and singly charged ions.

The electron temperature decreases from ~0.86 to ~0.48 eV when the distance from the target increases from 1 to 7 mm. The position of the recombination flux bottleneck for the atomic and ion components of laser plasma corresponds to the energy levels at 6.5 and 21.55 eV, respectively. Evolution of the laser plasma at large distances from the target is rather independent of the initial conditions. The operative mechanisms of formation of the excited states in atoms and ions are characterized by considerable selectivity.

The most intense emission lines in the spectrum of the laser erosion plasma measured for r = 1–7 mm (with percentage contributions to the total spectrum exceeding 4%) are as follows (nm): 220.4 (PbII), 261.4 (PbI), 280.2 (PbI), 357.3 (PbI), 364 (PbI), 368.3 (PbI), 405.7 (PbI). We recommend using these lines for optical diagnostics of the erosion plasma during laser deposition of lead-based multicomponent compounds.

REFERENCES

1. S. S. Chu and C. P. Grigoropoulos, J. Heat Transfer **122**, 771 (2000).
2. D. B. Geohegan and A. A. Puretzky, Appl. Phys. Lett. **67**, 197 (1995).
3. Ch. Corliss and W. Bozman, *Experimental Transition Probabilities for Spectral Lines of Seventy Elements (NBS Monograph No. 53)* (US Government Printing Office, Washington, 1962).
4. N. Grevesse, Sol. Phys. **6**, 381 (1969).
5. N. P. Penkin and I. Yu. Slavena, Opt. Spektrosk. **15**, 83 (1963).
6. J. Migdalek, J. Quant. Spectrosc. Radiat. Transf. **16**, 265 (1976).
7. A. K. Shuaibov, M. P. Chuchman, and L. L. Shimon, Zh. Tekh. Fiz. **74** (2), 133 (2004) [Tech. Phys. **49**, 272 (2004)].
8. O. K. Shuaibov, M. P. Chuchman, L. L. Shimon, and I. E. Kacher, Ukr. Fiz. Zh. (Russ. Ed.) **48**, 223 (2003).

Translated by P. Pozdeev

Technical Physics Letters, Vol. 30, No. 12, 2004, pp. 1045–1047. Translated from Pis'ma v Zhurnal Tekhnicheskoĭ Fiziki, Vol. 30, No. 24, 2004, pp. 56–62.

Using Tunable Lasers for Photochromic Coherent Speckle Diagnostics of Bulk Scattering Media and Optical Fibers

G. G. Akchurin and A. G. Akchurin

Saratov State University, Saratov, Russia

e-mail: rector@sgu.ssu.runnet.ru

Received June 22, 2004

Abstract—We have observed for the first time the dynamics of a speckle field generated in bulk scattering partly ordered media or low-mode optical fibers probed by a laser diode (λ = 654 nm) and a compact diode-pumped YAG:Nd laser (λ = 532 μm) in the regime of frequency tuning. The dynamic coherent speckle-photochromic effect can be observed provided that the deviation of the probing radiation frequency is comparable with or greater than the effective phase delay difference between modes in the optical fiber or between waves in the random scattering medium. Using the proposed photochromic speckle technique, it is possible to determine the intermode dispersion of fibers with a length on the order of one meter and the dispersion of phase delay in test fluoroplastic structures in the regimes of severalfold scattering (for a sample thickness of 10–20 μm) or multiple scattering (for a thickness of up to ~2 cm). © *2004 MAIK "Nauka/Interperiodica".*

In recent years, considerable effort has been devoted to the development of contactless optical methods for the diagnostics of inhomogeneous random or structurized bulk media (including biological tissues), which is related to the development of coherent optical tomography [1, 2]. The most significant progress in experimental realization of the optical tomography scheme was achieved with low-coherency optical tomographs based on a single-mode fiber-optic Michelson interferometer conjugated with a superluminescent semiconductor diode, which ensure a spatial resolution of 10–20 μm at a limiting probing depth of 1–1.5 mm.

Recently, it was suggested that effective diagnostics of inhomogeneous scattering biological tissues to a depth of several centimeters can be provided by so-called diffusion tomographs based on nonstationary optical techniques [3]. One possible approach to such tomographs consists in probing strongly scattering bulk media by picosecond laser pulses in the time domain. However, the most promising experimental realization seems to be provided by the diffusion optical tomographs operating in the frequency domain. These tomographs employ an amplitude-phase technique, whereby the object is probed by amplitude-modulated radiation of a laser diode operating in a range of frequencies comparable with the inverse time of the laser pulse broadening [4]. As is known, the propagation of laser radiation through a bulk scattering medium accompanied by the appearance of a certain speckle structure of scattered radiation as a result of the coherent interference effects. Using speckle correlation techniques based on the analysis of statistical properties of two-dimensional distributions of the coherent scattering field with allowance for their polarization properties, it is possible to obtain information about the structure of bulk scattering media [5].

This paper presents the result of application of a coherent-dynamical method, proposed for determining the dispersion of multimode optical fibers and the scattering parameters, to laser probing of stationary, random or partly ordered optically inhomogeneous bulk media. The method is based on an analysis of the dynamics of speckles generated as a result of deviation of the probing radiation frequency.

Transverse speckle dynamics in low-mode optical fibers probed by radiation of a tunable laser and the possibility of determining intermode dispersion. Previously we observed for the first time a coherent-dynamic effect related to the variation of the spatial structure of a speckle field of radiation passing through a multimode fiber with a length on the order of one hundred meters, in response to tuning the frequency of a He–Ne laser [6]. In the case of a low-mode (D = 9 μm, NA = 0.17) fiber probed by radiation of a single-frequency He–Ne laser (λ = 633 nm), observation of the speckle dynamics would require an optical fiber length of several kilometers in order to provide that the range of frequency tuning be comparable with intermode dispersion. It would of interest to realize the regime of spatial speckle dynamics for a short fiber. For this purpose, we have used the possibility of frequency tuning with a range of several gigahertz, which is provided by variation of the injection current in quantum-confinement laser diodes or by temperature variation in a diode-pumped solid-state YAG:Nd laser chips with an intracavity second-harmonic generator.

1063-7850/04/3012-1045$26.00 © 2004 MAIK "Nauka/Interperiodica"

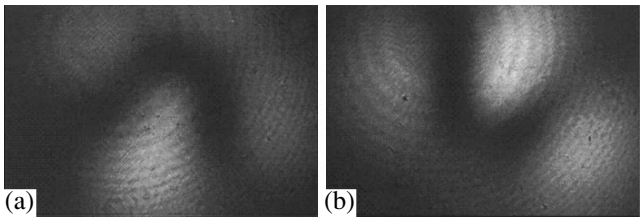

Fig. 1. The typical dynamics of a spatial structure of waveguide modes in the output radiation of a 1-m-long low-mode (D = 9 μm, NA = 0.17) step-index optical fiber robed with radiation of a quantum-confinement single-frequency laser diode with a frequency detuning of 126 GHz between patterns (a) and (b) (2D correlation coefficient, 0.018).

Figure 1 shows typical patterns of the transverse distribution of speckle fields for the laser radiation past a low-mode optical fiber with a fixed length, observed for two values of the resonator frequency. The results of a thorough experimental investigation of the mode photochromic effect showed that the transverse displacement of the speckle pattern is proportional to the fiber length and the range of laser frequency tuning.

The main mechanism of the photochromic effect observed in optical fibers can be interpreted based on the wave analysis of propagation of a single-frequency laser radiation in step-index multimode fibers, performed in the representation of linearly polarized LP_{nm} modes [7]. When the laser frequency is tuned, a change in the phase of each LP_{nm} mode propagating in the fiber can be determined (provided that the modes are far from cutoff, $u_{mn} \ll V = (2\pi a/\lambda)(n_{co}^2 - n_{cl}^2)^{1/2}$) from the relation

$$\delta\Phi_{n,m} - \delta\Phi_{n',m'} = (u_{n,m} - u_{n',m'})/2n_{co}^2/(2\pi a/\lambda)L\Delta\lambda, \quad (1)$$

where u_{nm} are the transverse propagation constants for the core of a step-index fiber, n_{co} is the core index, a is the core radius, L is the fiber length, $\Delta\lambda$ is the range of variation of the probing laser wavelength.

The results of detailed experimental investigation of step-index optical fibers with various lengths and diameters showed that, using the dependence of the two-dimensional (2D) correlation coefficient of frequency-dependent speckle fields on the frequency shift, it is possible to determine the mode dispersion for multimode fibers. The experiments performed on the typical multimode optical fibers (with a core diameter of D = 50 μm, a numerical aperture of NA = 0.2, and lengths varied from 100 m to tens of centimeters) and on the low-mode fibers (D = 9 μm, NA = 0.17, and the lengths varied from 5 km to several meters) showed that the transverse rearrangement of the speckle field of the output radiation pattern characterized by the 2D correlation coefficient is a linear function of the frequency detuning of the probing radiation. In particular, in our experiments, the maximum range of frequency tuning (660 MHz) for the probing radiation of a single-frequency He–Ne laser led to a twofold decrease in the 2D correlation coefficient for a 50-m-long multimode fiber, which corresponded to a dispersion of 30 MHz/km. This value agrees with the results of dispersion measurements using pulse and phase techniques. However, these traditional methods encounter considerable difficulties even in the case of multimode fibers with a length of several tens of meters, not speaking of low-mode fibers. The results of our experiments confirmed the possibility of determining the dispersion of multimode fibers with a length of not less than two meters using YAG:Nd laser with the frequency tuned within 84 GHz. By probing with a laser diode with frequency-tunable single-frequency quantum-confinement laser, it is possible to determine the dispersion for multimode fibers with a length of about 20 cm or low-mode fibers with a length of several meters.

Photochromic speckles in optically inhomogeneous random or ordered bulk media probed by tunable lasers. We have observed for the first time the transverse dynamics of the speckle field in optically inhomogeneous, stationary random or ordered (photonic crystals) bulk media probed by tunable lasers. The physical mechanism of the dynamic speckle photochromic effect observed in such scattering media is analogous to that described above for the multimode optical fibers possessing a significantly narrower discrete spatial spectrum. The investigation of speckle dynamics in laser-probed stationary random or partly ordered scattering structures are of special importance for optical topography, because the progress in this direction will probably provide the possibility to evaluate spatial inhomogeneity from an analysis of the photochromic speckle dynamics. Qualitative results of our experiments on fluoroplastic films with thicknesses below 100 μm probed simultaneously with a He–Ne red laser and a YAG:Nd green laser, with the beams spatially coinciding at the input and having comparable divergence, showed the presence of red, green, and yellow speckles in the far zone at the output from the samples. The yellow speckles arise at the sites of spatial overlap of the red and green speckles from two lasers in the paraxial region. The difference in the laser frequencies was very large (on the order of 98 THz ($\Delta\lambda \approx 101$ nm)). The experiments showed that the difference of phase delays for the probing of fluoroplastic phantoms with thicknesses below 20 μm in the scattered red and green laser radiation is also so large that the spatial positions of speckles coincide only for small-angle scattering (within a few angular degrees) near the axis of the probing beams (were virtually all the two-wave speckles overlap), while the phase delays at large scattering angles (reaching tens of femtoseconds) lead to spatial divergence of the red and green speckles. As the phantom thickness increases, the transverse correlation radius and, accordingly, the average speckle size quite rapidly decrease, while the phase delay would increase. If the difference between the probing frequencies is sig-

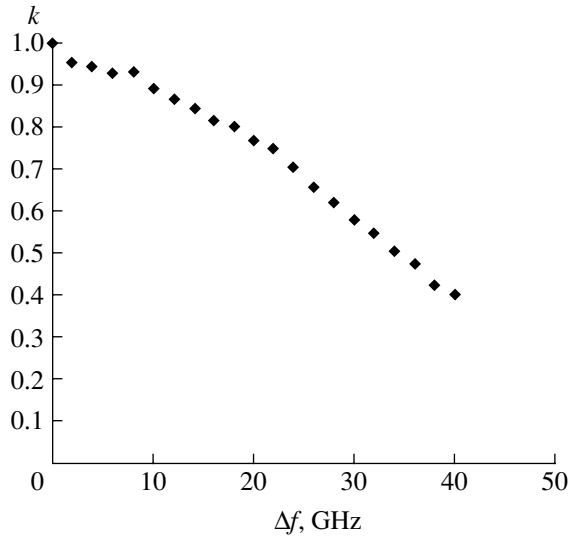

Fig. 2. A plot of the 2D correlation coefficient of the scattered speckle field versus frequency detuning for a 0.5-cm-thick test fluoroplastic plate probed by an injection-current-tuned laser diode.

nificantly smaller (~1 THz, not distinguished by the human eye), it is necessary to record two sequential speckle patterns. The difference pattern and the corresponding 2D correlation coefficient bear information about differential phase delays in the scattering medium. If the probing laser frequency is continuously tuned within a range much greater than the inverse difference of phase delays, a stochastic speckle dynamics is observed that appears as a "boiling" speckle pattern.

We have experimentally studied the dynamics of speckle structures observed upon probing fluoroplastic plates with a thickness varying from several tens of microns up to ~2 cm. The samples were probed by lasers with a maximum intermode frequency tuning. These were a semiconductor laser diode ($\Delta\nu$ = 126 GHz, $\delta\lambda$ = 0.18 nm) and a compact diode-pumped solid-state YAG:Nd laser ($\Delta\nu$ = 84 GHz, $\delta\lambda = 7.97 \times 10^{-2}$ nm) with an output power of 10^{-3} W. The typical results illustrating the dynamic of speckles obtained using current-tunable laser diodes for probing multiply-scattering fluoroplastic phantoms are presented in Fig. 2.

In conclusion, we have experimentally verified the speckle-photochromic method for determining the effective phase delay or structural dispersion (related to the multiplicity of scattering) in stationary, random or partly ordered optically inhomogeneous bulk media. The proposed method, based on probing the object by radiation of tunable lasers and detecting the corresponding 2D speckle patterns, has proved this approach to be competitive with the traditional nonstationary methods of laser diagnostics.

Acknowledgments. The authors are grateful to L.A. Mel'nikov and E.A. Romanova for fruitful discussions and to D.A. Zimnyakov for his help in conducting experiments.

This study was supported by the Presidential Program of Support for Leading Scientific Schools in Russia (project no. NSh-25.2003.2) and the US Civilian Research and Development Foundation for the Independent States of the Former Soviet Union (CRDF grant no. REC-006).

REFERENCES

1. A. F. Fercher, J. Biomed. Opt. **1**, 157 (1996).
2. V. M. Gelikonov, G. V. Gelikonov, N. D. Gladkova, *et al.*, Pis'ma Zh. Éksp. Teor. Fiz. **61**, 149 (1995) [JETP Lett. **61**, 158 (1995)].
3. *Handbook of Optical Biomedical Diagnostics*, Ed. by V. V. Tuchin (SPIE Press, Bellingham, 2001), p. 1057.
4. G. G. Akchurin, D. A. Zimnyakov, and V. V. Tuchin, Biomed. Radioélektron., No. 1, 46 (2000).
5. D. A. Zimnyakov *et al.*, Appl. Nonlinear Dyn. **10**, 188 (2002).
6. G. G. Akchurin, L. A. Melnikov, and E. A. Romanova, Proc. SPIE **2693**, 741 (1996).
7. A. W. Snyder and J. D. Love, *Optical Waveguide Theory* (Chapman and Hall, London, 1983).

Translated by P. Pozdeev

Technical Physics Letters, Vol. 30, No. 12, 2004, pp. 1048–1050. Translated from Pis'ma v Zhurnal Tekhnicheskoĭ Fiziki, Vol. 30, No. 24, 2004, pp. 63–69.

High-Resolution Conductivity Profile Measurements in Detonating Pressed Explosive

A. P. Ershov*, N. P. Satonkina, and G. M. Ivanov

Lavrentiev Institute of Hydrodynamics, Siberian Division, Russian Academy of Sciences, Novosibirsk, Russia

**e-mail: ers@hydro.nsc.ru*

Received July 1, 2004

Abstract—An improved method for measuring the electric conductivity profile behind the detonation front in dense high explosives has been developed, which provides for a spatial resolution better than 0.1 mm. In comparison to the existing techniques, the proposed method ensures a more than tenfold increase in the range of conductivity measurements. The conductivity profile of detonating RDX exhibits a peak with an amplitude of $\approx 2\ \Omega^{-1}\ \mathrm{cm}^{-1}$ and a width of about 1 mm, in agreement with known data on the chemical reaction zone thickness. The peak is followed by a "tail," in which the conductivity is several times lower. In samples with a density of 1.75–1.8 $\mathrm{g/cm}^3$ (approaching the theoretical compaction limit), the conductivity peak exhibits a sharp increase in amplitude (up to 5–6 $\Omega^{-1}\ \mathrm{cm}^{-1}$), while the peak width decreases to 0.5 mm. © *2004 MAIK "Nauka/Interperiodica".*

Introduction. The kinetics of chemical reactions involved in the phenomenon of detonation of high explosives (HEs) has been extensively studied in recent decades. Experimental methods developed so far provide for the most part qualitative information about the reaction zone thickness and the profiles of parameters in this zone. The results obtained by various methods are frequently contradictory. This situation is by no means surprising, since the problem of characterization of the reaction zone is among the most difficult in the physics of explosion. Indeed, an extremely high reaction rate (and, accordingly, very small reaction zone thickness) implies high requirements with respect to spatial resolution of the experimental techniques. However, extremal parameters of the detonation process and the aggressive character of the explosion hinder the use of small-size sensors. Optical probing methods are apparently free of the above disadvantages, but interaction of the detonation wave with the window material may affect the process and distort the results. Therefore, the development of alternative approaches is still an important task.

This paper describes a method based on the high-resolution measurement of the electric conductivity profile in the detonation wave. Previous investigations [1–3] showed that the conductivity may vary in a much broader range than the mechanical parameters such as the mass flow velocity or the pressure (the maximum pressure at the wave front is typically about 30% higher than the Chapman–Jouguet pressure). Therefore, methods based on the conductivity measurements are potentially more sensitive. In addition, variations of the conductivity may provide information about the process chemistry not reflected by the mechanical variables. However, this possible advantage may as well bring some uncertainty related to the exaggerated effect of by-products that are not as significant from the standpoint of energy balance. It is also not excluded that the conductivity obeys a quasi-equilibrium mechanism [4], whereby the ionization is determined primarily by the thermodynamic conditions; nevertheless, the reaction zone may still be well pronounced on the conductivity profile. Only experimental results will show to what extent the conductivity diagnostics is a useful and reliable tool for investigation of the reaction zone. Most of the previous experiments reported so far suffered from insufficient spatial resolution and, hence, provided rather a qualitative information. A quite acceptable resolution was achieved in our previous study [3], but only within a rather low conductivity range (fractions of $\Omega^{-1}\ \mathrm{cm}^{-1}$, typical of many loose-packed explosives). The role of such an important parameter as the initial density remained unknown.

This study was performed using a modified variant of the differential technique [3] capable of providing a sufficiently high spatial resolution and applicable to high-density HEs.

Experimental. The experiments were performed in a coaxial cell, schematically depicted in Fig. 1a. An explosive charge with a diameter of $b = 8$ mm was pressed into a thick copper case-electrode (*1*, *2*). Axial copper electrode *3* with a diameter of $c = 2$ mm was mounted in a PMMA stopper *4* fixed by hollow screw *5*. The outer electrode had a cavity in which the conductivity gauge *7* was arranged. The gauge had the form of a toroidal coil with a coefficient of mutual inductance

$M \sim 15$ nH with respect to the compartment contour. Parts *1* and *2* of the outer electrode had a thread connection, with a gap width between the cavity and the coaxial channel being determined by insulating spacer *6* (0.3-mm-thick Teflon film or 0.8-mm-thick PMMA plate). A sample of high explosive was pressed by 5-mm increments, so that the gap was near the middle of one of such portions. A total of two to four experiments (shots) were performed for each HE density.

As soon as the detonation zone reaches the axial electrode, the cell circuit is closed via a conduction zone behind the front and the current flows in the gauge compartment, producing a magnetic flux through the coil and inducing the electric response. When the detonation wave front passes by the gap section, the current is partly switched directly to the adjacent part of the outer electrode *2*. The current through the gauge compartment and the magnetic flux decrease, thus producing another pulse of the response voltage U. The electric conductivity, proportional to this signal, is given by the formula [3]

$$\sigma(x) = \frac{\ln(b/c)}{2\pi DM}\frac{U(t)}{V}, \qquad (1)$$

where D is the detonation front velocity, x is the distance traveled by the detonation front away from the gap for the time t, V is the supply voltage between electrodes (determined by the constant current I through the shunt R_s and the conducting charge region connected in parallel). In fact, a voltage U_{in} somewhat smoothened due to the coil inductance $L \approx 1$ μH is observed, so that a corrected voltage for formula (1) is $U = U_{in} + (L/R)dU_{in}/dt$, where R is the input impedance (50 Ω) of the oscillograph.

The spatial resolution of the proposed technique is determined by the gap width, which is conveniently denoted as $2a$. According to our previous estimates [3], the resolution is not worse than a (i.e., half of the insulating spacer thickness). In this study, the estimate of resolution was refined. Ignoring the curvature of the outer electrode, the electric field distribution can be described by solving an electrostatic problem for a planar configuration. For a stepwise conductivity σ behind the detonation front, the current per unit width of electrode *2* is $J = \pi\sigma E(x + 2a)/(2K(m))$, where E is the electric field strength far from the gap, K is the complete elliptic integral of the first kind, and $m = \sqrt{1 - x^2/(x + 2a)^2}$. Figure 1b shows the calculated signal profile (curve *1*, the current derivative dJ/dt) in comparison to the ideal step function *2*. As can be seen, a more adequate estimate of the experimental resolution is provided by $a/2$ (i.e., by a quarter of the gap width): at this distance traveled by the front away from the gap, the error amounts to about 25% and rapidly falls off as the distance increases further. The analytical estimates were confirmed by the results of numerical calculations including the conductivity varying along the cell axis over a characteristic distance of $2.5a$.

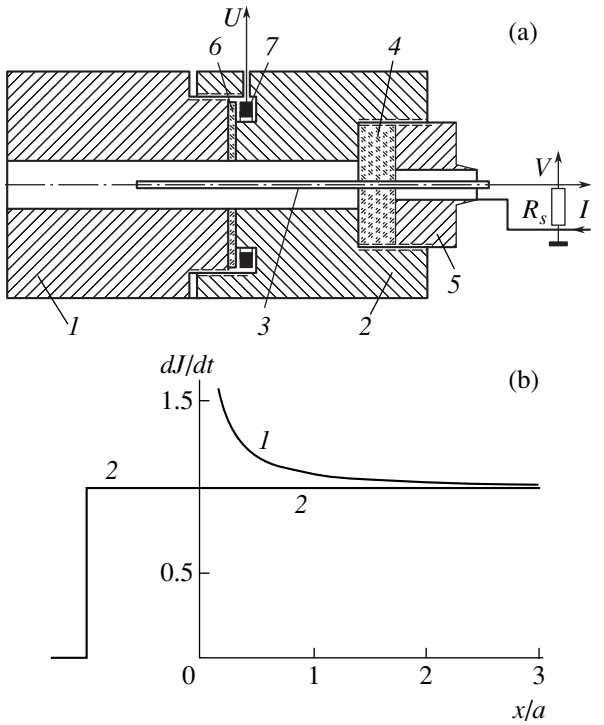

Fig. 1. Schematic diagrams showing (a) the experimental cell geometry and (b) the conductivity gauge response calculated for σ = 1, and $E = 1$ (curve *1*) in comparison to the unit step (curve *2*) beginning at the middle of the gap (see the text for explanations).

The differential scheme used previously [3] included an external measuring contour (a short piece of wire) with a parasitic inductance of about 50 nH. The main advantage of the new (perfectly coaxial) scheme is a very low inductance L_c of the gauge compartment contour (below 1 nH). This circumstance sharply increased the range of measurements, which has expanded up to about 10 Ω^{-1} cm^{-1} (instead of a fraction of Ω^{-1} cm^{-1} [3]). The limiting factor is the bypass current via a conducting medium over the gap, related to a parasitic voltage $L_c(dJ/dt)$. It should be noted that a similar low-inductance scheme was used in [5], but in a less convenient planar slab geometry.

Results and discussion. Figure 2a shows the typical experimental curves obtained with the aid of a 200-MHz-bandwidth digital oscillograph at a 4-ns sampling interval. The main coil response voltage U appears at a time of abut 1.8 μs. A signal of reverse polarity arising at $t = 0$ is induced by the start current when the detonation front reaches the axial electrode and closes the circuit. This first peak was used to calibrate the gauge (with respect the M value) immediately during the shot using the relation $(1/M)\int_0^t U\,dt = (V_0 - V)/R_s$. The detonation front velocity was determined

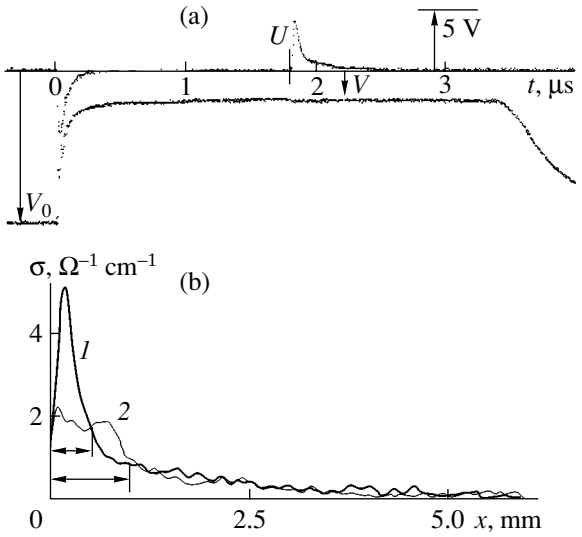

Fig. 2. (a) Experimental oscillograms measured for an initial RDX density of 1.75 g/cm^3 (signal V was measured with a 1 : 10 voltage divider; real voltage on the cell within t = 1.8–3 μs was about 25 V); (b) electric conductivity profiles for an initial RDX density of (*1*) 1.75 and (*2*) 1.64 g/cm^3.

using the reference points of the signals and known distances in the experimental system.

Figure 2b (curve *1*) shows the conductivity profile calculated using formula (1) for a high-density sample. At a gap width of 0.3 mm (Teflon spacer), the resolution was about 0.075 mm. The profile reveals a clear narrow peak with a width of about 0.5 mm. A similar profile was obtained for the maximum HE density (≈1.8 g/cm^3) achieved in our experiments. Curve *2* shows a profile for the HE sample of a lower density (≈1.64 g/cm^3). Note a sharp difference from the former case: the peak amplitude decreased to ≈2 Ω^{-1} cm^{-1} (instead of 5–6 Ω^{-1} cm^{-1} for curve *1*) and the peak width increased to about 1 mm. Similar profiles were also observed for still lower HE densities down to 1.44 g/cm^3.

The width of the conductivity peak generally corresponds to the reaction zone thicknesses reported in [6]. Significant narrowing of the peak and growth of the conductivity amplitude at a high density also agree with published data on a sharp increase in the reaction rate under such conditions. The chemical peak could not be resolved in agatized HEs (pressed with acetone to a 99% of the maximum possible (crystal) density)) [7, 8] and even in RDX with a density above 1.72 g/cm^3 [9]. In our experiments, the boundary between narrow and broad profiles occurs between 1.64 and 1.75 g/cm^3, in agreement with [9]. However, the conductivity peak is well resolved even at higher densities. The difference can be explained (following [8]) by a less homogeneous structure of the charge obtained by pressing without acetone; alternatively, the conductivity decay may be delayed after termination of the main reaction stage.

The "tail" following the main conductivity peak is also more pronounced for the samples of higher density. This can be explained by an increase in the carbon yield or in the ionization degree at high densities and pressures.

Conclusions. We have developed an improved method based on high-resolution conductivity measurements for the investigation of detonation wave structure in high-density HEs. The results of experiments with RDX confirm a sharp increase in the reaction rate at high densities of the explosive.

Acknowledgments. The authors are grateful to S.D. Gilev and A.M. Trubachev for fruitful discussions.

This study was supported by the Russian Foundation for Basic Research (project no. 02-03-32873) and by the INTAS Foundation (project no. 03-51-3332).

REFERENCES

1. A. A. Brish, M. S. Tarasov, and V. A. Tsukerman, Zh. Éksp. Teor. Fiz. **37**, 1543 (1959) [Sov. Phys. JETP **10**, 1095 (1960)].
2. B. Hayes, in *Proceedings of the 4th International Symposium on Detonation, White Oak, 1965* (Office of Naval Research, Washington, 1967), Rep. No. ACR-126, pp. 595–601.
3. A. P. Ershov, P. I. Zubkov, and L. A. Luk'yanchikov, Fiz. Goreniya Vzryva **10**, 864 (1974).
4. A. G. Antipenko, A. N. Dremin, and V. V. Yakushev, Dokl. Akad. Nauk SSSR **225**, 1086 (1975).
5. D. G. Tasker and R. J. Lee, in *Proceedings of the 9th International Symposium on Detonation, Portland, 1989*, pp. 396–406.
6. A. N. Dremin, S. D. Savrov, V. S. Trofimov, and K. K. Shvedov, *Detonation Waves in Condensed Media* (Nauka, Moscow, 1970) [in Russian].
7. V. K. Ashaev, G. S. Doronin, and A. D. Levin, Fiz. Goreniya Vzryva **24**, 95 (1988).
8. B. G. Loboĭko and S. N. Lyubyatinskiĭ, Fiz. Goreniya Vzryva **36** (6), 45 (2000).
9. A. V. Utkin, S. A. Kolesnikov, and S. V. Pershin, Fiz. Goreniya Vzryva **38** (5), 111 (2002).

Translated by P. Pozdeev

Technical Physics Letters, Vol. 30, No. 12, 2004, pp. 1051–1053. Translated from Pis'ma v Zhurnal Tekhnicheskoĭ Fiziki, Vol. 30, No. 24, 2004, pp. 70–76.

A Theory of Pulse-Periodic Radiative High-Pressure Cesium Discharge

F. G. Baksht* and V. F. Lapshin

Ioffe Physicotechnical Institute, Russian Academy of Sciences, St. Petersburg, 194021 Russia

** e-mail: baksht@mail.ioffe.ru*

Received July 27, 2004

Abstract—The gasdynamics of pulse-periodic discharge in high-pressure cesium vapor has been self-consistently modeled for the first time. The discharge is an effective light source with a continuous spectrum and a luminous efficacy of $\eta_V = 74$ lm /W. Under conditions where the optical thickness of plasma in most part of the spectrum is close to unity, the main mechanisms of energy transfer in the discharge volume are nonlocal radiative heat exchange and radiative heat conduction. © *2004 MAIK "Nauka/Interperiodica".*

Introduction. Low-current pulsed discharge is widely used in illumination engineering. At a low rate of current buildup ($dI/dt < 10^8$ A/s), the discharge current channel expands at a subsonic velocity. This type of discharge has been extensively studied [1–10], but the investigations were mostly devoted to regimes in which the discharge plasma is transparent for continuous radiation. Previously [11, 12], we demonstrated that the plasma of a pulse-periodic discharge in cesium vapor at a pressure of $p \sim 1$ bar has an optical thickness on the order of unity in the continuum. The discharge spectrum was qualitatively analyzed by considering an immobile column of cesium plasma with a homogeneous temperature [11] or with a model radial temperature profile [12].

In this study, the gasdynamics of pulse-periodic discharge in high-pressure cesium vapor is self-consistently modeled for the first time and it is shown that a plasma with the required optical characteristics can be actually obtained in this discharge, provided that its parameters are properly selected. The spectrum of cesium discharge is calculated. It is demonstrated that this discharge can be used as a source of radiation with almost continuous spectrum in the visible range and a high luminous efficacy.

Model of discharge. We consider a discharge in a ceramic (Al_2O_3) tube with an inner diameter of 1.5–4 mm. The plasma of auxiliary stationary discharge is maintained by passing a current of $I_{st} \sim 0.1$–1.0 A. The pulse-periodic discharge is initiated by a pulsed current with an amplitude of $I_{max} \sim 30$–200 A, a frequency of $\nu \sim 500$–2000 Hz, and a duty ratio of $k \sim 0.04$–0.1. Under these conditions, the temperature at the discharge axis reaches 6000–7000 K and the discharge plasma density is $n_e \sim 10^{17}$–10^{18} cm^{-3}.

Under the conditions studied, the plasma of pulse-periodic discharge is axisymmetric and occurs in the state of local thermodynamic equilibrium [12]. This plasma is described by the following system of equations,

$$\frac{\partial}{\partial t}(n_i + n_a) + \frac{1}{r}\frac{\partial}{\partial r}[r(n_a V_a + n_i V_i)] = 0, \quad (1)$$

$$\frac{\partial}{\partial r}p_a = n_a n_i R_{ai}(V_i - V_a), \quad (2)$$

$$\frac{\partial}{\partial r}(p_e + p_i) = n_i n_a R_{ai}(V_a - V_i), \quad (3)$$

$$\frac{\partial}{\partial t}\left(\frac{3}{2}p + n_a E_a + n_i E_i\right)$$

$$+ \frac{1}{r}\frac{\partial}{\partial r}\left\{r\left[\frac{5}{2}(p_a V_a + p_i V_i + p_e V_e) + n_a V_a E_a + n_i V_i E_i\right]\right\}$$

$$= \sigma_e E^2 + \frac{1}{r}\frac{\partial}{\partial r}r(\lambda_e + \lambda_a + \lambda_{rad})\frac{\partial T}{\partial r} - U \equiv Q, \quad (4)$$

$$I(t) = 2\pi E(t)\int_0^R \sigma_e(r) r dr, \quad (5)$$

where p_i, p_e, p_a and n_i, n_e, n_a are the partial pressures and number densities of ions, electrons, and cesium atoms, respectively; V_i, V_e, V_a are the radial hydrodynamic velocities of these species (it is assumed that the radial current to walls is zero and $V_i = V_e$); R_{ai} are the drag coefficients calculated as described in [9]; E_i is the ionization energy; E_a is the energy of excitation of cesium atoms averaged over the Boltzmann distribution; E is the longitudinal electric field strength in the plasma; $T(r, t)$ is the plasma temperature; σ_e is the electron conductivity; and λ_e and λ_a are the electron and atomic heat conductivities. The values of λ_e and σ_e

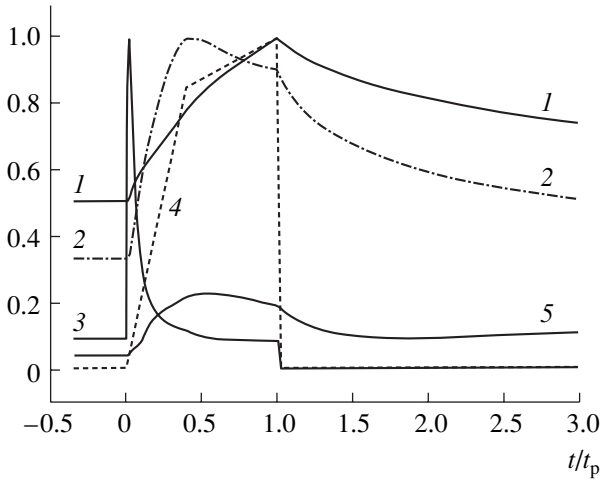

Fig. 1. Time variation of the main discharge parameters: (*1*) pressure $P(t)/P_{max}$; (*2*) temperature at the discharge axis $T_0(t)/T_{0\,max}$; (*3*) electric field strength in the plasma $E(t)/E_{max}$; (*4*) current pulse envelope $I(t)/I_{max}$; (*5*) energy fraction U_c/U_h absorbed in the cold region.

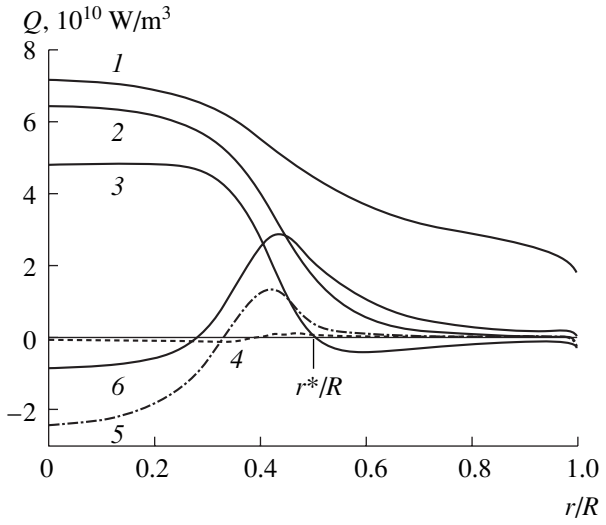

Fig. 2. Radial profiles of the temperature and volume rates of energy deposition at the time $t/t_p = 0.5$: (*1*) $10^{-3}T(r)$ K; (*2*) σE^2; (*3*) U; (*4*) $\frac{1}{r}\frac{\partial}{\partial r} r(\lambda_e + \lambda_a)\frac{\partial T}{\partial r}$; (*5*) $\frac{1}{r}\frac{\partial}{\partial r} r\lambda_{rad}\frac{\partial T}{\partial r}$; (*6*) Q (total rate of energy evolution per unit volume).

were calculated using the Frost formula for the kinetic coefficients of electrons in a partly ionized gas; $\lambda_a(T) = (T/T_0)^{1/2}\lambda_0$, where λ_0 is the heat conductivity of neutral cesium at $T_0 = 1500$ K. In Eq. (4), the term with λ_{rad} describes the energy released in the plasma in the optically dense part of the spectrum (over which integration is performed for calculating the radiative heat conduction [13]) and the term $U = \frac{1}{r}\frac{\partial}{\partial r}(r\int F_\lambda\, d\lambda)$ accounts for the radiative losses of the plasma energy in the remaining part of the spectrum. The calculations were performed in the spectrum interval 250 nm < λ < 9000 nm.

The radial flux F_λ of the radiant energy was expressed via equilibrium spectral intensity of radiation, $I_{\lambda P} = 2hc^2\lambda^{-5}[\exp(hc/\lambda k_B T) - 1]^{-1}$ as

$$F_\lambda(r, t) = 4\int_0^{\pi/2} d\psi \cos\psi \int_0^{\pi} d\theta \cos\theta \times \int_0^{l_w(r,\theta)} \kappa_\lambda(l) I_{\lambda P}(l) \exp\left(-\frac{1}{\cos\psi}\int_0^{l} \kappa_\lambda(l')dl'\right) dl, \quad (6)$$

where $l_w = (R^2 - r^2\sin^2\theta)^{1/2} + r\cos\theta$. The method of calculation and details of notations are described elsewhere [12].

In this study, it was assumed that the temperature distribution in the discharge tube wall and the number of cesium atoms C per unit length of the tube are constant during the pulse. The tube wall is assumed to be transparent for the emission from plasma. In this case, the boundary conditions for Eqs. (1)–(4) can be written as

$$\left.\frac{\partial T}{\partial r}\right|_{r=0} = 0, \quad T|_{r=R} = T_w, \quad 2\pi\int_0^R r(n_i + n_a)dr = C. \quad (7)$$

The temperature T_w of the inner wall of the tube was determined by solving a stationary heat conduction equation for the wall [9]

$$T_w = \left[\frac{q_w}{\varepsilon_w\sigma_{SB}(1 + \Delta R/R)}\right]^{1/4} + q_w\frac{R}{\lambda_w}\ln\left(1 + \frac{\Delta R}{R}\right),$$

where

$$q_w = \nu\int_0^{1/\nu}\left(-\lambda_a\frac{\partial T}{\partial r}\right)\Bigg|_{r=R} dt,$$

λ_w is the heat conductivity of the wall, q_w is the period-average heat flux from plasma to the wall due to the atomic heat conductivity (note that, near the wall, λ_e, $\lambda_{rad} \ll \lambda_a$); ε_w is the emissivity of the outer tube surface, σ_{SB} is the Stephan–Boltzmann constant, and ΔR is the wall thickness.

Results of calculations and discussion. Figures 1–3 show the results of calculations performed for I_{max} = 200 A, R = 4 mm, ν = 1000 Hz, k = 1/22. The number of cesium atoms per unit length of the tube was $C = 2\pi P_{sat}\int_0^R \frac{r\,dr}{k_B T_{st}(r)} = 2.77 \times 10^{19}$ cm^{-1}, which corresponds to the saturated vapor pressure P_{sat} = 750 Torr at the cold tube end (T_{cold} = 940 K); $T_{st}(r)$ is the temperature profile in the auxiliary discharge.

Figure 1 shows time variation of the main discharge parameters (in relative units normalized to maximum

values). The time t/t_p is measured in units of the pulse width, $t_p = k/\nu$; the maximum values of the field strength, pressure, and temperature are E_{max} = 378 V/cm, P_{max} = 1475 Torr, and $T_{0\,max}$ = 7080 K. It should be noted that the radial temperature profiles in this discharge are significantly less steep than those in the discharge where the plasma is optically transparent for the continuum [1, 4, 8, 10]. This is related to the fact that the energy U_c absorbed in the cold plasma amounts to a considerable part of the energy U_h emitted from the hot plasma in the continuum (Fig. 1); here $U_h = 2\pi\int_0^{r^*} r\,U(r)dr$ and $U_c = -2\pi\int_{r^*}^{R} r\,U(r)dr$, where r^* is the point determined from the condition $U(r^*) = 0$ (Fig. 2).

Figure 2 compares various mechanisms of plasma heating in the system. As can be seen, the maximum energy deposition Q takes place in the region of maximum temperature gradient (thermal front) at $r/R \sim 0.45$. This is related to the maximum divergence of radiant flux in this region. Heating of the cold region ($r/R > 0.55$) is provided for the most part at the expense of absorption of the continuum recombination radiation (here, $U < 0$). Formation of a thermal wave with a sharp temperature front under these conditions is impossible.

Another important feature of the discharge under consideration is the nearly continuous character of the emission spectrum. Figure 3 shows a period-average spectral flux of radiation $F_{rad}(\lambda) = \nu\int_0^{\nu^{-1}} F_\lambda(R, t)dt$ emitted from the plasma. As can be seen, the spectrum is almost continuous and covers the entire visible spectral range, which corresponds to a light source with high color-rendering index. We have calculated the period-average luminous flux per unit plasma column length as $\Phi = 2\pi RK_{max}\int_{380\text{ nm}}^{760\text{ nm}} F_{rad}(\lambda)V(\lambda)d\lambda$, where $V(\lambda)$ is the spectral luminous efficiency of radiation and K_{max} = 683 lm/W is the maximum luminous efficacy reached at λ = 555 nm. For the discharge regime under consideration, the luminous flux is Φ = 21600 lm/cm for a period-average consumed power of P = 290 W/cm. Thus, the luminous efficacy of the discharge is $\eta_V = \Phi/P$ = 74 lm/W.

To summarize, we demonstrated that important features of the pulse-periodic discharge in high-pressure cesium vapor are (i) predominance of the radiative mechanisms of energy transfer in the discharge plasma and (ii) a virtually continuous spectrum of radiation emitted from the plasma, concentrated for the most part in the visible spectral range. The total luminous efficacy of pulse-periodic cesium discharge significantly exceeds those of other radiation sources with continuous spectra, in particular, of mercury-free sources such as xenon lamps [14].

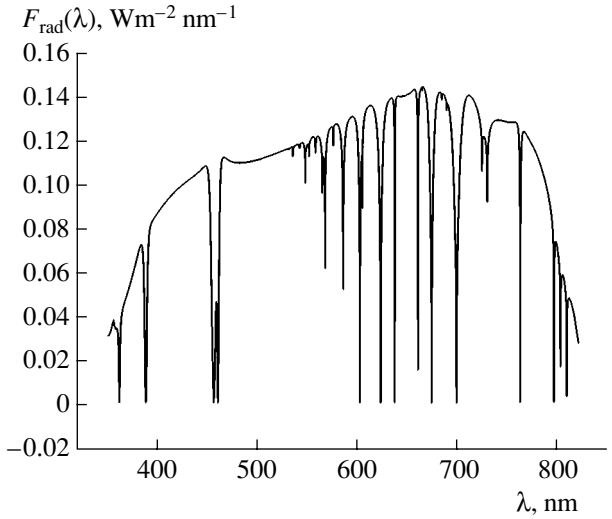

Fig. 3. Period-average spectrum of radiation emitted from discharge plasma.

REFERENCES

1. C. L. Chalek and R. E. Kinsinger, J. Appl. Phys. **52**, 716 (1981).
2. H. P. Stormberg and R. Schäfer, J. Appl. Phys. **54**, 4338 (1983).
3. J. T. Dakin and T. H. Rautenberg, J. Appl. Phys. **56**, 118 (1984).
4. E. A. Azizov, A. V. Kobelevskiĭ, and A. F. Nastoyashchiĭ, Fiz. Plazmy **12**, 362 (1986) [Sov. J. Plasma Phys. **12**, 211 (1986)].
5. E. A. Ershov-Pavlov, N. I. Chubrik, and V. D. Shimanovich, Teplofiz. Vys. Temp. **26**, 17 (1988).
6. Yu. Yu. Abramov, E. A. Azizov, and S. G. Solodovnikov, Fiz. Plazmy **15**, 97 (1989) [Sov. J. Plasma Phys. **15**, 57 (1989)].
7. K. Günter, H.-G. Kloss, T. Lehmann, *et al.*, Contrib. Plasma Phys. **30**, 715 (1990).
8. A. S. An'shakov, V. I. Nazaruk, and S. M. Khaĭtman, Teplofiz. Aérodin. **3**, 81 (1996).
9. F. G. Baksht and V. F. Lapshin, Zh. Tekh. Fiz. **66** (11), 170 (1996) [Tech. Phys. **41**, 1177 (1996)].
10. F. G. Baksht and V. F. Lapshin, Zh. Tekh. Fiz. **67** (9), 22 (1997) [Tech. Phys. **42**, 1004 (1997)].
11. F. G. Baksht and V. F. Lapshin, Pis'ma Zh. Tekh. Fiz. **23** (24), 40 (1997) [Tech. Phys. Lett. **23**, 961 (1997)].
12. F. G. Baksht and V. F. Lapshin, Zh. Tekh. Fiz. **72** (7), 100 (2002) [Tech. Phys. **47**, 894 (2002)].
13. F. G. Baksht and V. F. Lapshin, in *Abstracts of the Conference on the Physics of Low-Temperature Plasma (FNTP-2004), Petrozavodsk, 2004*, Chap. 1, pp. 56–61.
14. *A Handbook on Illumination Engineering*, Ed. by Yu. B. Aĭzenberg (Énergoatomizdat, Moscow, 1995) [in Russian].

Translated by P. Pozdeev

Technical Physics Letters, Vol. 30, No. 12, 2004, pp. 1054–1056. Translated from Pis'ma v Zhurnal Tekhnicheskoĭ Fiziki, Vol. 30, No. 24, 2004, pp. 77–81.

Gratings Formed during Nonlinear Recording of Superimposed Holograms

V. V. Orlov

Vavilov Optical Institute, State Scientific Center of the Russian Federation, St. Petersburg, 190164 Russia
e-mail: orlov@soi.spb.su

Received April 21, 2004

Abstract—Nonlinear recording of superimposed holograms has been theoretically studied. In the case of holograms recorded by method of angular or phase multiplexing, nonlinearity of the recording process leads to the appearance of gratings of two types, both meeting Bragg's condition in the course of reconstruction. The gratings of one type change the hologram diffraction efficiency, while those of the other give rise to diffractional cross-talk. The strength of gratings responsible for the cross-talk decreases until vanishing with increasing mutual orthogonality of the hologram object waves. © *2004 MAIK "Nauka/Interperiodica".*

The interest in investigations of superimposed holograms is related to the prospects of developing a holographic memory in which the data are stored in the form of superimposed volume holograms [1, 2]. In solving this task, it is especially important to study the noises and cross-talk arising in the course of reconstruction of a superimposed hologram and determine the dependence of these factors on the properties of the recording medium.

The aim of this study was to develop a theory of gratings appearing on superimposed holograms in the case on nonlinear dependence of the permittivity increment on the exposure [3–5] and to determine the influence of such gratings on the waves reconstructed by holograms.

Let M superimposed holograms be recorded by method of angular or phase multiplexing, with the reference and object waves composed of N plane waves (components). Among these, the first M components form the reference waves, while the remaining N–M form the object waves. The complex amplitude of the nth component during recording of the mth hologram is denoted by u_{mn}, where $m = 1, 2, \ldots, M$ and $n = 1, 2, \ldots, N$. Let the entire reference wave be of the same intensity Q. In the case of angular multiplexing, the reference waves have a single component and their complex amplitudes obey the relation $u_{mn} = \sqrt{Q}\exp(i\varphi_n)\delta_{mn}$, where δ_{mn} is the Kronecker delta ($\delta_{mn} = 1$ for $m = n$; $\delta_{mn} = 0$ for $m \neq n$). In the case of phase multiplexing, the complex amplitudes of the reference waves obey the relation $u_{mn} = \sqrt{\frac{Q}{M}}\exp(i\varphi_{mn})$ ($m, n = 1, 2, \ldots, M$), and these reference waves are mutually orthogonal: $\sum_{n=1}^{M} u_{pn}^* u_{qn} = Q\delta_{pq}$.

During the mth hologram recording, the wave field $\psi_m(\mathbf{r})$ is described by the equation

$$\psi_m(\mathbf{r}) = \sum_{n=1}^{N} u_{mn}\exp(i\mathbf{k}_n\mathbf{r}), \tag{1}$$

where $\mathbf{r}$ is the radius vector and $\mathbf{k}_n$ is the wave vector of the nth component.

Let us assume that recording of the superimposed holograms involves, in addition to the linear term, a quadratic term in the dependence of the permittivity increment on the exposure. Then, the permittivity of superimposed holograms can be described as

$$\begin{aligned}\varepsilon(\mathbf{r}) = \varepsilon_0 + i\sigma_0 + \chi_1\varepsilon_0 t\sum_{m=1}^{M}\left|\psi_m(\mathbf{r})\right|^2 \\ + \chi_2\varepsilon_0\left[t\sum_{m=1}^{M}\left|\psi_m(\mathbf{r})\right|^2\right]^2,\end{aligned} \tag{2}$$

where ε_0 is the initial permittivity of the recording medium, σ_0 is a change in the imaginary part of the permittivity cased by processing of the recording medium, t is the time of recording of each superimposed hologram, $\chi_1 = \chi_1' + i\chi_1''$ is the complex factor of proportionality between the linear permittivity increment and the exposure, and $\chi_2 = \chi_2' + i\chi_2''$ is the complex factor of proportionality between the quadratic permittivity increment and the exposure.

1063-7850/04/3012-1054$26.00 © 2004 MAIK "Nauka/Interperiodica"

The permittivity described by relation (2) is a sum of two components. The first of these,

$$\varepsilon_1(\mathbf{r}) = \varepsilon_0 + i\sigma_0 + \chi_1 t\varepsilon_0 \sum_{m=1}^{M} |\psi_m(\mathbf{r})|^2 = \varepsilon_0 + i\sigma_0 + \chi_1 t\varepsilon_0 \sum_{m=1}^{M}\sum_{n=1}^{N}\sum_{l=1}^{N} u_{mn}u_{ml}^* \exp[i(\mathbf{k}_n - \mathbf{k}_l)\mathbf{r}] \quad (3)$$

reflects the linear dependence of the permittivity increment on the exposure, while the second,

$$\varepsilon_2(\mathbf{r}) = \chi_2\varepsilon_0\left[t\sum_{m=1}^{M}|\psi_m(\mathbf{r})|^2\right]^2 = \chi_2\varepsilon_0 t^2 \times \sum_{m=1}^{M}\sum_{n=1}^{N}\sum_{l=1}^{N}\sum_{p=1}^{M}\sum_{q=1}^{N}\sum_{g=1}^{N} u_{mn}u_{ml}^* u_{pq}u_{pg}^* \times \exp[i(\mathbf{k}_n - \mathbf{k}_l + \mathbf{k}_q - \mathbf{k}_g)\mathbf{r}], \quad (4)$$

is a quadratic function of the exposure. For any combination of indices (n, l, q, g), relation (4) describes a permittivity grating arising as a result of the quadratic nonlinearity.

In what follows, we will consider only gratings for which the incidence of any component of the reference or object waves and the subsequent diffraction under Bragg's conditions leads to a combination of the same waves. Such gratings have vectors equal to the differences of two wave vectors, $\mathbf{k}_i - \mathbf{k}_j$ ($i, j = 1, 2, \ldots, N$) and arise in four cases corresponding to the following values of indices:

$$\text{(i)}\ n = l, \quad \text{(ii)}\ q = g,$$

$$\text{(iii)}\ n = g, \quad \text{(iv)}\ l = q.$$

In cases (i) and (ii), the gratings have equal vectors, phases, and amplitudes. The sum of permittivities for these gratings is described by the expression

$$\varepsilon_{21}(\mathbf{r}) = 2\chi_2\varepsilon_0 t^2 J \sum_{m=1}^{M}\sum_{n=1}^{N}\sum_{l=1}^{N} u_{mn}u_{ml}^* \exp[i(\mathbf{k}_n - \mathbf{k}_l)\mathbf{r}], \quad (5)$$

where $J = \sum_{m=1}^{M}\sum_{n=1}^{N}|u_{mn}|^2$ is the sum of intensities of the reference and object waves for all superimposed holograms. A comparison of expressions (5) and (3) shows that the permittivities of gratings (5) are proportional to those of gratings (3). The amplitudes of gratings (5) are (depending on the sign of χ_2) added to or subtracted from the amplitudes of gratings (3), thus increasing or decreasing, respectively, the hologram diffraction efficiency.

The gratings appearing in cases (iii) and (iv) also have equal vectors, phases, and amplitudes. The sum of permittivities for these gratings is

$$\varepsilon_{23}(\mathbf{r}) = 2\chi_2\varepsilon_0 t^2 \times \sum_{m=1}^{M}\sum_{l=1}^{N}\sum_{p=1}^{M}\sum_{q=1}^{N}(Q\delta_{pm} + G_{pm})u_{ml}^* u_{pq}\exp[i(\mathbf{k}_q - \mathbf{k}_l)\mathbf{r}], \quad (6)$$

where $G_{pm} = \sum_{n=1}^{M} u_{pn}^* u_{mn}$ is the scalar product of the pth and mth object waves. For $p = m$, gratings (6) coincide with gratings (5) and, hence the hologram diffraction efficiency also increases or decreases.

For $p \neq m$, gratings (6) acquire the following form:

$$\varepsilon_{23}(\mathbf{r}) = 2\chi_2\varepsilon_0 t^2 \times \sum_{\substack{m=1\\ m\neq p}}^{M}\sum_{l=1}^{N}\sum_{p=1}^{M}\sum_{q=1}^{N} G_{pm}u_{ml}^* u_{pq}\exp[i(\mathbf{k}_q - \mathbf{k}_l)\mathbf{r}]. \quad (7)$$

These gratings, while having vectors ($\mathbf{k}_q - \mathbf{k}_l$) ($q, l = 1, 2, \ldots, N$) equal to those of gratings (3), differ from the latter gratings by a factor of G_{pm}, modulating both the phase and amplitude. For this reason, the wave field arising as a result of diffraction on gratings (7) is a cross-talk field relative to the wave field formed due to the diffraction on gratings (3). According to expression (7), quadratic nonlinearity leads to the formation of gratings corresponding to the interference of reference waves of the superimposed holograms. These gratings correspond to the indices q. $l = 1, 2, \ldots, M$, $q \neq l$. For these indices, Eq. (7) can be rewritten as

$$\varepsilon_{23}(\mathbf{r}) = 2\chi_2\varepsilon_0 t^2 Q \times \sum_{\substack{l=1\\ l\neq q}}^{M}\sum_{q=1}^{M} G_{pl}\exp i(\varphi_q - \varphi_l)\exp[i(\mathbf{k}_q - \mathbf{k}_l)\mathbf{r}]. \quad (8)$$

Gratings (8) give rise to cross-talk as a result of two wave diffraction events. Indeed, during the reconstruction of one hologram, the reference wave of this hologram exhibits diffraction on gratings (8) and reconstructs the reference waves of the other superimposed holograms. The reference waves of these hologram in the second diffraction event reconstruct the corresponding object waves, representing in this case the diffractional cross-talk. It is important to note that the amplitudes of gratings (7) and (8) decreases until vanishing with increasing mutual orthogonality of the hologram object waves, whereby $G_{pm} \longrightarrow 0$ for $p \neq m$. Therefore, in order to reduce the aforementioned cross-talk during

holographic recording, it is expedient to use the amplitude–phase method of data encoding, which increases mutual orthogonality of the hologram object waves [6, 7].

Acknowledgments. This study was supported by the Russian Foundation for Basic Research (project no. 01-02-17854) and the Presidential Program of Support for Leading Scientific Schools in Russia (project no. NSh-98.2003.2).

REFERENCES

1. A. A. Akaev, S. B. Gurevich, K. M. Zhumaliev, *et al.*, *Holography and Optical Information Processing: Selected Items* (Bishkek, 2003) [in Russian].
2. H. J. Coufal, D. Psaltis, and G. T. Sincerbox, *Holographic Data Storage* (Springer, Heidelberg, 2000).
3. S. Fries, S. Bauschulte, E. Kratzig, *et al.*, Opt. Commun. **84**, 251 (1991).
4. E. M. de Miguel-Sanz, J. Limeres, L. Arizmendi, *et al.*, J. Opt. Soc. Am. B **16**, 1658 (1999).
5. J. Limeres, E. M. de Miquel-Sanz, A. Suchocki, *et al.*, Opt. Mater. **18**, 115 (2001).
6. V. V. Orlov, Proc. SPIE **3402**, 84 (1998).
7. V. V. Orlov, Opt. Spektrosk. **92**, 1024 (2002) [Opt. Spectrosc. **92**, 948 (2002)].

Translated by P. Pozdeev

Technical Physics Letters, Vol. 30, No. 12, 2004, pp. 1057–1059. Translated from Pis'ma v Zhurnal Tekhnicheskoĭ Fiziki, Vol. 30, No. 24, 2004, pp. 82–87.

Sources of Modulated Structures Appearing in Crystals under the Action of Variable External Factors

E. E. Slyadnikov

Tomsk Scientific Center, Siberian Division, Russian Academy of Sciences, Tomsk, Russia

e-mail: slyad@cc.tpu.edu.ru

Received July 21, 2004

Abstract—It is shown that pacemakers spontaneously arising at inhomogeneities of a medium play the role of local sources for the formation of a modulated structure (inhomogeneous inelastic strain) in a structurally unstable crystal. © *2004 MAIK "Nauka/Interperiodica".*

In many crystals exhibiting martensite transitions under the action of variable external factors (temperature, external force, etc.), experiments reveal precursor states and modulated structures [1, 2]. Published data indicate that, in the course of variation of the external action, an inhomogeneously distributed inelastic strain spontaneously arises in such samples as a result of self-organization of the crystal. The observed spatiotemporal pattern of inhomogeneous inelastic strain has the form of a phase autowave propagating in the material [3]. It was experimentally established that the law of dispersion of such phase waves has a parabolic character (see [4, Fig. 1)].

Within the framework of a recently developed microscopic model [5, 6], the formation of precursor states with modulated structures is related to the appearance of an inhomogeneous condensate of autosolitons, or an inhomogeneously distributed phase of the order parameter. However, the thermodynamical approach developed in [6] allows only the initial and final states of the crystal to be determined. Therefore, it would be important to study the dynamics of transition to a modulated crystal structure.

When the external action (temperature, external force) reaches a critical level σ_c, the interaction of autosolitons with local atomic displacements leads to instability of the state of a crystal with the ideal gas of autosolitons with respect to the formation of a Bose condensate of autosolitons [5, 6]. Thus, the crystal passes to a precursor state representing a coherent state with the condensate of autosolitons. Owing to the coherency, the motion of this condensate can be described in terms of a wave function of the single soliton $\Psi = |\Psi|\exp(-i[\omega_0 t - \Phi(\mathbf{r})])$, which is the order parameter of the system. The square amplitude of the order parameter is equal to the density of autosolitons, while the phase gradient is equal to the wave vector of a modulated crystal structure. Fluctuations of the order parameter depending on the phase gradient lead, on the one hand, to the appearance of inhomogeneities in the condensate and, on the other hand, to the formation of a modulated crystal structure (inhomogeneous inelastic strain). However, in order to provide for a stable existence of inhomogeneities in the condensate, there must exist a source of formation of the phase gradient. It will be demonstrated below that pacemakers spontaneously arising in the regions of inhomogeneity of the crystal act as sources for the formation of inhomogeneous condensate of autosolitons.

The inhomogeneous complex order parameter $\Psi(\mathbf{r}, t)$ is described by the evolution equation [6]

$$\begin{aligned}\dot{\Psi}(\mathbf{r}, t) &= \lambda(\rho)\Psi(\mathbf{r}, t) - i\omega(\rho)\Psi(\mathbf{r}, t) \\ &+ (D_1 + iD_2)\nabla^2\Psi(\mathbf{r}, t),\end{aligned} \quad (1)$$

where the upper dot denotes differentiation with respect to time, $\lambda(\rho) = -\alpha_1 - \beta_1|\Psi(\mathbf{r}, t)|^2$, $\omega(\rho) = \alpha_2 + \beta_2|\Psi(\mathbf{r}, t)|^2$, and α_1, α_2, β_1, β_2, D_1, D_2 are the coefficients and constants determined in [6]. As can be seen from Eq. (1), the function $\lambda(\rho)$ becomes zero at $\rho = \rho_0 = (\alpha_1/\beta_1)^{1/2}$, is negative for $\rho > \rho_0$, and is positive for $\rho < \rho_0$. Thus, the condensate of autosolitons is an autooscillatory medium described by the λ–ω model [7].

If the complex diffusion coefficient $D = D_1 + iD_2$ in Eq. (1) is zero, the condensate represents a set of uncorrelated points performing autooscillations according to the law $\Psi(t) = \rho_0\exp[-i(\omega_0 t + \varphi)]$, where ρ_0 is the amplitude determined from the condition $\lambda(\rho_0) = 0$ and $\omega_0 = \omega(\rho_0)$ is the frequency; ρ_0^2 is the density of generated autosolitons; ω is the energy of autosolitons in the condensate; and φ is the initial phase of autooscillations. This homogeneous regime of autooscillations corresponds to a state with the homogeneous density of the condensate and the homogeneous crystal structure. According to the relation $\delta\dot{\rho} = \rho_0\lambda'(\rho_0)\delta\rho$ (where the prime denotes differentiation with respect to ρ), small amplitude perturbations $\delta\rho = \rho - \rho_0$ for the condensate

1063-7850/04/3012-1057$26.00 © 2004 MAIK "Nauka/Interperiodica"

point decay with time, and the amplitude relaxation time is $t_{rel} = |\rho_0/(\partial\lambda/\partial\rho)_{\rho=\rho_0}|^{-1} = |(1/2\alpha_1)|$.

Assuming that $D \neq 0$ and substituting the order parameter $\Psi(\mathbf{r}, t) = \rho(\mathbf{r}, t)\exp[-i(\omega_0 t + \varphi(\mathbf{r}, t))]$ into Eq. (1), we obtain

$$\dot{\rho} = \lambda(\rho)\rho + D_1\nabla^2\rho - D_1\rho(\nabla\varphi)^2 + D_2\rho\nabla^2\varphi + 2D_2(\nabla\rho)(\nabla\varphi), \quad (2)$$

$$\dot{\varphi} = [\omega(\rho) - \omega_0] + 2D_1\rho^{-1}(\nabla\rho)(\nabla\varphi) - D_2\rho^{-1}\nabla^2\rho + D_2(\nabla\varphi)^2 + D_1\nabla^2\varphi. \quad (3)$$

Assuming also that the phase relaxation time t_L is large as compared to the amplitude relaxation time t_{rel}, let us consider (following [8]) only smooth distributions of the order parameter with a large spatial length L. Then, the amplitude deviations $\delta\rho(\mathbf{r}, t)$ will adiabatically adjust to $\nabla\varphi$ and $\nabla^2\varphi$ at the corresponding points of the condensate. Substituting $\rho = \rho_0 + \delta\rho$ and $\delta\rho = \rho_0 t_{rel}[D_2\nabla^2\varphi - D_1(\nabla\varphi)^2]$ into Eq. (3), we obtain for the homogeneous crystal the relation

$$\dot{\varphi} = a(\nabla\varphi)^2 + b\nabla^2\varphi, \quad (4)$$

where $a = -(\beta_2/\beta_1)D_1 + D_2$ and $b = (\beta_2/\beta_1)D_2 + D_1$ are coefficients with dimensionality of the diffusion coefficient and $\omega(\rho) = \omega_0$. As can be seen from Eq. (2), the relaxation time t_L is on the order of $\approx L^2/b$. Therefore, the equation of phase dynamics (4) is only applicable to the description of smooth phase distributions with large spatial lengths $L \gg (bt_{rel})^{1/2}$.

Substituting $\varphi(\mathbf{r}, t) = (b/a)\ln(Q(\mathbf{r}, t))$ into Eq. (4), we obtain

$$\dot{Q} = b\nabla^2 Q. \quad (5)$$

As can be seen from Eq. (5), evolution of the condensate phase is determined by the sign of the coefficient b. In the case of positive b, any local inhomogeneity Q, φ with a characteristic length L decays and completely vanishes over a period of time on the order of t_L. Thus, any fluctuation in the phase of the order parameter in a homogeneous condensate exhibits a decay, while modulation of the crystal structure caused by this fluctuation disappears.

When the phase wave propagates in the condensate, there appears a constant gradient of the phase of autooscillations, $\nabla\varphi = -\mathbf{q} = \text{const}$ [6, 8]. Autooscillations of the neighboring condensate points in the direction of vector $\mathbf{q}$ proceed with a constant phase shift, as if a phase autowave would propagate in the condensate. This wave corresponds to a partial solution $\varphi = -\mathbf{qr} + aq^2t$ of Eq. (4). The shift in the frequency of autooscillations is $\omega = \omega_0 + aq^2$, while the velocity of the wave propagation is $c = \omega_0/q + aq$. As can be seen from Eq. (4) all autowaves are stable for $b > 0$. This regime of autooscillations of the condensate corresponds to the state with a modulated crystal structure (inhomogeneous inelastic strain) with the wave vector $\mathbf{q}$.

In order to excite phase waves in the condensate, it is necessary to create an initial gradient of the phase of autooscillations, which is possible only in the presence of a source of such a phase gradient (inhomogeneity of the crystal). In the region of crystal inhomogeneity, the frequency $\omega(\mathbf{r})$ of autooscillations exceeds the frequency ω_0 of oscillations of the other points in the condensate, but $\omega(\mathbf{r}) \longrightarrow \omega_0$ when $r \longrightarrow \infty$. Then, the condensate phase dynamics in the inhomogeneous crystal is described by the following equation:

$$\dot{\varphi} = \omega(\mathbf{r}) - \omega_0 + a(\nabla\varphi)^2 + b\nabla^2\varphi. \quad (6)$$

By substituting $\varphi(\mathbf{r}, t) = (b/a)\ln(Q(\mathbf{r}, t))$, this expression can be reduced to the linear relation,

$$\dot{Q} = b\nabla^2 Q + (a/b)[\omega(\mathbf{r}) - \omega_0]Q, \quad (7)$$

which is equivalent to the Schrödinger equation. Within the framework of the Schrödinger equation, the fact that the condition $\omega(\mathbf{r}) > \omega_0$ is valid in a certain region implies that this region contains a potential well. As is known [9], for any bound state of a particle in a potential well, the wave function exponentially decays over a sufficiently large distance from the well center. Assuming that the potential well contains a single bound state, we find that, far from the region of perturbation localization,

$$\varphi(\mathbf{r}, t) = (b/a)\ln[C_0 + C_1\exp(\lambda_1 t - (\lambda_1/b)^{1/2}r)], \quad (8)$$

where λ_n are the eigenvalues of the linear operator $\hat{L}\mu = \lambda\mu$, $\hat{L} = b\nabla^2 + (a/b)[\omega(\mathbf{r}) - \omega_0]$. This solution describes the source of phase autowaves (pacemaker) appearing in the region of inhomogeneity of the crystal. Inside the growing spherical region of radius $R(t) = (b\lambda_1)^{1/2}t$, we have a system of concentric, divergent phase autowaves $\varphi(\mathbf{r}, t) = (b/a)[\lambda_1 t - (\lambda_1/b)^{1/2}r]$ with frequency $\omega = \omega_0 + (b/a)\lambda_1$ and wavenumber $k = (\lambda_1 b/a^2)^{1/2}$, which lead to the formation of a modulated crystal structure (inhomogeneous inelastic strain).

The above results lead to the conclusion that a crystal exhibiting a structural phase transition stimulated by an external variable factor (temperature, external force, etc.) behaves as an autooscillatory medium. The dynamics of formation of a modulated crystal structure (inhomogeneous inelastic strain) has the form of a phase autowave propagating along the sample. The law of dispersion of such phase waves $\omega = \omega_0 + aq^2$ has an experimentally observed parabolic character [4]. This behavior of dispersion is related to the presence of autosolitons of a nonlocal interaction proportional to

$\nabla^2\Psi(\mathbf{r}, t)$. In turn, the physical reason for the formation of the condensate of autosolitons is the interaction of nonlocal atomic displacements (single excitations of the crystal lattice) with autosolitons (collective excitations). It is this interaction that leads to the generation of an inhomogeneous condensate of autosolitons. This condensate exhibits nonlinear properties and obeys the nonlinear Schrödinger equation (1). Pacemakers spontaneously arising at inhomogeneities of the medium play the role of local sources for the formation of a modulated structure (inhomogeneous inelastic strain) in a structurally unstable crystal.

REFERENCES

1. V. E. Panin, V. A. Likhachev, and Yu. V. Grinyaev, *Structural Levels of Deformation in Solids* (Nauka, Novosibirsk, 1985) [in Russian].
2. V. G. Pushin, V. V. Kondrat'ev, and V. N. Khachin, *Pre-Transient Phenomena and Martensite Transformations* (Russian Academy of Sciences, Ekaterinburg, 1998) [in Russian].
3. L. B. Zuev, V. I. Danilov, and B. S. Semukhin, Usp. Fiz. Met., No. 3, 237 (2002).
4. S. A. Barannikova, Pis'ma Zh. Tekh. Fiz. **30** (8), 75 (2004) [Tech. Phys. Lett. **30**, 338 (2004)].
5. E. E. Slyadnikov, Fiz. Tverd. Tela (St. Petersburg) **46**, 1065 (2004) [Phys. Solid State **46**, 1095 (2004)].
6. E. E. Slyadnikov, Izv. Vyssh. Uchebn. Zaved., Fiz., No. 7 (Suppl.), 59 (2004).
7. P. Bak and V. J. Emery, Phys. Rev. Lett. **36**, 978 (1976).
8. A. Yu. Loskutov and A. S. Mikhaĭlov, *Introduction to Synergetics* (Nauka, Moscow, 1990) [in Russian].
9. L. D. Landau and E. M. Lifshitz, *Course of Theoretical Physics*, Vol. 3: *Quantum Mechanics: Non-Relativistic Theory* (Nauka, Moscow, 1989, 4th ed.; Pergamon, New York, 1977, 3rd ed.).

Translated by P. Pozdeev

Technical Physics Letters, Vol. 30, No. 12, 2004, pp. 1060–1063. Translated from Pis'ma v Zhurnal Tekhnicheskoĭ Fiziki, Vol. 30, No. 24, 2004, pp. 88–94.

The Virtual Cathode Velocity during Electron Beam Transport in a Drift Tube

S. Ya. Belomyttsev, A. A. Grishkov, S. D. Korovin, and V. V. Ryzhov*

Institute of High-Current Electronics, Siberian Division, Russian Academy of Sciences, Tomsk, Russia

** e-mail: ryzhov@to.hcei.tsc.ru*

Received July 5, 2004

Abstract—A solution corresponding to a thin annular electron beam in a homogeneous drift tube featuring a uniformly moving virtual cathode (VC) has been obtained. The dependence of the VC velocity on the injected and transmitted currents is determined and it is established that this velocity has a limiting value. Theoretical results agree with the results of numerical calculations performed by means of the electromagnetic PIC code KARAT. © *2004 MAIK "Nauka/Interperiodica".*

The results of our previous numerical calculations [1–3] showed that the injection of an electron beam into a two-section drift tube leads, under certain conditions, to the formation of a virtual cathode (VC) near the joint cross section. When the injected current reaches a certain critical value, the VC begins to move in the direction opposite to the electron beam propagation direction and the so-called "squeezed" state is formed behind the VC [1, 3]. This phenomenon can be used, for example, for the collective acceleration of electrons [4]. This study had the aim of determining the VC velocity in a homogeneous drift tube.

The values of currents of an annular electron beam corresponding to stationary states in a drift tube with immobile VC were determined in [5]. In order to obtain solutions corresponding to a moving VC, let us pass to an inertial frame of reference *K*' moving at a velocity of *V* along the drift tube. Then, the frame *K*' will feature a VC moving at a velocity *V* in the reverse direction.

Consider a homogeneous transport tube in an immobile inertial frame of reference *K*, in which a thin annular electron beam (Fig. 1) is characterized by the current *I*, the electron velocity V_b, and the radius R_b. On the outer boundary of the beam, the electric field strength is

$$E_r = \frac{2I\gamma_b}{c\sqrt{\gamma_b^2 - 1}}\frac{1}{R_b} \quad (1)$$

and the magnetic field strength is

$$H_\varphi = \frac{2I}{c}\frac{1}{R_b}, \quad (2)$$

where $\gamma_b = 1/\sqrt{1 - V_b^2/c^2}$ is the relativistic factor for electrons in the beam. In the inertial frame of reference *K*' moving at a velocity *V* along the *z* axis, the Lorentz transformations for the electric and magnetic field strengths are as follows [6]:

$$E_r' = \frac{E_r \pm \frac{V}{c}H_\varphi}{\sqrt{1 - \frac{V^2}{c^2}}} = \gamma\left(E_r \pm \frac{V}{c}H_\varphi\right), \quad (3)$$

$$H_\varphi' = \gamma\left(H_\varphi \mp \frac{V}{c}E_r\right), \quad (4)$$

where $\gamma = 1/\sqrt{1 - V^2/c^2}$ is the relativistic factor. The upper and lower signs in Eqs. (3) and (4) correspond to the *K*' frame moving in the same direction as particles

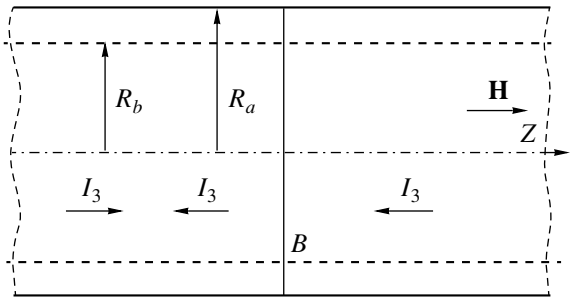

Fig. 1. The geometry of a homogeneous transport tube with a thin annular electron beam: R_a, the tube radius; R_b, the beam radius; I_1, I_2, I_3, the transmitted current, the forward current, and the current of electrons reflected from the VC, respectively, in frame *K* where the VC is at rest in the cross section *B*. The dashed contour shows the calculation region.

1063-7850/04/3012-1060$26.00 © 2004 MAIK "Nauka/Interperiodica"

in the injected beam and in the opposite direction, respectively.

Using relations (1), (2), and (4), it is possible to relate the beam current in frame K' to that in frame K:

$$I' = \frac{cR_bH_j'}{2} = I\gamma\left(\mathrm{Im}\frac{\gamma_b\sqrt{\gamma^2-1}}{\gamma\sqrt{\gamma_b^2-1}}\right). \quad (5)$$

Thus, upon going to system K', the currents I_1, I_2, and I_3 (Fig. 1) have to be replaced by

$$I_1' = I_1\gamma\left(1 \mp \frac{\gamma_1\sqrt{\gamma^2-1}}{\gamma\sqrt{\gamma_1^2-1}}\right), \quad I_2' = I_2\gamma\left(1 \mp \frac{\gamma_2\sqrt{\gamma^2-1}}{\gamma\sqrt{\gamma_2^2-1}}\right),$$
$$I_3' = I_3\gamma\left(1 \pm \frac{\gamma_2\sqrt{\gamma^2-1}}{\gamma\sqrt{\gamma_2^2-1}}\right). \quad (6)$$

Using the nonrelativistic rule of adding velocities, we readily determine the relativistic factors for the beams in frame K':

$$\gamma_1' = \gamma\gamma_1 \mp \sqrt{\gamma^2-1}\sqrt{\gamma_1^2-1}, \quad \gamma_2' = \gamma\gamma_2 \mp \sqrt{\gamma^2-1}\sqrt{\gamma_2^2-1},$$
$$\gamma_3' = \gamma\gamma_2 \pm \sqrt{\gamma^2-1}\sqrt{\gamma_2^2-1}. \quad (7)$$

Once the relativistic factors γ' (7) and the electric field strength (1) are known, we may calculate the applied voltage (Γ') corresponding to beams 1, 2, and 3 in frame K':

$$\Gamma_2' = \Gamma\gamma \mp \sqrt{\gamma^2-1}\sqrt{\gamma_2^2-1} \mp \frac{(\Gamma-\gamma_1)\sqrt{\gamma_1^2-1}\sqrt{\gamma^2-1}}{\gamma_1},$$

$$\Gamma_1' = \Gamma\gamma \mp \sqrt{\gamma^2-1}\sqrt{\gamma_1^2-1} \mp \frac{(\Gamma-\gamma_1)\sqrt{\gamma_1^2-1}\sqrt{\gamma^2-1}}{\gamma_1}, \quad (8)$$

$$\Gamma_3' = \Gamma\gamma \mp \sqrt{\gamma^2-1}\sqrt{\gamma_2^2-1} \mp \frac{(\Gamma-\gamma_1)\sqrt{\gamma_1^2-1}\sqrt{\gamma^2-1}}{\gamma_1}.$$

Using these formulas and the solution for a stationary system with an immobile VC [5], it is possible to determine the VC velocity and the corresponding currents for a beam transported in the drift tube in the regime of a moving VC.

Figure 2 shows a plot of the relativistic factor γ calculated using formulas (6)–(8) for a VC moving to the left (toward the injection region) versus the injected current I_2' for various fixed values of the transmitted current I_1' for $\Gamma_2' = 2$, $R_a = 1$ cm, and $R_b = 0.61$ cm. As can be seen from these results, the function $\gamma = f(I_2')$ at a given value of the transmitted current has two branches: the "slow" branch, corresponding to low values of the VC velocity for $I_{\mathrm{Tr}} < I_2' < I_{2\max}'$, and the "fast" (upper) branch for $I_1' < I_2' < I_{2\max}'$. At high injection currents, $I_{\mathrm{Tr}} < I_2' < I_{2\max}'$, the VC velocity has two values, while at low currents, $I_1' < I_2' < I_{\mathrm{Tr}}$, there are solutions described only by the fast branch.

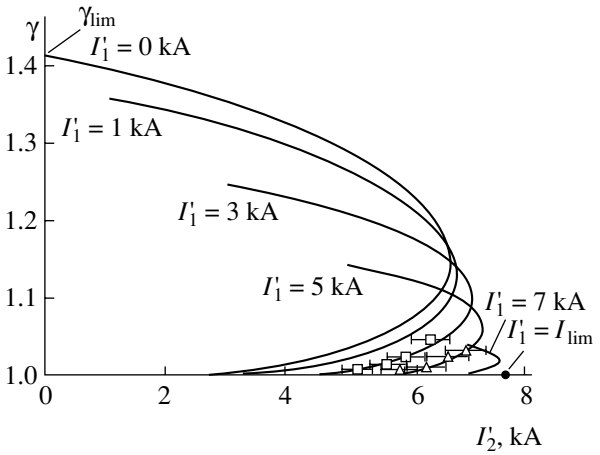

Fig. 2. Plot of the relativistic factor corresponding to the VC velocity for various values of the injected current at various values of the transmitted current for $\Gamma_2' = 2$, $R_1 = 1$ cm; $R_b = 0.61$ cm. Points present the results of model calculations using PIC code KARAT for a transmitted current of (□) $I_1' = 3$ kA and (Δ) $I_1' = 5$ kA. Error bars indicate the scatter related to fluctuations of the calculated current around the average values; $\gamma_{\mathrm{lim}} = 1/\sqrt{1-(V_{\mathrm{lim}}^L)^2/c^2}$.

The results of calculations showed that, for a given transmitted current, the injected current I_1' has a certain maximum value $I_{2\max}'$. This is related to limitation of this current by the field of the space charge of the forward and reverse (reflected) currents in the system with a moving VC. For the maximum value of the transmitted current such that $I_1' = I_{1\mathrm{lim}}'$, at which the dependence $\gamma = f(I_2')$ degenerates into a point on the abscissa axis and the VC velocity is zero ($V = 0$, $\gamma = 0$), the maximum injected current is equal to the limiting current for the homogeneous drift tube: $I_{2\max}' = I_{\mathrm{lim}}$ (Fig. 2). For the injection currents above the limiting value, $I_2' > I_{2\max}'$, stationary states of a beam with uniformly moving VC do not exist.

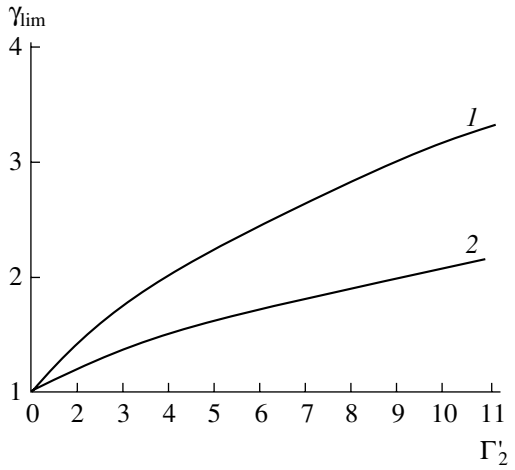

Fig. 3. Plot of the relativistic factor corresponding to the limiting VC velocity γ_{lim} versus Γ_2' for the (*1*) leftward and (*2*) rightward motion.

An analysis of the results of calculations showed that the slow branch can be realized in the case of unilateral injection of a magnetized electron beam into the section of smaller radius in a two-section drift tube. In this case, each value of the transmitted current corresponds to a certain critical injected current I_{Tr} (transition current) [3], at which the VC begins to move in the plane of current injection. The values of these currents correspond to the points of intersection of the curves describing the slow branch with the I_2' axis. For example, in the case of $I_1' = 0$, the curve intersects the abscissa axis at $I_2' = I_{Tr} = I_F/2$, which corresponds to a minimum value of the transition current. Note that the point of intersection of the curve for $I_1' = 0$ with the ordinate axis corresponds to the limiting velocity V_{lim}^L of the leftward VC motion ($\gamma_{lim} = 1/\sqrt{1-(V_{lim}^L)^2/c^2}$).

The points in Fig. 2 show the VC velocities determined from the results of modeling the electron beam injection into a two-section drift tube using the electromagnetic PIC code KARAT [7] for two values of the transmitted current, $I_1' = 3$ and 5 kA. As can be seen from these data, the results of modeling agree well with the results of calculations using formulas obtained in this study. Analysis showed that the upper branches of the curves in Fig. 2 correspond to injected beams on the left (slow) branch of the transport curve (i.e., to the "squeezed" states).

Formally speaking, the solutions obtained are valid for any velocity $V < c$. Each velocity V determines certain values of currents in frame K'. In order to determine the range of possible values of the VC velocities, it is necessary to introduce some physical restrictions. If the VC moves in the direction opposite to the injected beam, then the transmitted beam has to move in the same direction as the injected one. Let us determine the limiting VC velocity (V_{max}^L) in this case for the VC moving leftward (toward the injection region). Since the transmitted beam behind the VC occurs on the slow branch of the transport curve in the frame K [5], it has a velocity in the interval from zero up to a velocity corresponding to the relativistic factor $\gamma_1 = \Gamma^{1/3}$. Therefore, the limiting velocity of the leftward VC motion also corresponds to $\gamma_1 = \Gamma^{1/3}$, that is, to the case of a beam crossing the VC without reflection [5]. In this limiting case, the transmitted beam in frame K' is stopped. This corresponds to $\Gamma_2' = \Gamma^{2/3}$, but Γ_2' is the relativistic factor corresponding to the applied voltage in frame K', so that

$$\gamma_{lim}^L = \Gamma^{1/3} - \sqrt{\Gamma_2'}, \quad V_{lim}^L = c\sqrt{1-\frac{1}{\Gamma_2'}}. \tag{9}$$

The results of calculations using formula (9) are presented in Fig. 3 (curve *1*).

In the case when the VC moves rightward (away from the injection region), we can naturally introduce a restriction according to which the reflected beam is stopped when the VC velocity reaches the limiting value V_{lim}^R. Then, relation (7) yields $V_{lim}^R = \gamma_{2lim}$ (because the injected and reflected beams in frame K have the same relativistic factors γ). However, $\gamma_{2lim} = \gamma_F$, where $\gamma_F = \sqrt{2\Gamma + 1/4} - 1/2$ is the relativistic factor corresponding to the Fedosov current. Then, relation (8) yields

$$\Gamma_2' = \gamma_F^2 + \Gamma\gamma_F - 1. \tag{10}$$

These relations determine the dependence of the limiting velocity of the rightward VC motion, γ_{lim}^R, and the corresponding relativistic factor, γ_{lim}^R on the Γ_2' value (Fig. 3, curve *2*).

An analysis of the results described above suggests that the VC velocity can be controlled. By injecting a beam into a two-section drift tube and gradually increasing the beam current with time, it is possible to obtain a situation where the VC moves with acceleration. For the results obtained in this study to be applicable, it is only necessary that the regime would be quasistationary; that is, the injected current increment over the characteristic electron drift time must be sufficiently small.

Acknowledgments. This study was supported by the Russian Foundation for Basic Research, project no. 04-02-16527a.

REFERENCES

1. A. M. Ignatov and V. P. Tarakanov, Phys. Plasmas **1**, 741 (1994).
2. A. E. Dubinov and I. E. Efimova, Zh. Tekh. Fiz. **71** (6), 800 (2001) [Tech. Phys. **46**, 723 (2001)].
3. A. A. Grishkov, S. Ya. Belomyttsev, S. D. Korovin, and V. V. Ryzhov, Pis'ma Zh. Tekh. Fiz. **29** (22), 46 (2003) [Tech. Phys. Lett. **29**, 944 (2003)].
4. A. E. Dubinov, I. Yu. Kornilova, and V. D. Selemir, Usp. Fiz. Nauk **172**, 1225 (2002) [Phys. Usp. **45**, 1109 (2002)].
5. S. Ya. Belomyttsev, A. A. Grishkov, S. D. Korovin, and V. V. Ryzhov, Pis'ma Zh. Tekh. Fiz. **29** (16), 16 (2003) [Tech. Phys. Lett. **29**, 666 (2003)].
6. L. D. Landau and E. M. Lifshitz, *Course of Theoretical Physics*, Vol. 2: *The Classical Theory of Fields* (Nauka, Moscow, 1988; Pergamon, Oxford, 1975).
7. V. P. Tarakanov, *User's Manual for Code Karat* (Berkley, Springfield, 1992).

Translated by P. Pozdeev

Technical Physics Letters, Vol. 30, No. 12, 2004, pp. 973–975. Translated from Pis'ma v Zhurnal Tekhnicheskoĭ Fiziki, Vol. 30, No. 23, 2004, pp. 1–7.

The Mechanism of Mechanical Energy Accumulation in a Nonwetting Liquid–Nanoporous Solid System

V. D. Borman, A. A. Belogorlov*, A. M. Grekhov, G. V. Lisichkin, V. N. Tronin, and V. I. Troyan

Moscow Institute of Engineering Physics (State University), Moscow, 115409 Russia

** e-mail: a_belogorlov@mail333.com*

Received June 15, 2004

Abstract—The mechanism of mechanical energy accumulation in a nanoporous solid–nonwetting liquid system has been experimentally studied by filling a silica gel based nanoporous sorbent (Libersorb 2U-8) with an aqueous ethylene glycol solution. Interpretation of the experimental data within the framework of the previously developed percolation theory shows that the mechanical energy accumulated in this system is determined by a difference between the energy of formation of the porous solid–liquid interface and the dissipation energy related to the meniscus formation. © *2004 MAIK "Nauka/Interperiodica".*

One of the promising applications of nanotechnology is the development of novel devices capable of accumulating and absorbing mechanical energy that are based on the phenomenon of filling of a nanoporous solid with a nonwetting liquid [1–3]. The accumulation of mechanical energy in such systems is related to the fact that the filling process requires overcoming the Laplace pressure and performing work to create a disperse liquid surface. The possibility of mechanical energy accumulation in the course of zeolite filling with a liquid metal was originally considered by Bogomolov [1–3]. Subsequent investigations showed that filling of a nanoporous solid with a nonwetting liquid is accompanied by the phenomena of hysteresis and liquid retention in (or incomplete discharge from) the pores [4]. As will be demonstrated below, these factors determine the possibility of accumulating mechanical energy in a nanoporous solid–nonwetting liquid system.

We have studied the possibility of accumulating mechanical energy by filling a nanoporous Libersorb 2U-8 sorbent with an aqueous solution of ethylene glycol (EG). The phenomena of hysteresis and liquid retention in the pores were described within the framework of a previously developed percolation theory taking into account the energy barrier for fluctuational formation and growth of the fractal clusters of filled and (upon liquid discharge) empty pores [5] using a nonscaled distribution function of the fractal clusters [6]. It was established that the energy spent for filling pores in the system studied consists of two parts: (i) the energy E_s of reversible processes involved in the formation of a liquid–solid boundary surface and (ii) the energy E_m consumed in irreversible processes of meniscus formation and disappearance. The energy E_{ac} accumulated in the solid is determined by the difference $E_s - E_m$ and depends on the parameters of the nonwetting liquid and nanoporous solid.

Libersorb 2U-8 is a KSK-G grade silica gel with a SiO_2 skeleton and the surface chemically modified [7] so as to render it hydrophobic. Data on the specific pore volume and average pore size in Libersorb 2U-8 are presented in the table. The working liquid was an aqueous EG solution. According to published data [8], the surface energy of these solutions monotonically decreases from 72 to 49 mJ/m^2 when the EG concentration increases from $C = 0$ to 1.0.

A weighed amount (4.00 ± 0.05 g) of Libersorb 2U-8 powder with a grain size of 10–63 μm was placed into a high-pressure chamber, the chamber was filled with an EG solution, and the change in the volume V of the nanoporous solid–nonwetting liquid was measured as a function of the applied pressure. The high-pressure chamber allowed the experiments to be performed at

Characteristics of the Libersorb–aqueous EG solution system for various EG concentrations

C	σ, mJ/m^2 [8]	p_2, atm	$\frac{V_0}{V_{por}}$	δσ, mJ/m^2	E, J/g	σ/δσ
0.00	72.0	220	0.05	23.0	8.9	3.1
0.06	69.0	200	0.24	21.0	8.1	3.3
0.11	66.0	190	0.66	19.0	7.7	3.5
0.16	64.0	175	0.76	17.0	7.2	3.8
0.35	61.0	160	1.00	15.0	6.5	4.1
0.60	56.0	125	1.00	12.5	6.1	4.5
0.75	53.0	105	1.00	9.0	4.9	5.9
1.00	49.0	65	1.00	2.0	3.3	24.5

1063-7850/04/3012-0973$26.00 © 2004 MAIK "Nauka/Interperiodica"

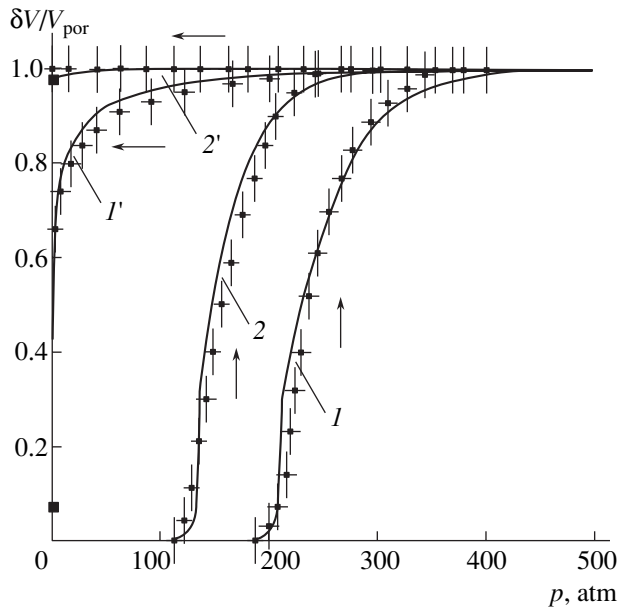

Plots of the specific liquid volume $\delta V/V_{por}$ versus excess pressure p, measured for Libersorb 2U-8–nonwetting liquid systems with (*1*, *1*') water and (*2*, *2*') aqueous EG solution ($C = 0.6$) in the stages of (*1*, *2*) charging and (*1*', *2*') discharging. Solid curves show the results of theoretical calculations using modified percolation theory [5].

pressures up to 10^3 bar. The pressure excess above atmospheric and the volume V were measured using a pressure gauge and a position-sensitive transducer, respectively, with an error not exceeding 10%. The rate of pressure variation did not exceed 1 bar/s, which allowed the pore filling process to be considered as quasi-static. The experimental procedure is described in more detail elsewhere [5].

Plots of the specific volume of liquid ($\delta V/V_{por}$) versus pressure in the nonwetting liquid–nanoporous solid system studied are presented in the figure. The measurements were performed until complete filling (plots *1* and *2*) of the pores and in the course of subsequent decrease of the excess pressure to zero (plots *1*' and *2*', respectively) in the Libersorb–EG solution system with the EG solution concentrations $C = 0$ (*1*, *1*') and 0.6 (*2*, *2*'). The data were corrected for the deformations of the porous solid, the chamber, and the liquid. The value of V_{por} for Libersorb 2U-8, determined as the difference of the liquid volumes after and before filling, was independent of the EG solution concentration and amounted to $V_{por} = 0.38 \pm 0.02$ cm^3/g. As can be seen from the figure, the system filled with the liquid at $C = 0$ (i.e., with pure water) exhibits hysteresis and incomplete discharge of the liquid. As the solution concentration increases from 0 to 0.1, the relative volume of liquid retained in the pores grows from 0.05 to 0.66 (see table). At $C = 0.6$, the system exhibits complete retention of liquid in the pores. In this case, the pressure of complete filling decreases from $p_2 = 220$ bar at $C = 0$ to $p_2 = 125$ bar at $C = 0.6$ (see table). Using the measured $V(p)$ curves, we determined the energy spent for filling the porous solid as $E = \int_0^\infty p(V)dV$, which was accumulated (except the dissipation losses) in the form of the energy of the newly formed boundary surface. The values of E corresponding to various surface energies σ of the solution are given in the table.

Solid curves in the figure show the theoretical dependences calculated within the framework of the percolation theory taking into account the energy barriers for filling the pores and for the discharge of a nonwetting liquid from the porous solid [5]. However, in this study (in contrast to the model considered in [5]), we used a nonscaled distribution function of the fractal clusters formed by filled pores [6],

$$F(n, p) = cn^{-\nu}\exp\left[\frac{-|\vartheta_v(p) - \vartheta_c|n}{\vartheta_c}\right], \qquad (1)$$

where $\nu \cong 2.2$ [6, 9], c is the normalization factor, $\vartheta_c = 0.16$ is the relative-volume percolation threshold for the given three-dimensional medium, $n \gg 1$ is the number of available pores, and $\vartheta_v(p)$ is the relative volume of available pores at the pressure p. The distribution function (1) takes into account the formation of fractal clusters with dimensions both smaller and greater than the correlation length, appearing as a result of their mutual interaction during the filling of the porous solid.

The pressure dependences of the specific volume of filled pores ($V_{in}(p)$) and empty pores ($V_{out}(p)$) formed upon pressure release, as well as the volume V_0 of the liquid retained in the pores, were calculated using the formulas [5]

$$V_{in}(p) = \int_1^\infty F(n, p)\vartheta_{in}(p)dn,$$

$$V_{out}(p) = \int_1^\infty F(n, p)\vartheta_{out}(p)dn, \qquad (2)$$

$$V_0 = \frac{4}{3}\pi\int_0^r R^3 f(R)dR,$$

where r is the pore radius determining the boundary below which the pores cannot enter into the cluster of empty pores [5]; $\vartheta_{in}(p)$ and $\vartheta_{out}(p)$ are the relative volumes of available filled and empty pores, respectively. The latter quantities are determined by the surface energies of the liquid σ and the porous solid–liquid interface ($\delta\sigma = \sigma_{sg} - \sigma_{sl}$) and by the average pore size $\bar{R}$. The pore size distribution function $f(R)$ for Libersorb 2U-8 was set as a normal distribution with the center at $\bar{R} = 3.6$ nm and a halfwidth of $\delta R = 0.4$ nm. Relations (2) take into account that, when the pressure is

increased to a level corresponding to the percolation threshold, $\vartheta_{in}(p) = \vartheta_c = 0.16$, an infinite fractal cluster is formed from the available pores, and the porous solid is filled in the state close to this threshold.

In the description of experimental data, the unknown parameter $\delta\sigma$ was selected so as to provide that the two dependences, $V_{in}(p)$ and $V_{out}(p)$, and the volume V_0 of retained liquid in the experiment with water ($\sigma = 72$ mJ/m^2), would be correctly described to within the experimental error. The value of $\delta\sigma$ estimated in the experiment with water was then used in the comparison of experimental and theoretical data for aqueous EG solutions of various concentrations. Satisfactory coincidence of the theoretical $V_{in}(p)$ and $V_{out}(p)$ dependences with experimental data at an EG solution concentration of $C \approx 0.6$ is illustrated in the figure (solid curves *2* and *2*').

The comparison of theory and experiment shows the possibility of a quantitative description of the hysteresis, the retention of liquid, and, hence, the accumulation of energy in the charge–discharge cycles in the porous solid–nonwetting liquid system under consideration based on the percolation theory taking into account the fluctuational filling of pores and the formation of empty pores (liquid discharge) upon pressure release [5]. Within the framework of this model, the total energy required for the complete filling of a solid can be written as

$$E = E_s + E_m = S(1-\eta)\delta\sigma + S\eta\sigma, \qquad (3)$$

where S is the total surface of pores and η is the ratio of the meniscus and pore surface areas. The first term ($E_s = S_s\delta\sigma$) on the right-hand side of Eq. (3) describes the work performed by external forces, which is spent in reversible processes involved in the formation and disappearance of a liquid–solid boundary surface. The second term ($E_m = S_m\sigma$) is the energy consumed in irreversible processes of formation (disappearance) of menisci in each filled (empty) pore. The latter processes lead to energy dissipation during the filling of a porous solid with a liquid. In the initial (unfilled porous solid) and the final (same solid completely filled with liquid) state, the menisci are absent. The discharge of a liquid from a porous solid proceeds provided that $E_m/E_s < 1$. Thus, the accumulation of energy in the porous solid takes place when the stored energy E_s exceeds the irreversible losses taking place during discharge as a result of the formation and disappearance of menisci. As can be seen from data in the table, the E and $\delta\sigma$ values exhibit monotonic growth with increasing σ.

Using Eq. (3), the energy ratio E_m/E_s can be expressed as

$$\frac{E_m}{E_s} = \frac{\sigma}{\delta\sigma}\frac{\eta}{(1-\eta)}. \qquad (4)$$

For Libersorb 2U-8, a comparison of the experimental data to theoretical dependences (1) and (2) gave a value of $\eta = 0.25$. Once the ratio $\sigma/\delta\sigma$ and the value of η are known, it is possible to estimate σ values for which the energy is accumulated in a given system. For the system under consideration, the accumulated energy varies from $E_{ac} = 1.1$ J/g to $E_{ac} \cong 0$ when the EG concentration is changed from $C = 0$ to 0.3. In this concentration interval, the pore filling–emptying cycle becomes irreversible and the hysteresis disappears (see figure). At higher EG concentrations, $E_s < E_m$, the liquid is completely retained in the porous solid, and, hence, the accumulation of energy becomes impossible.

REFERENCES

1. V. N. Bogomolov, Usp. Fiz. Nauk **124**, 171 (1978) [Sov. Phys. Usp. **21**, 77 (1978)].
2. V. N. Bogomolov, Phys. Rev. B **51**, 17040 (1995).
3. V. N. Bogomolov, Poverkhnost **9**, 136 (1992).
4. A. Yu. Fadeev and V. A. Eroshenko, Zh. Ros. Khim. O–va im. D. I. Mendeleeva **39**, 93 (1995).
5. V. D. Borman, A. M. Grekhov, and V. I. Troyan, Zh. Éksp. Teor. Fiz. **118**, 193 (2000) [JETP **91**, 170 (2000)].
6. A. A. Abrikosov, Pis'ma Zh. Éksp. Teor. Fiz. **29**, 72 (1979) [JETP Lett. **29**, 65 (1979)].
7. G. V. Lisichkin, A. Yu. Fadeev, A. A. Serdan, P. N. Nesterenko, P. G. Mingalev, and D. B. Furman, *Chemistry of Graft Surface Compounds* (Fizmatlit, Moscow, 2003) [in Russian].
8. K. Nakanishi, T. Matsumoto, and M. Hayatsu, J. Chem. Eng. Data **16**, 1 (1971).
9. M. B. Isichenko, Rev. Mod. Phys. **64**, 961 (1992).

Translated by P. Pozdeev

Technical Physics Letters, Vol. 30, No. 12, 2004, pp. 976–978. Translated from Pis'ma v Zhurnal Tekhnicheskoĭ Fiziki, Vol. 30, No. 23, 2004, pp. 8–14.

Thermostimulated Luminescence from Single Crystals of Modified Lithium Gadolinium Orthoborate $Li_{6-x}Na_xGd(BO_3)_3$:Ce

R. P. Yavetskiy* and A. V. Tolmachev

Institute of Single Crystals, National Academy of Sciences of Ukraine, Kharkov, Ukraine

** e-mail: yavetskiy@isc.kharkov.ua*

Received June 15, 2004

Abstract—We have grown single crystals of a $Li_6Gd(BO_3)_3$:Ce (LGBO:Ce) scintillation phosphor modified with sodium. The thermostimulated luminescence curves of the crystals of $Li_{6-x}Na_xGd(BO_3)_3$:Ce ($0.1 < x < 0.3$) exhibit, in addition to the peak at 425 K observed for the initial compound, a new intense peak at 362 K. The total thermoluminescence yield from the modified crystals is more than 20 times that of the initial (nonmodified) LGBO:Ce with a close Ce activator content (0.012–0.019 wt %). The energy accumulation in the new material is explained by the formation of hole traps of the V_{Li^+} type filled in the field of the $Na^+_{Gd^{3+}} + V_{O^{2-}}$ growth defect favoring the spatial separation of charge carriers. © *2004 MAIK "Nauka/Interperiodica".*

In recent years, much attention has been devoted to the development of storage media for thermal neutron detectors employing the phenomena of photo- (PSL) and thermostimulated (TSL) luminescence. New storage phosphors have been synthesized, in particular, those based on complex borates [1]. A phosphor for solid state TSL dosimeters must possess a high neutron capture cross section, low sensitivity to gamma radiation, and sufficiently high radiation resistance admitting the formation of radiation-induced defects participating in the radiative recombination of secondary charge carriers.

We have studied mixed lithium gadolinium orthoborate $Li_6Gd(BO_3)_3$:Ce (LGBO:Ce), which is a new, extensively developed scintillator for thermal neutron detectors [2–4]. Single crystals of the initial orthoborate $Li_6Gd(BO_3)_3$ possess a high radiation resistance, such that no energy storage is observed upon irradiation with β particles to a total absorbed dose of up to $\approx 10^8$ rad. Recently [5], it was reported for the first time that cerium-activated single crystals of this compound (LGBO:Ce) exhibit TSL in the form of a low-intensity peak at $T = 426$ K, which was attributed to the disintegration of a hole center related to the $Ce^{4+}_{Gd^{3+}} + V_{Li^+}$ complex. Thus, there arises the problem of directed modification of the crystal structure of this complex borate, aimed at the creation of effective energy storage centers. Naturally, such a modification must compromise between a certain number of defects introduced into the crystal lattice and the retained single-phase composition and base packing motif of the crystal.

We have selected sodium as the modifying additive, since it admits both the isovalent substitution of Na^+ for the matrix Li^+ ion and the heterovalent substitution of Na^+ for Gd^{3+}, accompanied by the formation of charge-compensating oxygen vacancies ($V_{O^{2-}}$). Single crystals of $Li_{6-x}Na_xGd(BO_3)_3$ and $Li_{6-x}Na_xGd(BO_3)_3$:Ce ($0.1 < x < 0.3$) with a diameter of up to 15 mm and a length of up to 20 mm were grown by the Czochralski technique in air, using platinum crucibles and $[4\bar{3}2]$ oriented seeds [6]. The initial charge was synthesized as described in [7]. The phase composition of the charge was checked by X-ray diffraction. As was reported previously [8], the oxide system Li_2O–Na_2O–Gd_2O_3–B_2O_3 admits the existence of a single-phase compound $Li_{6-x}Na_xGd(BO_3)_3$ with a modifier content of up to $x \le 0.3$. The content and the charged state of cerium activator ions were determined by plasma photometry using an SF-46 spectrophotometer (LOMO, Russia).

The optical measurements were performed using plane-parallel polished single crystals with the dimensions $7 \times 7 \times 2$ mm, cut perpendicularly to the crystal growth direction. The absorption spectra were recorded on a Specord M-40 UV-VIS spectrophotometer (Germany). The TSL curves were measured with an experimental setup using a FEU-79 photoelectron multiplier detector. The measurements were performed at a heating rate of ~5 K/s in a temperature range from 300 to 650 K. The samples were irradiated with β particles at room temperature using a $^{90}Sr/^{90}Y$ radionuclide source with an activity of 2 K. Below, we present the results of measurements performed for single crystals with the composition $Li_{5.7}Na_{0.3}Gd(BO_3)_3$:Ce.

1063-7850/04/3012-0976$26.00 © 2004 MAIK "Nauka/Interperiodica"

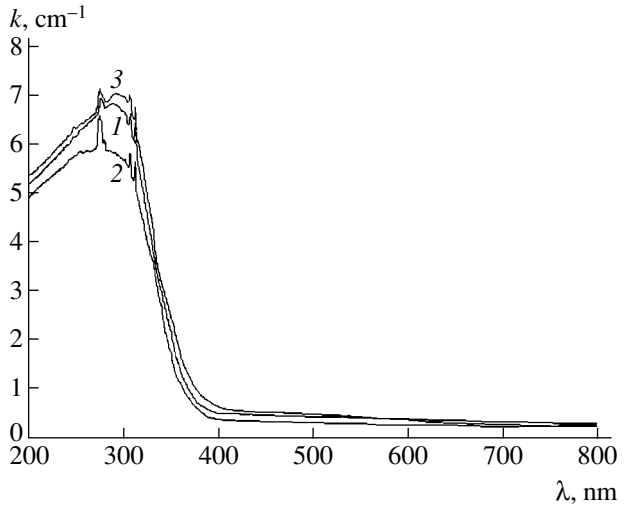

Fig. 1. The optical absorption spectra of $Li_{5.7}Na_{0.3}Gd(BO_3)_3$:Ce (4.5% Ce) measured (*1*) before and (*2*) after β-irradiation and (*3*) after heating in the TSL measurement regime.

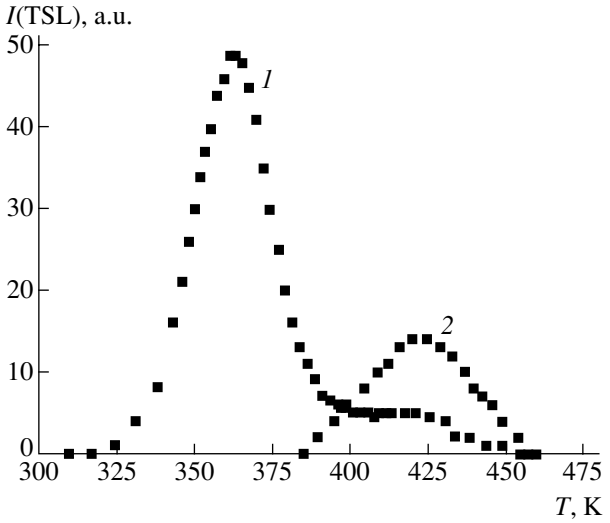

Fig. 2. TSL curves of crystals irradiated with β particles to a total absorbed dose of ~10^7 rad: (*1*) $Li_{5.7}Na_{0.3}Gd(BO_3)_3$:Ce (4.5% Ce); (*2*) $Li_6Gd(BO_3)_3$:Ce (4.5% Ce), ×10.

Irradiation of the nonactivated $Li_{5.7}Na_{0.3}Gd(BO_3)_3$ crystals with β particles (up to an absorbed dose of ~10^7 rad) does not lead to TSL. The optical absorption spectrum of $Li_{5.7}Na_{0.3}Gd(BO_3)_3$:Ce exhibits a broad band in the near-UV range with the maximum at a wavelength of $\lambda \approx 280$ nm and a set of bands in the regions of 245–255, 275–280, and 300–315 nm related to the *f–f* electron transitions in Gd^{3+} ions (Fig. 1, curve *1*) [9]. The band observed in the near-UV range is typical of glasses and crystals containing Ce^{4+} ions and is interpreted as the charge-transfer band corresponding to the electron transport from the 2*p* orbital of the oxygen ion to the unfilled 4*f* orbital of the cerium ion: $Ce^{4+} + O^{2-} \longleftrightarrow Ce^{3+} + O^-$ [10, 11]. According to the results of chemical analyses, the initial C^{4+}/Ce^{3+} ratio in the crystals is approximately 4:1.

After irradiation of the $Li_{5.7}Na_{0.3}Gd(BO_3)_3$:Ce crystals, the intensity of the band with a maximum at $\lambda \approx 280$ nm somewhat decreases ($\Delta k \approx 1$ cm^{-1}, see curve *2* in Fig. 1), which is indicative of a decrease in the C^{4+}/Ce^{3+} ratio:

$$Ce^{4+}_{Gd^{3+}} + V_{Li^+} + O^{2-} \longrightarrow \beta\text{-irradiation} \longrightarrow Ce^{3+}_{Cd^{3+}} + V^+_{Li^+} + O^-. \quad (1)$$

The stability of the recharged state $Ce^{4+}_{Gd^{3+}} \longrightarrow Ce^{3+}_{Cd^{3+}}$ is determined by that of a lithium vacancy that has trapped a hole ($V_{Li^+} + e^+ \longrightarrow V^+_{Li^+}$). Upon thermal deactivation of the hole center, the intensity of the absorption band at $\lambda \approx 280$ nm is restored on the initial level (Fig. 1, curve *3*). Therefore, a reverse process with respect to reaction (1) takes place, and the C^{4+}/Ce^{3+} ratio acquires its initial value. It should be emphasized that the presence of activator ions predominantly in the charged state Ce^{4+} is the key factor in the mechanism of energy storage in the system under consideration.

Figure 2 (curve *1*) shows the typical TSL curve of a β-irradiated $Li_{5.7}Na_{0.3}Gd(BO_3)_3$:Ce crystal. The initial nonactivated crystal exhibited no thermostimulated emission in the temperature range 300–620 K. As can be seen, the TSL curve exhibits two peaks: the low-temperature peak at $T_1 = 362$ K and the high-temperature peak at $T_2 \approx 420$ K (close to the position of the TSL peak in LGBO:Ce crystals). The energies of the thermal activation of traps are $E_1 \approx 0.76$ eV for the low-temperature peak and $E_2 \approx 0.82$ K for the high-temperature peak (the latter activation energy also virtually coincides with the analogous value for LGBO:Ce crystals [5]). Thus, we may suggest that the TSL peak at $T_2 \approx 420$ K in the modified crystals, as well as in the nonmodified material, is related to thermal decay of the $Ce^{3+}_{Cd^{3+}} + V^+_{Li^+}$ complex.

Based on an analysis of the experimental results, we suggest the following model for the process of radiation energy storage in $Li_{5.7}Na_{0.3}Gd(BO_3)_3$:Ce crystals. The substitution of sodium for gadolinium in the lattice sites is possible due to the close ionic radii of these elements ($r_{Na^+}(6) = 1.16$ Å, $r_{Gd^{3+}}(6) = 1.15$ Å) and the tendency to cationic disorder in crystals containing cations of similar sizes [12]. During the heterovalent substitution $Na^+ \longrightarrow Gd^{3+}$, the excess charge can be compensated by the formation of oxygen vacancies of the type $[Li_6][Gd_{1-x-y}Ce^{3+}_x Na_y][B_3][O_{9-y}\square_y]$, where [ ] is the lattice site and □ is the vacancy. The most probable

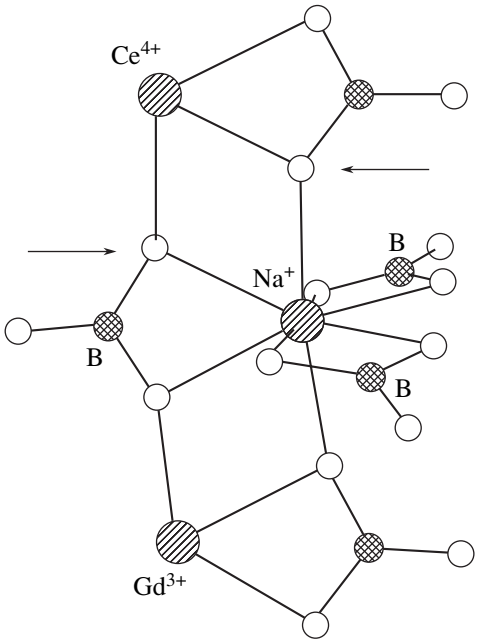

Fig. 3. Schematic diagram showing the structure of $Li_{5.7}Na_{0.3}Gd(BO_3)_3$ with a $Na^{+}_{Gd^{3+}} + V_{O^{2-}}$ growth defect. Arrows indicate the sites of localization of the oxygen vacancies (a lithium vacancy in the $Ce^{4+}_{Cd^{3+}} + V_{Li^{+}}$ defect is not depicted).

sites for localization of the oxygen vacancies are the positions of bridging oxygen ions linking the neighboring gadolinium ions into chains aligned in the [010] direction (Fig. 3) [13]. In a real crystal, the neighboring positions in the chains of gadolinium polyhedra can be occupied in such a way that one position belongs to a sodium ion ($Na^{+} \longrightarrow Gd^{3+}$ substitution with the formation of the $Na^{+}_{Gd^{3+}} + V_{O^{2-}}$ growth defect) and the other, to a cerium ion (defect of the $Ce^{4+}_{Cd^{3+}} + V_{Li^{+}}$ type). In this configuration, the hole center is perturbed by the nearest-neighbor oxygen vacancies ($V_{O^{2-}}$) and, hence, is characterized by somewhat different energy parameters as compared to those of the nonperturbed center. This difference accounts for the appearance of the additional TSL peak observed at a lower temperature T_1 = 362 K.

The total thermoluminescence yield from the modified crystals is more than 20 times that of the initial (nonmodified) LGBO:Ce with a close Ce activator content (0.012–0.019 wt %). We believe that the higher efficiency of energy accumulation in the $Li_{5.7}Na_{0.3}Gd(BO_3)_3$:Ce crystals as compared to that in nonmodified LGBO:Ce is related to a greater concentration of hole centers of the $V^{+}_{Li^{+}}$ type. This is favored by the anion nonstoichiometry of the modified crystals, that is, by the presence of additional $Na^{+}_{Gd^{3+}} + V_{O^{2-}}$ growth defects whose field facilitates the spatial separation of electron–hole pairs in the ionized crystal lattice. Adopting this mechanism of energy accumulation, we may expect that a similar phenomenon would be observed in the case of controlled nonstoichiometry, for example, in magnesium-modified LGBO:Ce crystals featuring growth defects of the $Mg^{2+}_{Li^{3+}} + V_{Li^{+}}$ type. The results of investigations of the TSL from such crystals will be published soon.

Acknowledgments. The authors are grateful to O.V. Gaiduk for his help in determining the concentration and charged state of cerium in grown crystals.

REFERENCES

1. A. V. Sidorenko, P. A. Rodnyi, and C. W. E. van Eijk, Pis'ma Zh. Tekh. Fiz. **29** (14), 33 (2003) [Tech. Phys. Lett. **29**, 586 (2003)].
2. J. P. Chaminade, O. Viraphong, F. Guillen, *et al.*, IEEE Trans. Nucl. Sci. **48**, 1158 (2001).
3. A. N. Shekhovtsov, A. V. Tolmachev, M. F. Dubovik, *et al.*, J. Cryst. Growth **242**, 167 (2002).
4. V. V. Chernikov, M. F. Dubovik, V. P. Gavrylyuk, *et al.*, Nucl. Instrum. Methods Phys. Res. A **498**, 424 (2003).
5. V. N. Baumer, M. F. Dubovik, B. V. Grinyov, *et al.*, in *Proceedings of the 5th European Conference on Luminescent Detectors and Transformers of Ionizing Radiation, Prague, 2003*, p. 201.
6. R. P. Yavetskiy, B. V. Grinev, M. F. Dubovik, *et al.*, in *Proceedings of the 10th National Conference on Crystal Growth, Moscow, 2002*, p. 218.
7. M. F. Dubovik, A. V. Tolmachev, R. P. Yavetskiy, *et al.*, Ukr. Patent Application No. 66072A (April 15, 2004); Byull. Izobret., No. 4 (2004).
8. T. I. Korshikova, R. P. Yavetskiy, and A. V. Tolmachev, Function. Mater. **10**, 407 (2003).
9. C. T. Garapon, B. J. Jacquier, J. P. Chaminade, *et al.*, J. Lumin. **34**, 211 (1985).
10. H. Ebendorff-Heidepriem and D. Ehrt, Opt. Mater. **15**, 7 (2000).
11. L. Van Pieterson, PhD Thesis (Proefschrift Univ., Utrecht, 2001).
12. A. A. Blistanov, *Crystals of Quantum and Nonlinear Optics* (MISiS, Moscow, 2000) [in Russian].
13. E. F. Dolzhenkova, V. N. Baumer, and S. I. Gordeev, Kristallografiya **48**, 614 (2003) [Crystallogr. Rep. **48**, 563 (2003)].

Translated by P. Pozdeev

Technical Physics Letters, Vol. 30, No. 12, 2004, pp. 979–982. Translated from Pis'ma v Zhurnal Tekhnicheskoĭ Fiziki, Vol. 30, No. 23, 2004, pp. 15–23.

Peculiarities of the Electron Diffraction from Nanostructured Objects in High-Symmetry Projections

S. K. Maksimov[a,*], R. Herrero[b], and B. P. Sobolev[c]

[a] *Moscow State Institute of Electronic Engineering (Technical University), Moscow, Russia*
[b] *Institute of Materials Science, Madrid, Spain*
[c] *Shubnikov Institute of Crystallography, Russian Academy of Sciences, Moscow, Russia*
* *e-mail: lemi@lemi.miee.ru*

Received June 24, 2004

Abstract—The crystals of $M_{1-x}R_xF_{2+x}$ (where M = Ca, Ba, Cd and R is a rare earth element, Ga, or In) are susceptible to phase separation on a nanometer scale (nanostructurization), which determines to a considerable degree the properties of these materials. The patterns of electron diffraction from such nanostructured crystals exhibit reflections corresponding to unknown structural features, but these reflections may completely disappear when the sample is tilted within <1°. It is shown that suppression of the nonmatrix reflections is related to peculiarities of the electron diffraction from such objects rather than to any structural features. © *2004 MAIK "Nauka/Interperiodica".*

Calcium fluoride (CaF_2) is the most important material for far-UV range optics. However, the mechanism of optical absorption in this spectral range for CaF_2 crystals is still incompletely clear [1]. Fluorides of the $M_{1-x}R_xF_{2+x}$ system, where M = Ca, Ba, Cd and R is a rare earth element, Ga, or In, are promising materials for many applications. For example, $Cd_{1-x}In_xF_{2+x}$ has no competitors as a medium for three-dimensional holography [1].

The ratio of cations and anions in $M_{1-x}R_xF_{2+x}$ is not equal to the ratio of allowed positions in the cationic and anionic sublattices. The structure of these ionic crystals contains, besides ions of the component elements, a certain amount of point defects [1]. Interactions in the subsystems of defects and components lead to the phenomenon of composition-defect separation [1–3] over a ~10 nm scale and the formation of defect regions with an unknown structure, one that is defective with respect to the matrix structure. At the same time, the lattices of the matrix and these defect regions have close parameters and exhibit coherent matching. Such crystal structures are referred to as nanostructured [1–3]. At least a part of MF_2 may exist in the form of a partly disordered phase of the $MF_{2-\delta}F'_\delta$ type, where F and F' refer to fluorine ions localized at the regular positions (1/4, 1/4, 1/4) and in interstitials, respectively, and δ is the fraction of interstitial fluorine ions [1], which may also account for nanostructurization.

In electron diffraction patterns, the defect regions are manifested by the characteristic systems of reflections, which are absent in the projections corresponding precisely to the [001], [011], and [111] directions (referred to below as exact high-symmetry projections, or simply exact projections) but appear upon deviations from these directions within ≤1° [4]. The electron diffraction patterns with two or more subsystems of reflections (composite diffraction patterns, CDPs) correspond to heterophase objects [5]. In particular, the electron diffraction patterns of twinned crystals also exhibit different subsystems of reflections [5]. Within the framework of the kinematic approach, suppression of the nonmatrix reflections during variation of the inclination axes is explained by deviations of the reflection sphere from the corresponding planes of the reciprocal lattice [5]. An exact projection in the matrix lattice may not correspond to the reflecting position for the lattice of inclusions as a result of mismatch between these lattices [5]. For an object with twins in one projection (e.g., [011]), the reflections of some twins are localized in the projection plane, while those of the other twins (e.g., [111]) fall completely within the twinned Laue diffraction zones [5]. The reflections from these Laue zones appear on the diffraction patterns for deviations within ~1°–4° from the exact high-symmetry directions, but disappear on the exact projections [5]. Elucidation of the nature (twin versus defect region) of the objects responsible for nonmatrix reflections is a task of primary importance in electron diffraction. The possibility of misorientation between the crystal lattices of the matrix and defect regions is also of fundamental importance for explaining the phenomenon of nanostructurization [1], which requires elucidating factors accounting for the suppression of nonmatrix reflections.

In this context, we have performed an electron-microscopic investigation of the commercial crystals of CaF_2 and the single crystals of $Ba_{0.75}La_{0.25}F_{2.25}$ and $Ba_{0.69}La_{0.31}F_{2.31}$ grown using the Bridgman method.

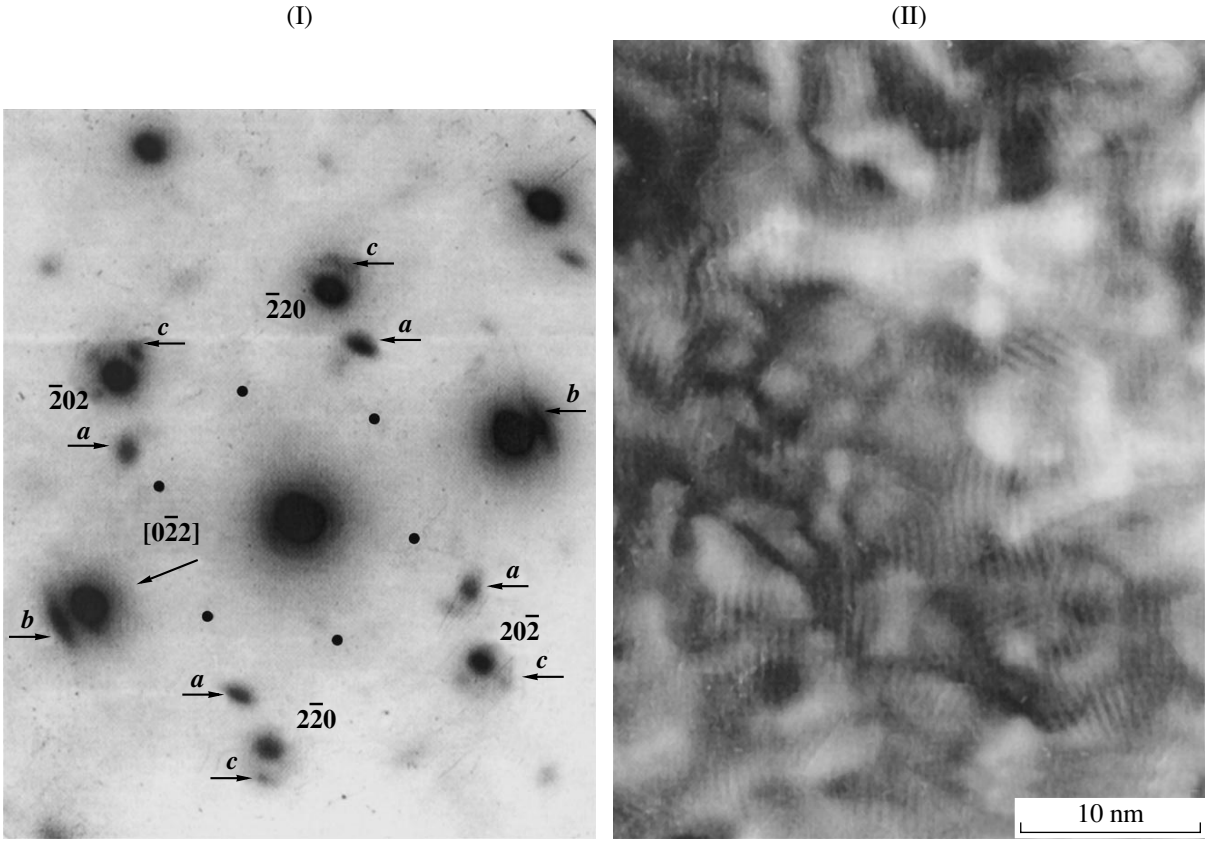

Fig. 1. (I) Electron diffraction pattern and the corresponding electron micrograph of a CaF_2 crystal in the projection deviating from the $[111]_m$ projection by ≈1° rotation about the $[0\bar{1}1]_m$ axis. Matrix reflections are provided with indexes; arrows indicate reflections from defect regions: (*a*) 002_d type, which disappears in the exact projection; (*b*) 022_d type, whose traces are retained; (*c*) 022_d type with different orientation. Points indicate the positions where twin reflection must occur. (II) Electron-microscopic image with a moire contrast.

The crystals were studied in the initial state and upon annealing at 1173 K in a fluorine-containing atmosphere [1, 2]. The samples were prepared by cleavage; the cleaved sections exhibited transparent regions with a width of ≈0.5 μm at the edge. The measurements were performed with a Philips CM-30 electron microscope.

The difference between the radii of Ba^{2+} and La^{3+} ions is much greater than, for example, that between the radii of Cd^{2+} and In^{3+} ions. This must lead to a significant difference between the lattice parameters of the matrix and defect regions and should facilitate the observation of diffraction reflections from the latter regions. Since the amplitudes of electron scattering for Ba and La atoms are virtually equal, it is possible to exclude from consideration the effects related to differences in the atomic scattering amplitudes. The results obtained for the as-grown and annealed crystals have proved to be identical.

The CDPs of CaF_2 observed for an 0.5°–1° deviation from the exact projections $[011]_m$, $[111]_m$, and $[112]_m$ exhibited reflections from the fluorite matrix with $a \approx 0.545$ nm and from the defect regions (Fig. 1(I)). For CaF_2, the reflections indexed as 002_d (here and below, the subscripts "m" and "d" refer to the matrix and defect regions, respectively) formed a rectangle. The form of the network of reflections cannot be explained by different inclinations of the twinning planes, since it is the same in the exact projection. Therefore, despite the fact that the reflections from defect regions are close to those from twins, these reflections represent inclusions of the second phase with a slightly distorted cubic lattice. With neglect of the distortion, the ratios of the lattice parameters of the matrix and defect regions are as follows: $a_d/a_m \approx \sqrt{3}/2$ for $\{111\}_m \parallel \{001\}_d$ and $\langle 211\rangle_m \parallel \langle 110\rangle_d$, $d_{002m} = d_{111m}$, $3d_{111m} = 4d_{002d}$, $3d_{211m} = 2d_{110d}$, $3d_{221m} = 2d_{111d}$, $13d_{110m} \approx 5d_{110d}$ (the latter value is determined to within 0.07%). This provides for a three-dimensional matching of the lattices with virtually zero misfit stresses.

On the passage to the exact projections $[011]_m$, $[111]_m$, and $[112]_m$, the intensity of reflections from defect regions decreased, although the CDPs of the exact projections strictly corresponded to the same volumes of the crystal as the CDPs of inclined projections.

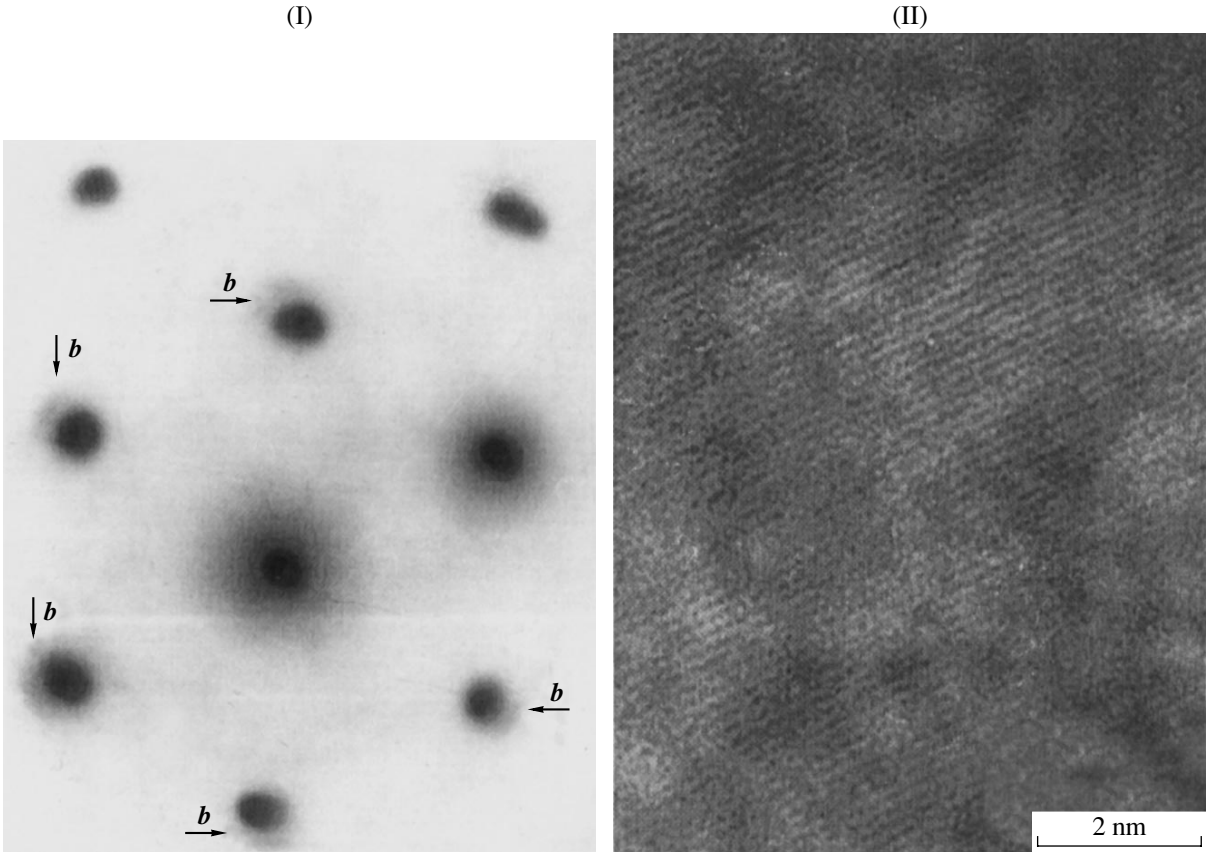

Fig. 2. (I) Electron diffraction pattern and the corresponding electron micrograph of the same volume of CaF_2 crystal as in Fig. 1, in the exact $[111]_m$ projection. The intensities of matrix reflections are leveled; arrows indicate reflections of the 022_d type near the 022_m matrix reflections. (II) electron-microscopic image showing one-dimensional oscillations in intensity, but no evidence of the moire contrast.

The drop in the intensity of reflections from defect regions increased with the matrix thickness, and an almost complete suppression was observed for sufficiently thick objects (Fig. 2(I)). The 002_d reflections were more sensitive with respect to sample tilt than the 022_d reflections localized near the 022_m reflections. Traces of the 022_d reflections were observed even on the CDPs of relatively thick regions (Fig. 2(I)). The appearance and disappearance of reflections was observed upon every tilt and depended neither on the axis about which the rotation was performed nor on the direction of deviation (for deviations in the opposite directions, a change in the CDP was observed for the same angles of rotation).

The CDP changes observed upon variation of the inclination angle cannot be explained by deviation of the defect region lattice from the reflecting position. Figure 2(I) shows that traces of the $0\bar{2}2_d$ type reflections are present near at least five $0\bar{2}2_m$ reflections. The passage from the CDP in Fig 1(II) to that in Fig. 1(I) was observed upon rotation about the $0\bar{2}2_m$ axis (on which the $0\bar{2}2_d$ and $02\bar{2}_d$ reflection are situated, which cannot leave their reflection spheres as a result of this rotation).

In order to reveal the dependence of the obtained micrographs on the character of CDPs, we used thicker objects, for which the reflections from defect regions in the exact projections were completely suppressed. Figures 1(II) and 2(II) show the CPDs from the same volume of a CaF_2 sample. The former pattern reveals 5- to 10-nm defect regions with a moire contrast but exhibits no interference bands with a period corresponding to the interplanar spacing, whereas the latter pattern shows no defect regions but displays bands with a period corresponding to the $[111]_m$ interplanar distance.

In the CDPs from $Ba_{0.75}La_{0.25}F_{2.25}$, and $Ba_{0.69}La_{0.31}F_{2.31}$, the projections deviating by ≈0.8° from the exact high-symmetry $[011]_m$, $[111]_m$, and $[112]_m$ projections exhibited reflections from a fluorite matrix lattice with $a \approx 0.61$ nm and a network of nonmatrix reflections. The geometry of these networks for various projections, as well as their changes from one

to another projection, unambiguously indicated that the observed nonmatrix reflections belonged to twins.

On the passage from inclined projections to the exact $[111]_m$ projection, the nonmatrix reflections were suppressed in accordance with the rules of suppression of twin reflections [5]. The $[011]_m$ plane features reflections of the families of twins corresponding to the $[1\bar{1}1]$ and $[\bar{1}\bar{1}1)$ twinning planes, which do not leave the reflection sphere upon going to the exact projection and, hence, must not be suppressed. However, on the passage to the exact projection $[011]_m$, the reflections of twins corresponding to the $[0\bar{1}1]_m$ and $[1\bar{1}1]_m$ twinning planes (observed in the inclined projections) were suppressed.

The observed suppression of twin reflections for the $[011]_m$ projection and the reflections from defect regions for the $[111]_m$ projection cannot be explained within the framework of the kinematic approach. Suppression of the latter reflections can be, in principle, explained by structural peculiarities of the nanostructured objects. However, the lattice of twins in the cubic crystals differs from the matrix lattice only by rotation. The same laws governing the suppression of reflections from twins and defect regions indicate that this effect is not related to peculiarities of the atomic structure of these defect regions.

Apparently, the phenomenon of suppression of the nonmatrix reflections has the same nature as a decrease in the sensitivity with respect to the crystal structure defects observed for the electron diffraction patterns obtained using converging beams corresponding to exact projections [6]. The latter phenomenon has a dynamic nature. In high-symmetry projections, the Bloch waves exhibiting anomalous absorption are predominantly excited, which leads to a decrease in the relative intensity of diffraction peaks with respect to background [5].

For BaF_2, the suppression of nonmatrix reflections was not observed [7], probably because of considerable differences between the lattices of inclusions and the matrix and large dimensions of inclusions. The angle of deviation from the exact projection for which the appearance and disappearance of reflections from defect regions are observed decreases with the object thickness. For the $[011]_m$ projection, only the reflections from defect regions with $|g_{hkl}|_d \leq |g_{220}|_d$ were observed, but the $[111]_m$ projection also showed the 400_d reflections, while the $[255]_m$ projection and the $(011)_d$ plane exhibited the $31\bar{1}_d$ reflections. This result indicates that suppression of the reflections from defect regions depends on the occupation of the plane of the reciprocal lattice of the matrix by low-index reflections.

The fact that the effect is less pronounced in CaF_2 is probably related to a lower anomalous absorption in CaF_2, since the degree of suppression in this crystal increases with the object thickness. This behavior is consistent with the hypothesis on the dynamic nature of the suppression effect.

Neither the nature of nor the reasons for the formation of defect regions in CaF_2 are established (these regions probably correspond to $CaF_{2-\delta}F'_\delta$, but the nanostructurization may be one of the factors responsible for the increase in optical absorption in the far-UV spectral range. The phenomenon of suppression of the reflections from defect regions is not related to peculiarities in the atomic structure of these regions and leads to difficulties in the interpretation of the results of electron-microscopic investigation of nanostructured objects. Reliable information about the structure of defect regions (especially for the [001], [011], and [111] projections) can be extracted from a comparative analysis of the results obtained for the exact and deviated projections. In development of the technology of CaF_2 crystals for UV optics, the crystal structure has to be monitored by means of electron-microscopic techniques.

Acknowledgments. The authors are grateful to N.I. Borgard (Moscow State Institute of Electronic Engineering), L.D. Marx (North-western University, Illinois), and A.S. Avilov (Moscow State Institute of Electronic Engineering) for fruitful discussions.

This study was supported by the Russian Foundation for Basic Research, project no. 01-03-33000.

REFERENCES

1. B. P. Sobolev, *The Rare Earth Trifluorides* (Institut d'Estudis Catalans, Barselona, 2001).
2. H. Gleiter, Acta Mater. **48**, 1 (2000).
3. B. P. Sobolev, A. N. Golubev, E. A. Krivandina, *et al.*, Kristallografiya **47**, 2237 (2002) [Crystallogr. Rep. **47**, 201 (2002)].
4. S. K. Maksimov, A. S. Avilov, B. P. Sobolev, and P. Herrero, in *Proceedings of the 5th International Conference "Single Crystal Growth and Heat & Mass Transfer," Obninsk, 2003*, Vol. 2, pp. 379–388.
5. *Electron Microscopy of Thin Crystals*, Ed. by P. B. Hirsch, A. Howie, R. B. Nicholson, D. W. Pashley, and M. J. Whelan (Plenum Press, New York, 1965).
6. Kenji Tsuda, in *Proceedings of the European Summer School on Electron Crystallography, Moscow, 2003* (Shubnikov Institute of Crystallography, Moscow, 2003), pp. 70–80.
7. S. K. Maksimov, A. S. Avilov, B. P. Sobolev, and P. Errero, Zavod. Lab. **69** (10), 24 (2003).

Translated by P. Pozdeev

Technical Physics Letters, Vol. 30, No. 12, 2004, pp. 983–986. Translated from Pis'ma v Zhurnal Tekhnicheskoĭ Fiziki, Vol. 30, No. 23, 2004, pp. 24–31.

Theory of Magnetoelectric Effect in Ferromagnetic–Piezoelectric Bilayer Structures

D. A. Filippov

Novgorod State University, Velikiĭ Novgorod, Russia

e-mail: fdma@novsu.ac.ru

Received June 15, 2004

Abstract—A theory of the magnetoelectric (ME) effect in a ferromagnetic-piezoelectric bilayer structure is presented. An expression for the ME voltage coefficient in terms of the parameters of the ferromagnetic and piezoelectric phases is obtained, and the dependence of this coefficient on the frequency and the ratio of the ferromagnetic and piezoelectric layer thicknesses is analyzed. The results of numerical calculations of the ME voltage coefficient for a permendur–PZT bilayer system are in satisfactory agreement with experimental data. *© 2004 MAIK "Nauka/Interperiodica".*

Magnetoelectric (ME) composites consist of the mechanically interacting layers of magnetostrictive and piezoelectric components. This interaction between the magnetic and piezoelectric components gives rise to the magnetoelectric (ME) effect observed in such materials. Previously [1–3], a theory of the ME effect was developed based on the method of effective parameters and was compared to the experimental results for multilayer composites based on nickel ferrite and lead zirconate titanate (PZT). Since the ME voltage coefficient is proportional to the product of the piezoelectric and piezomagnetic coefficients, replacing the ferrite with a ferromagnet possessing a large magnetostriction constant provides for a large magnitude of the ME effect.

Recently, the results of an experimental investigation of the disk-shaped permendur–PZT–permendur plane-parallel trilayer structures were reported in [4]. In this case, the ME composite can no longer be considered a homogeneous medium, and the aforementioned model is inapplicable. A theory of the ME effect in a hybrid structure of a thin plate comprising serially connected ferrite and piezoelectric regions was developed in [5].

This paper presents a theory of the ME effect in heterogeneous disk-shaped structures consisting of parallel layers of magnetic and piezoelectric materials.

The theory is developed for a model (Fig. 1) representing the disk of a bilayer composite material comprising plane-parallel ferromagnetic and piezoelectric layers in mechanical contact, with metal electrodes of a negligibly small thickness deposited onto the external surfaces of both layers. Let the sample be polarized along the normal to the planes (i.e., in the direction parallel to the Z axis). For the longitudinal ME effect, the constant (bias) and alternating magnetic fields are also perpendicular to the contact planes, while for the transverse (lateral) ME effect, these magnetic fields are oriented in the plane parallel to the contacts and are parallel to the X axis.

The alternating magnetic field with frequency ω induces oscillations in the ferromagnetic layer that propagate both in plane and in depth of the sample and penetrate via the mechanical contact into the piezoelectric layer. In what follows, consideration will be restricted to the volume oscillations propagating in plane of the sample. Taking into account that the disk is thin and bears metal contacts on the top and bottom surfaces, the only nonzero components of the stress tensor and the electric field strength tensor are T_1, T_2, and E_3. Then, equations for the strain tensor ${}^mS_i$ in the magnetic layer and for the strain tensor ${}^pS_i$ and the electric induc-

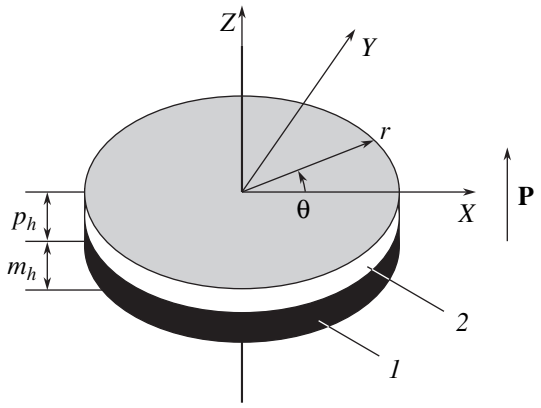

Fig. 1. Schematic diagram of the composite structure consisting of (*1*) ferromagnetic and (*2*) piezoelectric layers (see the text for explanations).

1063-7850/04/3012-0983$26.00 © 2004 MAIK "Nauka/Interperiodica"

tion D_i in the piezoelectric layer in the case of a transverse orientation of the field can be written as

$$ {}^{m}S_1 = {}^{m}s_{11}{}^{m}T_1 + {}^{m}s_{12}{}^{m}T_2 + q_{11}H_1, \quad (1) $$

$$ {}^{m}S_2 = {}^{m}s_{12}{}^{m}T_1 + {}^{m}s_{11}{}^{m}T_2 + q_{12}H_1, \quad (2) $$

$$ {}^{p}S_1 = {}^{p}s_{11}{}^{p}T_1 + {}^{p}s_{12}{}^{p}T_2 + d_{31}E_3, \quad (3) $$

$$ {}^{p}S_2 = {}^{p}s_{11}{}^{p}T_1 + {}^{p}s_{12}{}^{p}T_2 + d_{31}E_3, \quad (4) $$

$$ D_3 = {}^{p}\varepsilon_{33}E_3 + d_{31}({}^{p}T_1 + {}^{p}T_2), \quad (5) $$

where ${}^{m}s_{ij}$ and ${}^{p}s_{ij}$ are the components of the compliance tensors of the magnetic and piezoelectric materials, respectively; ${}^{p}\varepsilon_{33}$ are the components of the permittivity tensor; and d_{ij} and q_{ij} are the piezoelectric and piezomagnetic coefficients, respectively. For the longitudinal orientation of the electric and magnetic fields, the terms $q_{11}H_1$ in Eq. (1) and $q_{12}H_1$ in Eq. (2) have to be replaced by $q_{31}H_3$.

Taking into account the symmetry of the problem and passing to a cylindrical coordinate system using well-known relations [6], we obtain expressions for the components of the strain tensor:

$$ {}^{m}S_{rr} = {}^{m}s_{11}{}^{m}T_{rr} + {}^{m}s_{12}{}^{m}T_{\theta\theta} + (q_{11}\cos^2(\theta) + q_{12}\sin^2(\theta))H_1, \quad (6) $$

$$ {}^{m}S_{\theta\theta} = {}^{m}s_{12}{}^{m}T_{rr} + {}^{m}s_{11}{}^{m}T_{\theta\theta} + (q_{11}\sin^2(\theta) + q_{12}\cos^2(\theta))H_1, \quad (7) $$

$$ {}^{p}S_{rr} = {}^{p}s_{11}{}^{p}T_{rr} + {}^{p}s_{12}{}^{p}T_{\theta\theta} + d_{31}E_3, \quad (8) $$

$$ {}^{p}S_{\theta\theta} = {}^{p}s_{12}{}^{p}T_{rr} + {}^{p}s_{11}{}^{p}T_{\theta\theta} + d_{31}F_3. \quad (9) $$

The equation of motion for the radial oscillations of the disk appear as

$$ \frac{\partial T_{rr}}{\partial r} + \frac{1}{r}(T_{rr} - T_{\theta\theta}) + \rho\omega^2 u_r = 0, \quad (10) $$

where ρ is the density of the material.

Expressing the stress tensor components T_{rr} and $T_{\theta\theta}$ in terms of relations (6) and (7) and substituting these expressions into Eq. (10), we obtain a differential equation for the radial component ${}^{m}u_r$ of the displacement vector in the magnetic medium:

$$ \frac{\partial^{2m}u_r}{\partial r^2} + \frac{1}{r}\frac{\partial^{m}u_r}{\partial r} - \frac{{}^{m}u_r}{r^2} + {}^{m}k^{2m}u_r - \frac{D(\theta)}{r} = 0, \quad (11) $$

where $D(\theta) = (q_{11} - q_{12})(1 - {}^{m}\nu)(\cos^2(\theta) - \sin^2(\theta))H_1$, ${}^{m}k = \sqrt{{}^{m}\rho\,{}^{m}s_{11}(1 - {}^{m}\nu)}\,\omega$, ${}^{m}\rho$ is the density of the magnetic medium, and ${}^{m}\nu = {}^{m}s_{12}/{}^{m}s_{11}$ is the Poisson coefficient of this medium.

According to [3], a solution of Eq. (11) can be found in the following form:

$$ {}^{m}u_r = c_1 J_1({}^{m}kr) + c_2 Y_1({}^{m}kr) + D(\theta)/({}^{m}k^2 r), \quad (12) $$

where $J_1({}^{m}kr)$ and $Y_1({}^{m}kr)$ are the Bessel functions of the first and second kind, respectively, and c_1 and c_2 are the integration constants determined from the boundary conditions.

Using the condition that the displacement vector at the disk center is zero and taking into account the properties of the Bessel function of the second kind for small values of the argument, we obtain an expression for the integration constant c_2:

$$ c_2 = \pi D(\theta)/(2\,{}^{m}k). \quad (13) $$

For the free side surface of the disk, the condition of equilibrium for mechanical stresses at the boundary yields

$$ {}^{m}h\,{}^{m}T_{rr}(R) + {}^{p}h\,{}^{p}T_{rr}(R) = 0. \quad (14) $$

Oscillations of the ferromagnet displacement ${}^{m}u_r(r)$ excited by the magnetic field are transmitted to the piezoelectric layer via the interface. Since the mechanical contact at the interface in the general case is nonideal, the radial components of the displacement vector in the magnetic and piezoelectric layers are related as

$$ {}^{p}u_r(r) = \beta\,{}^{m}u_r(r), \quad (15) $$

where β is a parameter describing mechanical coupling between the ferromagnetic and piezoelectric layers ($0 < \beta < 1$). Using relation (15) and boundary condition (14), we obtain an expression for the integration constant c_1:

$$ c_1 = \frac{R}{(\gamma + \beta)\Delta}((1 - {}^{p}\nu)d_{31}E_3 + \gamma((\cos^2(\theta) + {}^{m}\nu\sin^2(\theta))q_{11} + (\sin^2(\theta) + {}^{m}\nu\cos^2(\theta))q_{12})H_1 - D(\theta)(0.5\pi(\gamma + \beta) \times (Y_0(\kappa) - (1 - {}^{m}\nu)Y_1(\kappa)/\kappa) - (1 - {}^{m}\nu)/\kappa^2)), \quad (16) $$

where $\Delta = \kappa J_0(\kappa) - (1 - {}^{m}\nu)J_1(\kappa)$, $\kappa = {}^{m}kR$, $\gamma = ({}^{m}h/{}^{p}h)({}^{p}s_{11}(1 - {}^{p}\nu^2))/({}^{m}s_{11}(1 - {}^{m}\nu^2))$, and ${}^{p}\nu = {}^{p}s_{12}/{}^{p}s_{11}$ is the Poisson coefficient for the piezoelectric medium.

The normal component of the vector of electric induction in the piezoelectric layer is determined from Eq. (5). Substituting solution (12) into expressions for the stress tensor and taking into account relation (15), we obtain an equation for the normal component of the of electric induction vector,

$$ D_3 = {}^{p}\varepsilon_{33}E_3 - \frac{2d_{31}^2}{{}^{p}s_{11}(1 - {}^{p}\nu)}E_3 + \frac{d_{31}\beta\kappa}{{}^{p}s_{11}(1 - {}^{p}\nu)R}(c_1 J_0({}^{m}kr) + c_2 Y_0({}^{m}kr)). \quad (17) $$

The strength of the electric field induced in the strained piezoelectric medium can be determined using Eq. (17) with the open-circuit condition $\int_0^R r\,dr \int_0^{2\pi} d\theta D_3 = 0$. Performing the integration, we obtain an expression for the electric field strength E_3 in the piezoelectric layer:

$$E_3 = -\frac{\gamma\beta}{(\gamma+\beta)}\frac{d_{31}(q_{11}+q_{12})(1+{}^m\nu)J_1(\kappa)}{{}^ps_{11}(1-{}^p\nu)\Delta_a}H_1, \quad (18)$$

where $\Delta_a = \Delta + K_p^2(1+{}^p\nu)J_1(\kappa)\beta/(\gamma+\beta)$ and $K_p^2 = 2d_{31}^2/({}^p\varepsilon_{33}{}^ps_{11}(1-{}^p\nu))$ is the square of the electromechanical coupling coefficient for the planar oscillations.

The ME voltage coefficient for the bilayer structure is defined as

$$\alpha_E = E_{\text{av}}/H, \quad (19)$$

where $E_{\text{av}} = U({}^mh + {}^ph)$ is the average value of the electric field strength in the disk and U is the potential difference between electrodes. Since the resistance of the piezoelectric layer is much greater than that of the ferromagnet, we may assume that the applied voltage drops entirely in the former layer. Then, the ME coefficient for the transverse orientation of the electric and magnetic fields is given by the expression

$$\alpha_{E,T} = -\frac{\gamma\beta}{(\gamma+\beta)}\frac{d_{31}(q_{11}+q_{12})(1+{}^m\nu)J_1(\kappa)}{{}^ps_{11}(1-{}^p\nu)\Delta_a}\frac{{}^ph}{({}^mh+{}^ph)}. \quad (20)$$

For the longitudinal orientation of the electric and magnetic fields (i.e., for the sample polarized along the Z axis), the sum $q_{11}+q_{12}$ is replaced by $2q_{31}$. Under the action of demagnetizing fields, the value of q_{31} is usually smaller than that of q_{11}. For this reason, the ME effect for the longitudinal polarization is usually one order of magnitude lower than the effect for the transverse polarization.

Expression (20) indicates that the ME coefficient must exhibit a resonance growth for the frequencies corresponding to $\Delta_a = 0$. The level of losses in the structure under consideration can be taken into account by introducing a parameter characterizing the damping of oscillations. For this purpose, it is convenient to represent the circular frequency as the complex quantity $\omega = \omega' + i\chi$, where χ is the damping coefficient [7].

Figure 2 presents the frequency dependence of the ME voltage coefficient calculated using formula (20) for a permendur–PZT bilayer structure with the following parameters: magnetic layer, ${}^ms_{11} = 5.5\times10^{-12}$ m^2/N, $q_{11} = 63.75\times10^{-10}$ m/A, ${}^mh = 0.36$ mm; piezoelectric layer, ${}^ps_{11} = 15\times10^{-12}$ m^2/N, $d_{31} = -175\times10^{-12}$ m/V,

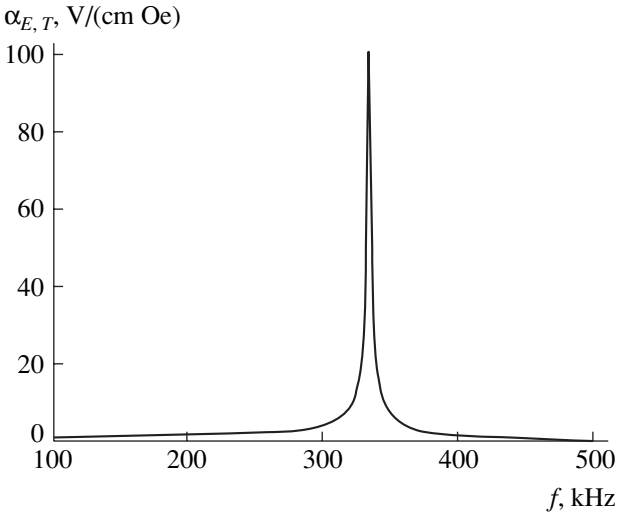

Fig. 2. Frequency dependence of the ME voltage coefficient calculated for a permendur–PZT bilayer structure.

${}^p\varepsilon_{33}/\varepsilon_0 = 1750$, ${}^ph = 0.36$ mm; damping coefficient, $\chi = 10000$ s^{-1}; disk radius, $R = 9$ mm; coupling coefficient, $\beta = 0.9$. As can be seen from Fig. 2, the bilayer structure with these parameters exhibits a resonance increase in the ME coefficient. The maximum value of this coefficient agrees in order of magnitude with the experimental value reported in [4]. In the low-frequency range, the ME voltage coefficient is virtually independent of the frequency and can be approximately described by the expression

$$\alpha_{E,T}^{\text{LF}} = -\frac{\gamma\beta}{(\gamma+\beta)}\times\frac{d_{31}(q_{11}+q_{12})}{{}^ps_{11}(1-{}^p\nu)(1+\beta K_p^2(1+{}^p\nu)/((\gamma+\beta)(1+{}^m\nu)))}\times\frac{{}^ph}{({}^mh+{}^ph)}. \quad (21)$$

Formula (20) shows that the ME voltage coefficient depends on the parameters of the ferromagnetic and piezoelectric materials, the coupling coefficient, and the ratio of thicknesses of the ferromagnetic and piezoelectric layers. For small values of the coupling coefficient, the ME effect is proportional to this quantity, but the dependence is less pronounced when β is close to unity. According to expressions (20) and (21), the maximum value of the ME voltage coefficient is achieved for the following ratio of thicknesses of the ferromagnetic and piezoelectric layers:

$${}^mh/{}^ph = (\beta{}^ms_{11}(1-{}^m\nu))/({}^ps_{11}(1-{}^p\nu)). \quad (22)$$

In the experiments reported in [4], the maximum value of the ME voltage coefficient was observed for a

piezoelectric layer thickness of ${}^{p}h$ = 0.6 mm and a ferromagnetic layer thickness of ${}^{m}h$ = 0.36 mm. Substituting the known values of compliances for permendur and PZT, we obtain good agreement between theory and experiment for a coupling coefficient of $\beta = 0.9$.

In conclusion, the mechanical interaction between magnetostrictive and piezoelectric subsystems leads to the appearance of the ME effect in stratified ferromagnetic–piezoelectric composites. The maximum value of the ME voltage coefficient is observed for a certain ratio between the thicknesses of the ferromagnetic and piezoelectric layers, which depends on the coupling coefficient between layers and on the ratio of the compliance moduli of the ferromagnetic and piezoelectric media.

Acknowledgments. This study was supported in part by the Ministry of Education of the Russian Federation (project no. E02-3.4-278) and the program "Universities of Russia" (project no. UR 01.01.007).

REFERENCES

1. M. I. Bichurin, D. A. Filippov, V. M. Petrov, *et al.*, Phys. Rev. B **68**, 132408 (2003).
2. D. A. Filippov, M. I. Bichurin, V. M. Petrov, *et al.*, Pis'ma Zh. Tekh. Fiz. **30** (1), 15 (2004) [Tech. Phys. Lett. **30**, 6 (2004)].
3. D. A. Filippov, M. I. Bichurin, V. M. Petrov, *et al.*, Fiz. Tverd. Tela (St. Petersburg) **46**, 1621 (2004) [Phys. Solid State **46**, 1674 (2004)].
4. V. Laletsin, N. Padubnaya, G. Srinivasan, and C. P. De Vreugd, Appl. Phys. A **78**, 33 (2004).
5. D. A. Filippov, Pis'ma Zh. Tekh. Fiz. **30** (9), 6 (2004) [Tech. Phys. Lett. **30**, 351 (2004)].
6. W. P. Mason, Phys. Rev. **74**, 1134 (1948).
7. R. Truell, C. Elbaum, and B. B. Chick, *Ultrasonic Methods in Solid State Physics* (Academic Press, New York, 1969).

Translated by P. Pozdeev

Technical Physics Letters, Vol. 30, No. 12, 2004, pp. 987–988. Translated from Pis'ma v Zhurnal Tekhnicheskoĭ Fiziki, Vol. 30, No. 23, 2004, pp. 32–35.

Microscopic X-ray Sources Imaged Using High-Resolution Enlargement Kumakhov Optics

A. Yu. Romanov

Institute for Roentgen Optics, Moscow, Russia

e-mail: androm2@yandex.ru

Received June 10, 2004

Abstract—A substantially new direction in X-ray microscopy is developed. X-ray images of a microscopic X-ray source representing a focal spot of a microfocus X-ray tube have been obtained with a spatial resolution on the level of 1 μm. This possibility is provided by a cone-shaped polycapillary high-resolution Kumakhov optical structure. © *2004 MAIK "Nauka/Interperiodica".*

The problem of imaging objects emitting in the X-ray range is still of considerable importance in view of the continuous development of both traditional X-ray sources such as microfocus X-ray tubes and relatively new devices such as laser plasma sources. Previously [1, 2], the focal spot size of an X-ray tube was determined using an image obtained with the aid of a cylindrical Kumakhov X-ray optical structure. However, the accuracy provided by such imaging systems is frequently insufficient for determining the dimensions of focal spots of modern microfocus X-ray tubes, since the error introduced by the usual polycapillary structure is comparable with the anode spot size that is to be determined. Moreover, in the case of micron focal spots, the size of the image of this spot at the exit of the polycapillary column can be smaller than the limiting resolution of a detector system: modern commercial X-ray imaging systems have a resolution on the order of 5–6 μm, whereas the focal spots of microfocus X-ray tubes can be as small as a few microns.

In this situation, it expedient to use the wide possibilities offered by Kumakhov optics in application to the X-ray images [2–7]. Using a high-resolution imaging cone-shaped polycapillary of Kumakhov optical structure, it is possible to lift restrictions related to the detector resolution.

The proposed method is essentially as follows (see Fig. 1). A polycapillary structure with the shape of a truncated cone is brought sufficiently close (at a distance shorter than the focal length) to the X-ray anode, and a detector system is placed at the exit of this capillary structure. The focal length is defined as the point of convergence of the generating lines of the cone. As the detector system for a rapid evaluation of the source size, it is most expedient to use a conventional X-ray imager. The size of the focal spot is determined from the image size upon preliminary calibration of the system.

In the proposed method, the role of the cone-shaped structure is to form an enlarged image of the source. The entrance diameter of the capillary used in the polycapillary structure (i.e., the capillary edge facing the focal spot) must be much smaller than the anode spot size. The exit diameter of the capillary (at the output of the Kumakhov lens) must correspond to the resolution of the imager. In such systems, the capillary optics transfers information about the object size to the detector at an accuracy corresponding to 2–3 entrance diameters of the capillary. Therefore, reaching a resolution of 1 μm requires that the capillary entrance diameter not exceed ~0.5 μm. Naturally, the capillary diameter variation from entrance to exit should be thoroughly controlled so as to avoid distortion of the information transferred. The spatial resolution in the proposed scheme is increased both due to a decrease in the entrance size of the channel and to the cone shape, which provides an increase in the image size.

Using the proposed approach, it is possible to increase the accuracy of spot-size determination using modern X-ray imaging systems up to a level of 1 μm. A disadvantage of this method (as compared to the capillary column technique [1, 2]) is the somewhat more complicated procedure of the adjustment of the cone

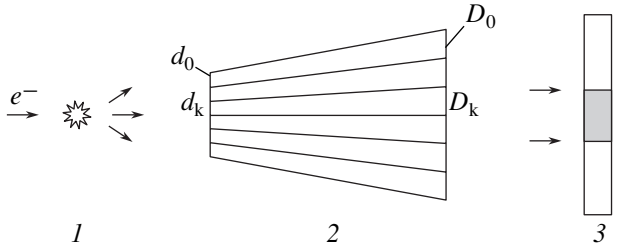

Fig. 1. Schematic diagram of the experimental arrangement: (*1*) focal spot of the X-ray tube; (*2*) cone-shaped polycapillary structure; (*3*) X-ray detector.

1063-7850/04/3012-0987$26.00 © 2004 MAIK "Nauka/Interperiodica"

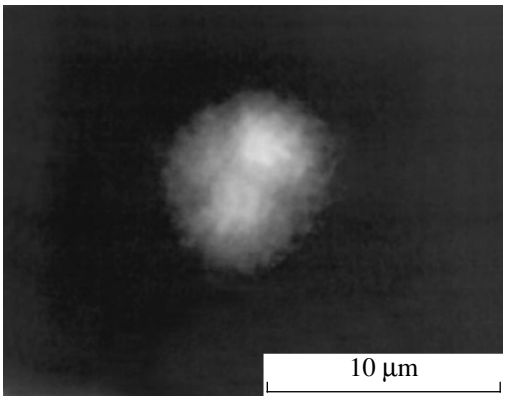

Fig. 2. Typical image of the focal spot of a microfocus X-ray tube obtained using a cone-shaped Kumakhov semilens (the spatial scale is reduced to the anode surface).

relative to the X-ray tube. Additional distortions can be introduced by an imperfectly regular polycapillary structure, which is related to technological difficulties encountered in manufacturing capillaries with decreasing channel size.

The proposed method was implemented using a cone-shaped polycapillary structure (Kumakhov cone semilens) comprised of an assembly of cone-shaped capillaries (hollow glass tubes) with a small entrance diameter that gradually increased toward the exit. The entire assembly had an input diameter of $d_0 = 0.3$ mm and an output diameter of $D_0 = 4.5$ mm (Fig. 1). The capillary channel diameter was approximately 1000 times smaller ($d_k = 0.3$ μm at the entrance and $D_k = 4.5$ μm at the exit).

The polycapillary structure was mounted in a special holder capable of moving in three mutually perpendicular directions, which allowed the collimator to be precisely adjusted relative to the focal spot of the X-ray tube. The minimum step of adjustment was 0.1 μm.

The experiments were performed with an X-ray imager comprising a scintillation screen, a light guide, an electrooptical converter, and a CCD camera whose signal was digitized and fed to a computer for storage and processing. The total resolution of the X-ray imager in the phosphor-coated plane was ~5 μm. A microfocus X-ray tube used in these experiments also had a minimum focal spot size of 5 μm.

Figure 2 shows an example of the typical X-ray image of the focal spot of the microfocus X-ray tube. The image, with a resolution of about 1 μm, was obtained using the method described above. An analysis of this image allows the X-ray tube anode spot size to be determined. The image exhibits dark regions related to the walls of the polycapillary structure. However, these features do not introduce significant image distortions capable of hindering determination of the focal spot size.

Thus, using a cone-shaped Kumakhov semilens, it is possible to obtain images of the focal spots of X-ray tubes with a micron resolution. The proposed method provides high-precision determination of the effective focal spot size of a microfocus X-ray tube.

Acknowledgments. The authors are grateful to V.N. Chernik for fruitful discussions that greatly contributed to this study.

REFERENCES

1. V. A. Arkadiev and A. A. Bzhaumikhov, Proc. SPIE **2515**, 514 (1995).
2. A. Yu. Romanov, Izmer. Tekh., No. 7 (2004).
3. S. V. Nikitina, A. S. Scherbakov, *et al.*, Proc. SPIE **2011**, 255 (1993).
4. S. V. Nikitina, G. A. Vartaniants, *et al.*, Proc. SPIE **2278**, 210 (1994).
5. A. N. Nikitin, N. S. Ibraimov, and S. V. Nikitina, Proc. SPIE **2859**, 117 (1996).
6. A. N. Nikitin, Proc. SPIE **3115**, 117 (1997).
7. A. N. Nikitin, Proc. SPIE **3115**, 143 (1997).

Translated by P. Pozdeev

Technical Physics Letters, Vol. 30, No. 12, 2004, pp. 989–990. Translated from Pis'ma v Zhurnal Tekhnicheskoĭ Fiziki, Vol. 30, No. 23, 2004, pp. 36–39.

Thin Microwire with Negative Magnetostriction in a Zero Magnetic Field

S. A. Baranov* and M. Vazquez**

Instituto de Ciencia de Materiales, Madrid, Spain

*e-mail: * baranov@icmm.csic.es; ** mvazquez@icmm.csic.es*

Received June 10, 2004

Abstract—The effect of residual mechanical stresses on the distribution of magnetization in thin metal microwires with negative magnetostriction has been studied in a zero magnetic field. It is established that the microwire has a nonzero residual magnetization in the absence of twisting and bulging rotational modes.

Cobalt based microwires with negative magnetostriction are magnetically soft, exhibit giant magnetic impedance, and possess a domain structure that was recently proposed in [1]. Very thin microwires with a radius r_c smaller than the domain wall thickness feature domainless structures [2–5].

This Letter presents the results of a theoretical calculation of the magnetic properties of a thin ($r_c \sim 1$ μm and smaller) cast amorphous microwire with negative magnetostriction in a glass insulating shell and predicts high-frequency resonance in this material.

Let us obtain an analytical solution of the well-known Brown equation [2, 3],

$$\theta''(\rho) + 1/\rho\theta''(\rho) + [\eta/f(\rho) - 1/\rho^2] \times \sin\{2\theta(\rho)\}/2 = 0, \quad (1)$$

where $0 < \theta(\rho) < \pi/2$ is the relative magnetization of the microwire (which is equal, in the geometric representation, to the angle $\theta(\rho)$ between the axis and the magnetic moment of a cylinder modeling the wire); $\rho = r/r_c$ is the dimensionless radial coordinate (expressed in r_c units); $\rho^\circ < \rho < 1$, where $(\rho^\circ)^2 = A/[K(r_c)^2]$ ($\rho^\circ < 0.1$ has the physical sense of the relative radius of a region in the wire where the magnetization is homogeneous and directed along the cylinder axis, so that $\theta(\rho) = 0$ [4, 5]); A is the exchange interaction constant; and K is the constant of anisotropy of the microwire. Previously [5], it was demonstrated that a microwire with negative magnetostriction has $\eta = 1$ (for a wire with positive magnetostriction, $\eta = -1$, but this case is not considered here). Taking into account the results reported by Antonov *et al.* [6], we assume that the function $f(\rho)$ obeys the relation

$$1/f(\rho) = 1/(\rho^\circ)^2\{|\sigma_{\min} - \sigma_z|/\sigma_z\}, \quad (2)$$

where $\sigma_{\min} = \min\{\sigma_\rho, \sigma_\varphi\}$ (note that, in the case under consideration, the use of σ_ρ or σ_φ does not influence the form of the function). The case of neglect of the functions σ_ρ and σ_φ was considered elsewhere [4, 5].

Following [1, 7], let us adopt the following model of stress development in a cast amorphous microwire in a glass insulating shell. Electrochemical interactions provide for a strong adhesion between the external surface of the wire and the glass shell. The surface stresses exhibit relaxation on the passage from the metal surface to a certain layer of radius b. According to the physical meaning of this radius, the material at $r < b$ features only plastic relaxation, and we may assume that $b \sim \rho^\circ$. Indeed, the magnetization of a wire with negative magnetostriction under conditions of decreasing stresses must be oriented toward the axis of the cylinder.

According to [1, 7], the residual stresses in the microwire can be represented in the following form:

$$\sigma_\rho = P(1 - b^2/\rho^2) + \sigma^\circ,$$
$$\sigma_\varphi = P(1 + b^2/\rho^2) + \sigma^\circ, \quad (3)$$
$$\sigma_z = \nu(\sigma_\rho + \sigma_\varphi) \sim P + \sigma^\circ,$$

where ν is Poisson's coefficient (in the case of elastic-plastic relaxation under consideration, this quantity varies within $\nu \sim 0.3$–0.5); σ° denotes all the remaining stresses such that $\sigma^\circ < P$ [1, 7], where P is the parameter determined in [8] (this quantity is not considered here, since it is canceled). For the unknown function $1/f(\rho)$ in Eq. (1), we obtain the following asymptotic expression:

$$1/f(\rho) = \{1/(\rho^\circ)^2\}\{b^2/\rho^2\} \sim 1/\rho^2. \quad (4)$$

Taking into account this relation, we obtain the following asymptotic form of Eq. (1):

$$\theta''(\rho) + 1/\rho\theta'(\rho) = 0. \quad (5)$$

In contrast to Eq. (1), this equation is linear and can be readily integrated. A partial solution for Eq. (5) with

allowance for the appropriate boundary conditions [4–6] is as follows:

$$\theta(\rho/\rho^\circ) = C\ln|\rho/\rho^\circ|, \quad C = \pi/2\ln|1/\rho^\circ|. \tag{6}$$

Integrating expression (6) from ρ° (e.g., adopting $\rho^\circ \sim 0.1$) to $\rho^\circ \sim 1$, we obtain a relation for the relative magnetization of the microwire:

$$M/M_0 \sim 1/4(1-(\rho^\circ)^2)(1-1/\ln|1/\rho^\circ|) \sim 0.2. \tag{6a}$$

Assuming that $M_0 \sim 0.06$ T, we infer that M can be on the order of 0.01 T. This is a value sufficiently large to be detected and used in applications. In particular, a nonzero magnetization provides for the possibility of natural ferromagnetic resonance. The resonance frequency can be estimated using the well-known Kittel formula for a cylindrical sample (assuming that the skin layer thickness is greater the cylinder radius):

$$\Omega/2\pi \sim 2\pi\gamma M_{\text{eff}} \sim 2 \text{ GHz}, \tag{7}$$

where $M_{\text{eff}} \sim (M/M_0)M_0$ and $\gamma \sim 2.8$ MHz/Oe.

Conclusions. (i) The result obtained for the magnetization (formula (6)) does not involve rotational (twisting and bulging) modes [2, 3]) determined previously for the homogeneous isotropic cylinder [2, 3].

(ii) The microwire remains magnetized in a zero external field; the residual magnetization depends on the technological parameter ρ°.

(iii) Such microwires possessing a residual magnetization can be used as memory elements in microelectronics.

(iv) By comparing the experimentally measured residual magnetization to the theoretical value, it is possible to determine the technological parameters ρ° and b using formula (7).

(v) The microwire with residual magnetization must naturally exhibit ferromagnetic resonance, which was probably observed in [8, 9].

Acknowledgments. One of the authors (S.A.B.) gratefully acknowledges support from the NATO Science for Peace Program.

REFERENCES

1. S. A. Baranov, J. Magn. Magn. Mater. **266**, 278 (2003).
2. W. F. Brown, *Micromagnetics* (Interscience, New York, 1963).
3. A. Aharoni and S. Shtrikman, Phys. Rev. **109**, 1522 (1958).
4. S. A. Baranov, V. S. Larin, A. V. Torcunov, *et al.*, in *Proceedings of the 4th International Workshop on Non-Crystalline Solids, Singapore, 1995*, Ed. by M. Vazquez and A. Hernando (World Scientific, Singapore, 1995), pp. 425–428.
5. S. A. Baranov, in *Proceedings of Conference on Barkhausen Effect and Similar Physical Phenomena, Izhevsk, 1995*, pp. 12–14.
6. A. Antonov, A. Dykhne, A. Lagar'kov, and N. Usov, Physica A **241**, 425 (1997).
7. S. A. Baranov, Élektron. Obrab. Mater., No. 3, 84 (2002).
8. S. A. Baranov, V. N. Berzhanskiĭ, S. K. Zotov, *et al.*, Fiz. Met. Metalloved. **67**, 73 (1989).
9. O. Acher, P.-M. Jacquart, and C. Boscher, IEEE Trans. Magn. **30**, 4542 (1994).

Translated by P. Pozdeev

Technical Physics Letters, Vol. 30, No. 12, 2004, pp. 991–994. Translated from Pis'ma v Zhurnal Tekhnicheskoĭ Fiziki, Vol. 30, No. 23, 2004, pp. 40–46.

Surface TM Wave Propagating at the Boundary of Isotropic Collisionless Plasma Moving at a Relativistic Velocity

S. N. Maryshev and N. S. Shevyakhov

Institute of Radio Engineering and Electronics (Ul'yanovsk Branch), Russian Academy of Sciences, Ul'yanovsk, Russia

e-mail: ufire@mv.ru

Received June 28, 2004

Abstract—The dispersion properties of a surface TM wave propagating at the boundary of isotropic collisionless plasma moving at a relativistic velocity are described. The phenomenon of aberration, whereby the wave normal of the surface wave deviates from the boundary plane and rotates in the direction of motion, takes place only in the laboratory frame. The subrelativistic motion of the plasma is manifested by a decrease in the cutoff frequency of the surface TM wave and by the appearance of a long-wavelength limit in the TM wave spectrum, which shifts toward shorter wavelengths with increasing plasma velocity, thus reflecting the indissoluble unity of space and time. © *2004 MAIK "Nauka/Interperiodica".*

Previously [1, 2], the behavior of surface TM waves was studied at the plasma–vacuum boundary of the type of a photoionization front propagating in a rarefied medium. Formally, this problem belongs to the class of parametric wave problems in electrodynamics [3] in which allowance for relativistic effects is substantial. However, in view of the finite lifetime of photoelectrons in a rarefied medium, the adopted method of formation of a sharp moving plasma–vacuum boundary (wherein the plasma was considered to be at rest) in fact excluded (within the framework of the geometric description of the interface) the possibility of taking relativistic effects into account, since the boundary exhibited considerable "swelling" as its velocity approached the speed of light c. As a result, the investigations were performed by method of comparison of the electrodynamic systems [4] on the basis of the Galilean transformation of coordinates.

From the relativistic standpoint, it would be of interest to consider the case when plasma moves together with the boundary and this boundary can be considered (irrespective of the reasons and methods of setting the plasma into motion) as a sharp interface independent of the plasma velocity component V along the normal to the plasma–vacuum interface. In this case, the laboratory ($x0yz$) and comoving ($\tilde{x}0\tilde{y}\tilde{z}$) frames of reference change roles in comparison to the situation considered in [1, 2]. Indeed, in the frame moving with (fixed at) the interface, the plasma is now at rest (rather than moving, as in [1, 2]). In contrast, in the laboratory frame (which was the rest frame in [1, 2]) plasma now moves at a velocity **V** along the y axis (Fig. 1).

In accordance with these considerations, a solution describing the surface TM wave at the plasma boundary in the comoving frame is known [5]. Thus, we have only to elucidate the character of changes in the electromagnetic fields and the wave dispersion upon moving to the laboratory frame according to relativistic rules [6].

For an isotropic collisionless plasma in the region $\tilde{y} < 0$, the electromagnetic field of the surface TM wave

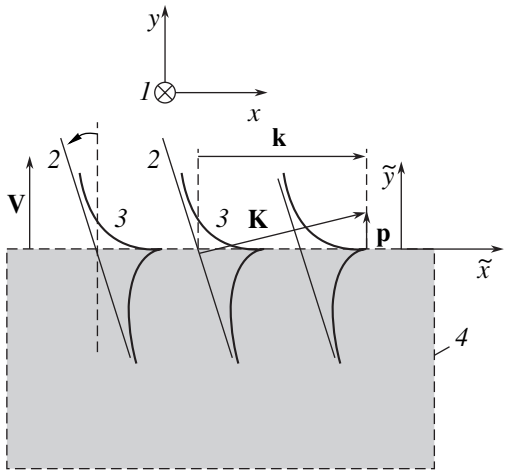

Fig. 1. Schematic diagram of the problem geometry and the surface TM wave propagating at the boundary of a moving plasma: (*1*) receiving antenna and related laboratory frame of reference; (*2*) deviated wave fronts; (*3*) field distribution in the surface TM wave; (*4*) plasma and comoving frame of reference.

1063-7850/04/3012-0991$26.00 © 2004 MAIK "Nauka/Interperiodica"

in the comoving frame is determined [5] by the nonzero components of the magnetic field strength in plasma,

$$\tilde{H}_z = A\exp[i(k\tilde{x} - \omega\tilde{t})]\exp(s\tilde{y}), \quad \tilde{y} < 0 \qquad (1)$$

and in vacuum,

$$\tilde{H}_z^{(0)} = B\exp[i(k\tilde{x} - \omega\tilde{t})]\exp(-s_0\tilde{y}), \quad \tilde{y} > 0, \qquad (2)$$

where k is the wavenumber of the surface TM wave, ω is the frequency in the comoving frame, and s and s_0 are the field decay coefficients with the distance from the interface in plasma and vacuum, respectively. The nonzero components of the electric field strength in plasma ($\tilde{E}_x$, $\tilde{E}_y$) and in vacuum ($\tilde{E}_x^{(0)}$, $\tilde{E}_y^{(0)}$) are obtained by substituting relations (1) and (2) into Maxwell's equations and the material relationships for plasma. Relations (1) and (2) must be considered together with the dispersion relationship

$$s_0 = -\frac{s}{\varepsilon} \qquad (3)$$

and the relations

$$\frac{\omega^2}{c^2}\varepsilon = k^2 - s^2, \quad \frac{\omega^2}{c^2} = k^2 - s_0^2, \qquad (4)$$

which follow from Eqs. (1) and (2) and Maxwell's equations.

Using formulas (3) and (4), the dispersion relation is usually written as [5]

$$k = \frac{\omega}{c}\sqrt{\frac{\varepsilon}{1+\varepsilon}}. \qquad (5)$$

By virtue of relation (3), the permittivity of plasma

$$\varepsilon = 1 - \frac{\Omega_e^2}{\omega^2} \qquad (6)$$

obeys the relation $\varepsilon < 0$, which is followed by a stronger condition that $1 + \varepsilon < 0$, which implies that the frequency spectrum is limited from above:

$$\omega < \frac{\Omega_e}{\sqrt{2}}, \quad \Omega_e^2 = \frac{4\pi e^2 n_0}{m_e}. \qquad (7)$$

Here, Ω_e is the plasma frequency, e is the electron charge, n_0 is the plasma density, and m_e is the rest mass of electron.

In order to move to the laboratory frame (where the four-dimensional spacetime coordinates and the field components are denoted by symbols without tildes), we use the Lorentz transformations [6]

$$\tilde{x} = x, \quad \tilde{y} = \frac{y - Vt}{\sqrt{1-\beta^2}}, \quad \tilde{z} = z, \quad \tilde{t} = \frac{t - y\beta/c}{\sqrt{1-\beta^2}}, \qquad (8)$$
$$\beta = \frac{V}{c},$$

and the corresponding formulas for relativistic transformation of the fields. As can be readily established, the general structure of the fields in the laboratory frame remains unchanged and the wave polarization type is retained: $\mathbf{H}$, $\mathbf{H}^{(0)} \parallel z$; $\mathbf{E}$, $\mathbf{E}^{(0)} \perp z$. The magnetic field strengths in the frames compared on a relativistic basis are related as

$$H_z = \frac{1 - iVs/\omega}{\sqrt{1-\beta^2}}\tilde{H}_z, \quad H_z^{(0)} = \frac{1 + iVs_0/\omega}{\sqrt{1-\beta^2}}\tilde{H}_z^{(0)}.$$

After a spacetime coordinate transformation in Eqs. (1) and (2) in accordance with relations (8), we obtain

$$H_z = H_0^+\exp[i(kx + py - \Omega t)]\exp[\Gamma(y - Vt)], \quad y < Vt, \qquad (9)$$

$$H_z^{(0)} = H_0^-\exp[i(kx + py - \Omega t)]\exp[-\Gamma_0(y - Vt)], \quad y > Vt, \qquad (10)$$

where $A = B \equiv H_0$ and

$$H_0^+ = \frac{H_0}{\sqrt{1-\beta^2}}\left(1 - i\frac{Vs}{\omega}\right), \quad H_0^- = \frac{H_0}{\sqrt{1-\beta^2}}\left(1 + i\frac{Vs_0}{\omega}\right).$$

Formulas (9) and (10) give the required representation of the surface TM wave in the laboratory frame. The quantity $p = \beta\Omega/c$ determines (by analogy with [1, 2]) the transverse component of the wave vector $\mathbf{K} = \mathbf{k} + \mathbf{p}$. However, the noncollinearity of the surface wave (which is related to the plasma motion) characterized by this quantity is manifested only in the laboratory frame and involves a lower (compared to [1, 2]) Doppler frequency increment $\Omega = \omega/\sqrt{1-\beta^2}$. Note, however, that the comparison to the results obtained in [1, 2] is correct only for $\beta \ll 1$, where the above differences are small and the main factor (owing to the relativistic contraction of length in the direction of plasma motion) is the increased boundary localization of the wave field according to the relations

$$\Gamma = \frac{s}{\sqrt{1-\beta^2}}, \quad \Gamma_0 = \frac{s_0}{\sqrt{1-\beta^2}}. \qquad (11)$$

We may suggest that, by analogy with dispersion relation (3), the coefficients Γ and Γ_0 are interrelated as well, but with a modified (relativistic) value of ε' replacing ε. It is necessary to warn against attempts to obtain ε' through a formal relativistic transformation of the quantities entering into formula (6), since the latter relation (by definition of the fields in the comoving frame) a priori corresponds to a nonrelativistic relation between the electric induction **D** and the electric field strength **E**.

In order to derive a relativistic dispersion relation, the simplest way is to use the relations (following from the Minkowski material relationships [6] by virtue of Eqs. (9) and (10)) between the tangential field components in the plasma (E_x, H_z) and in vacuum ($E_x^{(0)}, H_z^{(0)}$). Their ratio gives the impedances of plasma

$$Z = -\frac{iE_x}{H_z} = c\frac{\Gamma + ip}{\Omega}\frac{1-\varepsilon\beta^2}{\varepsilon + \beta^2(1-2\varepsilon)} - i\frac{(1-\varepsilon)\beta(1-\beta^2)}{\varepsilon + \beta^2(1-2\varepsilon)}$$

and vacuum

$$Z_0 = -\frac{iE_x^{(0)}}{H_z^{(0)}} = c\frac{ip - \Gamma_0}{\Omega}$$

for the surface TM wave, whose boundary matching condition $Z = Z_0$ determines the dispersion relation. In view of the complex character of Z and Z_0, this condition is formally equivalent to two equations. However, equality of the imaginary parts reduces to the above definition of p and, hence, is identically satisfied. Equality of the real parts yields

$$\Gamma_0 = -\frac{\Gamma}{\varepsilon'}, \quad \varepsilon' = \frac{\varepsilon}{1-\varepsilon\beta^2} + \beta^2\frac{1-2\varepsilon}{1-\varepsilon\beta^2}, \qquad (12)$$

which is a relativistic analog of Eq. (3). Using formulas (11), relations (4) can be written as

$$\frac{\omega^2}{c^2}\varepsilon = k^2 - \Gamma^2(1-\beta^2), \quad \frac{\omega^2}{c^2} = k^2 - \Gamma_0^2(1-\beta^2).$$

Then, using formulas (12), we obtain a dispersion relation replacing Eq. (5):

$$k = \frac{\omega}{c}\sqrt{\frac{\varepsilon - \varepsilon'^2}{1-\varepsilon'^2}}. \qquad (13)$$

Of course, the dispersion properties of the surface TM wave must be described in the spectral variables $\Omega, K = \sqrt{k^2 + p^2}$ or Ω, k (where k is invariant because longitudinal dimensions are retained in the course of plasma motion) in the laboratory frame of reference. Accordingly, ω in Eqs. (12) and (13) must be replaced by the quantity $\Omega = \omega\sqrt{1-\beta^2}$.

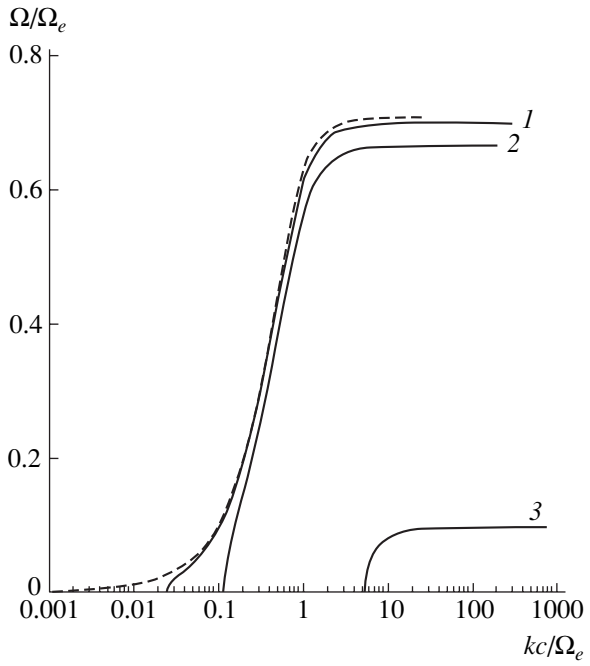

Fig. 2. Dispersion spectra of the surface TM wave propagating at the boundary of plasma moving at $\beta = 0.15$ (*1*), 0.3 (*2*), and 0.575 (*3*); the dashed curve shows $\Omega(k)$ for the immobile plasma.

Relation (13) directly suggests characteristic limitations imposed on the spectrum. Indeed, the pole k at $\varepsilon'^2 = 1$ determines the cutoff frequency

$$\Omega^* = \frac{\Omega_e}{\sqrt{2}}\frac{\sqrt{1-3\beta^2}}{1-\beta^2}.$$

A zero of the function $k = k(\Omega)$ at $\varepsilon = \varepsilon'^2$ determines the lower boundary of the wavenumbers k. The appearance of this boundary is a manifestation of the indissoluble unity of space and time in relativity, whereby a temporal limitation inherent in the surface TM waves (determined by the cutoff frequency) leads to an analogous spatial limitation with respect to the wavelength.

The above results are illustrated in Fig. 2, which shows the spectrum of a surface TM wave calculated in the subrelativistic region of $\beta < 1/\sqrt{3}$. The dashed curve corresponds to the case of an immobile interface, where $\beta = 0$ and $\Omega^* = \Omega_e/\sqrt{2}$, while curves *1–3* correspond to the gradually increasing plasma velocity $\beta = 0.15$, 0.3, and 0.575, respectively. In the limit as $\beta \longrightarrow 1\sqrt{3}$, the origin of the spectral branch (leaning on the abscissa axis) shifts toward shorter wavelengths. In this

limiting transition, the fields H_z and $H_z^{(0)}$ become static and negligibly small. It should also be noted that the absence of reverse branches of the dispersion curves (such as were described previously [1, 2]) is directly related to the fact that the plasma and interface in the case under consideration possess the same velocity.

Acknowledgments. This study was supported by the Federal Special Program "Integration," code B0107.

REFERENCES

1. N. S. Shevyakhov, Pis'ma Zh. Tekh. Fiz. **28** (12), 40 (2002) [Tech. Phys. Lett. **28**, 507 (2002)].
2. Yu. V. Gulyaev, G. A. Kolchina, V. G. Shjavrov, and N. S. Shevyakhov, Radiotekh. Élektron. (Moscow) **48**, 459 (2003).
3. V. N. Krasil'nikov, *Parametric Wave Phenomena in Classical Electrodynamics* (St. Petersburg State University, St. Petersburg, 1996) [in Russian].
4. M. A. Miller, Yu. M. Sorokin, and N. S. Stepanov, Usp. Fiz. Nauk **121**, 525 (1977) [Sov. Phys. Usp. **20**, 264 (1977)].
5. A. N. Kondratenko, *Surface and Bulk Waves in Organic Plasma* (Énergoatomizdat, Moscow, 1985) [in Russian].
6. W. Pauli, *The Theory of Relativity* (Pergamon Press, Oxford, 1958).

Translated by P. Pozdeev

Technical Physics Letters, Vol. 30, No. 12, 2004, pp. 995–997. Translated from Pis'ma v Zhurnal Tekhnicheskoĭ Fiziki, Vol. 30, No. 23, 2004, pp. 47–53.

Raman Spectra of Iron-Modified Amorphous Carbon

S. G. Yastrebov[a,*], V. I. Ivanov-Omskiĭ[a], V. A. Kosobukin[a], F. Dumitrache[b], and C. Morosanu[c]

[a] *Ioffe Physicotechnical Institute, Russian Academy of Sciences, St. Petersburg, 194021 Russia*
[b] *National Institute of Lasers, Plasma, and Radiation Physics, P.O. Box MG-36, R-76900 Bucharest, Romania*
[c] *National Institute of Materials Science, P.O. Box MG-7, R-76900 Bucharest, Romania*
** e-mail: yastrebov@mail.ioffe.ru*

Received June 25, 2004

Abstract—Raman spectra of amorphous carbon films containing encapsulated iron (a-C:Fe) have been measured in the frequency range 200–1000 cm^{-1}. The concentration of encapsulated iron atoms (3, 26, 38, and 54 at. %) was controlled by changing the relative areas of iron and graphite targets during the film deposition by RF magnetron sputtering and checked by Rutherford backscattering. The Raman spectra of a-C:Fe films display a series of almost equidistant bands spaced by approximately 110 cm^{-1}. This character of the spectrum is explained in terms of the atomic vibrations in short carbon nanotubes formed during the introduction of iron into an amorphous carbon matrix. © *2004 MAIK "Nauka/Interperiodica".*

In recent years, the process of encapsulation of ferromagnetic metal nanoclusters in thin films of amorphous carbon has been extensively studied [1–5] in view of the development of media for ultrahigh density data recording.

The introduction of a magnetic metal into a carbon matrix protects the metal nanoclusters from damage by the ambient medium and provides for a decrease in the exchange interaction between the neighboring magnetic particles that is necessary for data recording in separate particles.

We believe that an effective method for studying the structure of encapsulated materials and the character of atomic interactions in these particles is offered by the Raman scattering on phonons. This paper presents the results of investigations of the vibrational spectra of Raman scattering of amorphous carbon films doped with iron in a broad range of concentrations. Based on the obtained data, we will consider some peculiarities of a nanostructure formed in the carbon matrix and iron clusters.

The samples of amorphous carbon films modified with iron (a-C:Fe) were prepared by simultaneous RF magnetron sputtering of graphite and iron targets. The procedure of sample preparation and the Raman spectra of a-C:Fe films measured in the 1000–1800 cm^{-1} frequency range are described in detail elsewhere [6]. In this paper, we present and consider the Raman spectra of a-C:Fe films measured in the 200–1000 cm^{-1} frequency range. The concentration of iron encapsulated in each film was determined using Rutherford backscattering of protons.

The Raman spectra were measured (as described in more detail in [6]) on an Ocean Optics R-2001 spectrometer using a 500-mW laser radiation source operating at a wavelength of $\lambda = 785$ nm. The probing laser radiation was transmitted to a sample, and the response signal was transmitted to a detector with the aid of a fiber optic waveguide.

Figure 1 shows the pattern of Stokes lines in the Raman spectrum of a-C:Fe films with various atomic concentrations of iron. The spectra exhibit a sequence of quite well resolved equidistant lines whose positions are virtually independent of the iron concentration. Figure 2 shows a linear plot of the frequency positions of the spectral maxima versus their numbers (indicated by arrows in Fig. 1). In the region below 200 cm^{-1}, the observed Raman spectrum is significantly attenuated

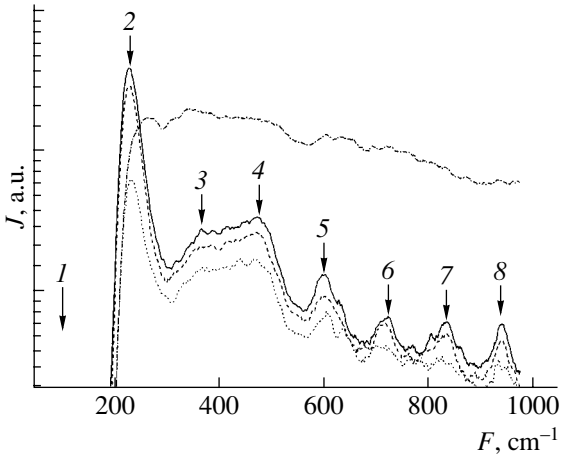

Fig. 1. Raman spectra of a-C:Fe films with various concentrations of iron (at. %): 3, 26, 38, 54 (top to bottom). Arrows indicate the Stokes lines.

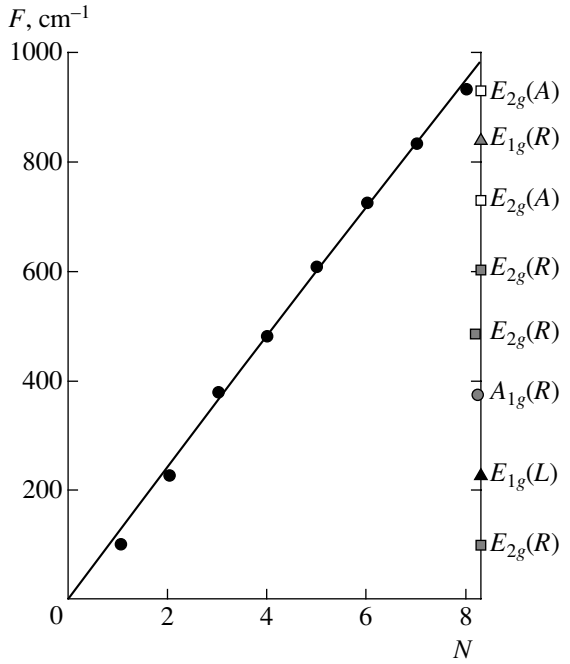

Fig. 2. A plot of the frequency versus line number in the Raman spectra of a-C:Fe films (line numbering as in Fig. 1). Black circles present the experimental data. Symbols on the right-hand vertical axis show the Raman-active mode frequencies calculated [9] for CNTs with a zigzag configuration consisting of $n = 7$ repeating units: (*L*) longitudinal mode; (*A*) axial mode; (*R*) radial mode (notation as in [9]).

because of filtration ("cutoff") of the exciting laser radiation. At a given iron content, the intensity of the line decreases with increasing Stokes frequency shift induced by the scattering. All lines increase in intensity with the iron concentration in a sample.

As is known, the Raman spectra of amorphous covalent samples, which are dependent on the density of vibrational states [7], exhibit no clear structure characteristic of the spectra of crystals and molecules. The Stokes lines in the Raman spectra presented in Fig. 1 are also weakly pronounced in the spectra of samples with low iron content (3 at. %), but significantly increase in intensity for elevated iron concentrations (>26 at. %). This fact indicates that the observed lines are actually due to iron encapsulated in a-C:Fe films.

When iron is encapsulated in amorphous carbon, the vibrational spectrum of such a sample observed in the Raman scattering mode can be modified under the action of two factors: (i) a change in the structure and spectrum of atomic vibrations of the carbon matrix and (ii) the appearance of vibrations of the atomic clusters of iron. In this context, it is necessary to note that, first, the bands in the Raman spectrum of a-C:Fe films are observed in the frequency range corresponding to the volume acoustic oscillations of carbon and iron and, second, the vibrational spectra of C and Fe atoms are significantly separated because of a significant difference in their masses and force constants. Indeed, the fundamental frequencies of atomic vibrations for iron fall below 350 cm^{-1} [14], so that these vibrations cannot be significantly manifested in the observed Raman spectrum (Fig. 1) extending up to 950 cm^{-1}. This interval, however, is completely covered by the spectrum of acoustic oscillations in carbon-based materials (diamond [8], graphite [9]), which extends up to 1200 cm^{-1}.

The introduction of a sufficiently large number of Fe atoms into an amorphous carbon matrix may lead to microstructurization in the bulk of a-C:Fe films, which is related to the formation of iron clusters and fractionation of the volume occupied by carbon. Spatial limitation of the vibrational modes in each material component must give rise to dimensional quantization (summation of bands) in the spectrum. Evidence for the spatial limitation of modes is provided by the fact that C and Fe possess significantly different acoustic impedances $Z_i = \rho_i s_i$ (ρ_i is the mass density and s_i is the sound velocity in the ith medium) determining the coefficient of reflection of acoustic waves, $R = |(Z_C - Z_{Fe})/(Z_C + Z_{Fe})|^2$, from the interface. Indeed, $Z_{Fe}/Z_C \approx 0.25$ (for $\rho_{Fe} = 7.87$ g/cm^3, $s_{Fe} = 7.87 \times 10^3$ cm/s [10] and $\rho_C = 1.8$ g/cm^3, $s_C = 8.7 \times 10^3$ cm/s [12]), and these parameters provide for a good evaluation of the regions of acoustic oscillations for iron and carbon.

The equidistant arrangement of lines observed in the Raman spectrum of a-C:Fe films suggests that these lines can be due to one-dimensional structures of finite lengths, in which the constant frequency shift is related to the dimensional quantization of the linear (acoustic) spectrum. In amorphous carbon, such one-dimensional structures may be represented by carbon nanotubes (CNTs) whose formation can be catalyzed by iron [13]. The spectrum of Raman-active vibrations of CNTs with various lengths and configurations was recently calculated by Dubay and Kresse [9]. Considering the spectrum presented in Fig. 1 from this standpoint, we may suggest that termination of the Raman spectrum above 950 cm^{-1} is consistent with the theory (for relatively short CNTs with configurations of the zigzag and armchair type). A more detailed comparative analysis of the observed spectra and theory [9] shows that there is a certain correspondence between the frequencies (Fig. 2) and the sets of Raman-active frequencies [9, Figs. 7a and 7b] calculated for CNTs with a zigzag configuration and a small number n of repeating units. This is illustrated in Fig. 2, where all the Raman-active vibrational modes calculated in [9] are shown for a zigzag CNT configuration with $n = 7$. A comparative analysis shows that the observed Raman spectrum can be due to a superposition of various modes (longitudinal, axial, and radial) excited in CNTs.

The frequencies of atomic vibrations in Fe clusters of rather large size can be evaluated through dimensional quantization of the spectrum of acoustic oscillations (only this type of vibration is possible in a monoatomic metal such as iron). Estimates using the above

parameters show that the frequencies of fundamental vibrations of Fe clusters do not exceed 350 cm^{-1}, which coincides with the boundary of the spectrum of acoustic oscillations for bulk iron [14]. Therefore, the Raman spectrum presented in Fig. 1 cannot be attributed to the fundamental vibrations of Fe clusters. Generally speaking, overtones and composite modes of Fe clusters might occur in the spectral range above 350 cm^{-1}. For example, experiments have shown that the Raman spectrum of Fe_2 molecules contains four lines with the frequencies 300, 600, 900, and 1200 cm^{-1} and the corresponding relative intensities 1 : 0.58 : 0.25 : 0.12 [15]. The first of these frequencies is assigned to the main tone and the others, to overtones. Although the spectrum of overtones in F_2 molecules also consists of equidistant lines, it is unlikely that this spectrum can account for the observed Raman spectrum of a-C:Fe films (Fig. 1). Indeed, the number of components observed in our spectrum is much greater, while the separation of lines is smaller than the analogous values for Fe_2. The lines of overtones were also found in the spectra of Fe_3 clusters [16], but these lines occur at much lower frequencies and have much lower intensities than the lines of overtones in the spectrum of Fe_2 clusters. Moreover, the appearance of overtones and composite frequencies in the Raman spectrum is possible in the presence of optical anharmonicity provided that certain selection rules are obeyed. We may also expect that, in the presence of various Fe clusters differing in shape and size, the overtones would possess a structureless spectrum only weakly manifested on the background of the Raman signal from amorphous carbon. Thus, the assignment of lines observed in the Raman spectra of our a-C:Fe films (Fig. 1) to the overtones of Fe clusters is unlikely. We suggest that the observed structure of the Raman spectrum is related to atomic vibrations in short CNTs, which may exist in the amorphous carbon matrix containing encapsulated iron.

In conclusion, we demonstrated that the Raman spectra of amorphous carbon films containing encapsulated iron display a sequence of equidistant lines situated in the spectral range of acoustic oscillations of the carbon matrix. The intensity of these lines increases with the atomic concentration of iron in the composite material. Our analysis showed that the observed Raman spectrum is most likely evidence of the formation of short CNTs in amorphous carbon whose vibrations are manifested in the first-order Raman spectra. This conclusion agrees with published data, according to which iron may catalyze the formation of CNTs, and with the results of calculations of the Raman-active mode frequencies of CNTs.

Acknowledgments. This study was supported by the Russian Foundation for Basic Research, project no. 03-02-16289a.

REFERENCES

1. T. Hayashi, S. Hirono, M. Tomita, *et al.*, Nature **381**, 772 (1996).
2. J. Jiao and S. Seraphin, J. Appl. Phys. **83**, 2442 (1998).
3. T. Cabioch, A. Naudon, M. Jaouen, *et al.*, Philos. Mag. B **79**, 501 (1999).
4. J.-J. Delaunay, T. Hayashi, M. Tomita, *et al.*, J. Appl. Phys. **82**, 2200 (1997).
5. T. K. Zvonareva, E. I. Ivanova, G. S. Frolova, *et al.*, Fiz. Tekh. Poluprovodn. (St. Petersburg) **36**, 734 (2002) [Semiconductors **36**, 695 (2002)].
6. S. G. Yastrebov, V. I. Ivanov-Omskiĭ, F. Dumitrache, and C. Morosanu, Fiz. Tekh. Poluprovodn. (St. Petersburg) **37**, 490 (2003) [Semiconductors **37**, 473 (2003)].
7. *Light Scattering in Solids*, Ed. by M. Cardona and G. Güntherodt (Springer, Heidelberg, 1975; Mir, Moscow, 1979).
8. W. Goldammer, W. Ludwig, W. Zierau, *et al.*, Phys. Rev. B **36**, 4624 (1987).
9. O. Dubay and G. Kresse, Phys. Rev. B **67**, 035401 (2003).
10. *Dictionary of Physics*, Ed. by B. A. Vvedenskiĭ (Sov. Éntsiklopediya, Moscow, 1962), Vol. 2, p. 11.
11. J. Minkiewicz, G. Shirane, and R. Nathans, Phys. Rev. **162**, 528 (1967).
12. A. J. Bullen, K. E. O'Hara, D. G. Cahill, *et al.*, J. Appl. Phys. **88**, 6317 (2000).
13. Y. Fujiwara, H. Takegava, H. Sato, *et al.*, J. Appl. Phys. **95**, 7118 (2004).
14. A. Del Corso and S. Gironcoli, Phys. Rev. B **62**, 273 (2000).
15. M. Moskovits and D. P. DiLella, J. Chem. Phys. **73**, 4917 (1980).
16. T. L. Haslett, K. A. Bosnick, S. Fedrigo, *et al.*, J. Chem. Phys. **111**, 6456 (1999).

Translated by P. Pozdeev

Technical Physics Letters, Vol. 30, No. 12, 2004, pp. 998–1001. Translated from Pis'ma v Zhurnal Tekhnicheskoĭ Fiziki, Vol. 30, No. 23, 2004, pp. 54–61.

Generalized Synchronization of Chaotic Oscillators as a Partial Case of Time Scale Synchronization

A. A. Koronovskiĭ* and A. E. Khramov**

State Scientific Center "College," Saratov State University, Saratov, Russia

*e-mail: * alkor@cas.ssu.runnet.ru; ** aeh@cas.ssu.runnet.ru*

Received April 20, 2004

Abstract—Two coupled dynamical systems of the Rössler type are studied, and it is shown that the generalized synchronization regime can be considered as a partial case of the time scale synchronization process. © *2004 MAIK "Nauka/Interperiodica".*

The process of chaotic synchronization of dynamical systems has been extensively studied in recent years [1–3]. This phenomenon is both of basic importance and of considerable practical interest (in particular, in biology [4, 5], data transfer by means of deterministic chaotic oscillations [6], etc.). According to modern classification schemes, there are several types of chaotic synchronization, including generalized [7, 8], phase [9, 10], lag [11], and complete [12] synchronization. Recently [13, 14], it was shown that the phase, lag, and complete synchronization regimes are closely related, essentially manifestations of the same type of synchronous dynamics of the time scale of coupled chaotic oscillators, whereby the character of synchronization (phase, lag, or complete) is determined by the number of synchronized time scales introduced by means of a continuous wavelet transform [15].

In this Letter, we show that the regime of generalized synchronization is also a particular case of the synchronous behavior of time scales of a system of coupled chaotic oscillators.

The notion of generalized synchronization [7, 8] introduced for unidirectionally coupled dynamical systems implies that there exists a certain function $\mathbf{F}[\cdot]$ relating the states of chaotic oscillators such that $\mathbf{x}_2(t) = \mathbf{F}[\mathbf{x}_1(t)]$. This functional relation can be very complicated, but there are methods capable of detecting the phenomenon of synchronization between unidirectionally coupled chaotic oscillators (see, e.g., [7, 16, 17]).

The time scale s and the associated phase $\phi_s(t)$ of a chaotic signal $\mathbf{x}(t)$ are defined by means of the continuous wavelet transform

$$W(s, t_0) = \int_{-\infty}^{+\infty} x(t)\psi^*_{s, t_0}(t)dt, \qquad (1)$$

where $\psi_{s, t_0}(t)$ is the wavelet function (the asterisk denotes complex conjugation) obtained from the base wavelet $\psi_0(t)$:

$$\psi_{s, t_0}(t) = \frac{1}{\sqrt{s}}\psi\left(\frac{t - t_0}{s}\right). \qquad (2)$$

The time scale s determines the width of the $\psi_{s, t_0}(t)$ wavelet, while the parameter t_0 is the shift of the wavelet function along the time axis. For the base wavelet, we use the Morlet wavelet

$$\psi_0(\eta) = \frac{1}{\sqrt[4]{\pi}}\exp(j\Omega_0\eta)\exp\left(\frac{-\eta^2}{2}\right). \qquad (3)$$

Selection of the wavelet parameter $\Omega_0 = 2\pi$ provides for the relation $s \sim 1/f$ between the time scale s of the wavelet transform and the frequency f of the Fourier transform. It is also convenient to introduce the integral distribution of the wavelet energy with respect to the time scales, which is defined as

$$\langle E(s)\rangle = \int |W(s, t_0)|^2 dt_0. \qquad (4)$$

Let $\mathbf{x}_{1, 2}(t)$ be the time series generated by two coupled chaotic oscillators. If there exists a certain interval of time scales $[s_m; s_b]$ such that, for any time scale $s \in [s_m; s_b]$, the condition of phase entrainment

$$|\phi_{s1}(t) - \phi_{s2}(t)| < \text{const} \qquad (5)$$

is satisfied and the energy fraction of the wavelet spectrum in this interval is nonzero,

$$E_{snhr} = \int_{s_m}^{s_b} \langle E(s)\rangle ds > 0, \qquad (6)$$

then the time scales $s \in [s_m; s_b]$ are synchronized and the chaotic oscillators occur in the regime of time scale synchronization.

1063-7850/04/3012-0998$26.00

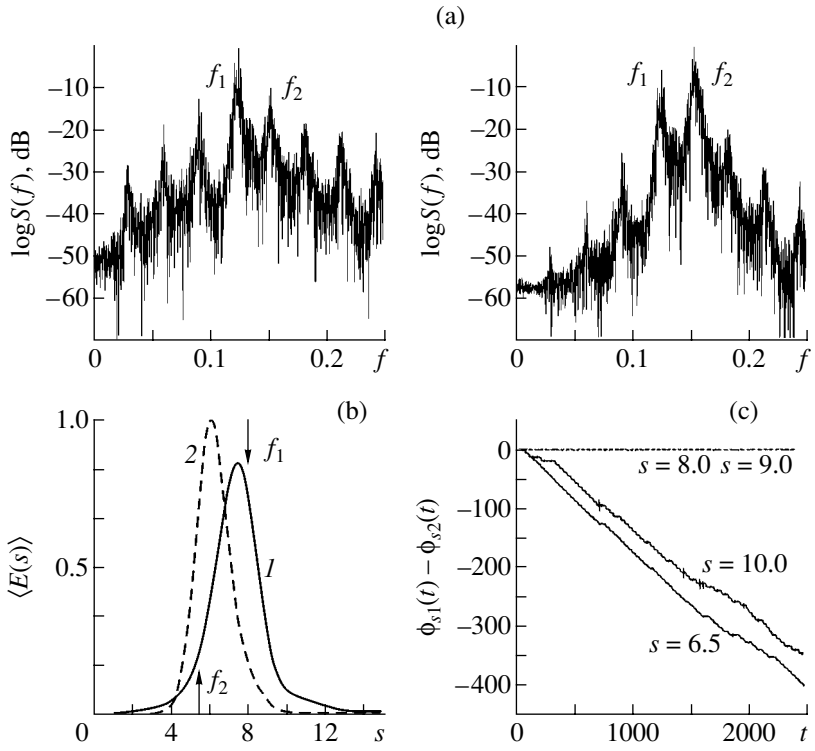

Fig. 1. Coupled chaotic Rössler systems (7): (a) logarithmic Fourier spectra log$S(f)$ of the master (left) and slave (right) systems with a coupling parameter of $\varepsilon = 0.2$; (b) normalized energy distribution $\langle E(s)\rangle$ in the wavelet spectrum of the master (*1*) and slave (*2*) system; arrows indicate the time scales corresponding to the main frequencies $f_1 = 0125$ and $f_2 = 0.154$; (c) phase difference $\phi_{s1}(t) - \phi_{s2}(t)$ for various time scales. Plots in (a, b) correspond to the regime of generalized synchronization.

In order to analyze this situation in more detail for two unidirectionally coupled oscillators occurring in the regime of generalized synchronization, let us consider two coupled Rössler systems,

$$\begin{aligned}
\dot{x}_1 &= -\omega_1 y_1 - z_1, \\
\dot{y}_1 &= \omega_1 r_1 + a y_1, \\
\dot{z}_1 &= p + z_1(x_1 - c), \\
\dot{x}_2 &= \omega_2 y_2 - z_2 + \varepsilon(x_1 - x_2), \\
\dot{y}_2 &= \omega_2 x_2 + a y_2, \\
\dot{z}_2 &= p + z_2(x_2 - c),
\end{aligned} \tag{7}$$

where $\mathbf{x}_1 = (x_1, y_1, z_1)^T$ and $\mathbf{x}_2 = (x_2, y_2, z_2)^T$ are the state vectors of the first (master) and second (slave) systems, respectively, and ε is the coupling parameter. The values of the control parameters are selected as follows: $\omega_1 = 0.8$, $\omega_2 = 1.0$, $a = 0.15$, $p = 0.2$, $c = 10$, and $\varepsilon = 0.2$. It is known that two coupled Rössler systems with such parameters occur in the regime of generalized synchronization (for more detail, see [8]), while the phase synchronization does not take place.

How it is possible that the phase synchronization regime is not established despite the fact that generalized synchronization takes place becomes clear from an analysis of the behavior of the time scales. Figure 1a shows the Fourier spectra of the coupled chaotic oscillators. As can be seen, the spectra contain the main spectral components with the frequencies $f_1 = 0125$ and $f_2 = 0.154$. An analysis of the behavior of the time scales shows that the time scales $s_1 = 1/f_1 = 8$ of the coupled oscillators corresponding to the frequency f_1 (and the scales close to s_1) are synchronized, whereas the time scales $s_2 = 1/f_2 \simeq 6.5$ corresponding to the frequency f_2 (and the scales close to s_2) exhibit nonsynchronous behavior (Fig. 1b). Since both of these frequencies present in the spectrum in some manner influence the instantaneous phase of the chaotic signal introduced (for more detail, see [9]), while the time scales corresponding to f_2 are not synchronized, the phenomenon of phase synchronization is not observed (see also [19]).

The reason for such behavior of the time scales becomes clear from an analysis of the wavelet spectra $\langle E(s)\rangle$ of both Rössler systems (Fig. 1). Indeed, the time scale of the master system is characterized by a large energy, while the fraction of the energy corresponding to this time scale in the spectrum of the slave system is rather small. For this reason, the master system induces its dynamics in the slave system over the time scale s_1. However, the fraction of energy corresponding to the

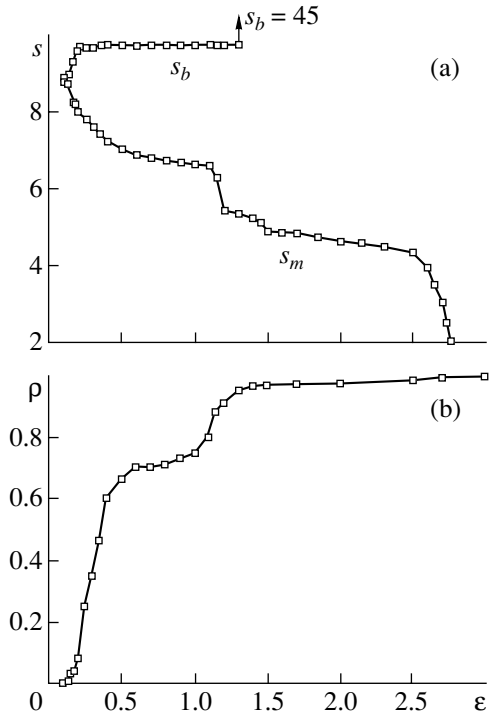

Fig. 2. Plots of (a) the lower (s_m) and upper (s_b) boundaries of the interval of synchronized time scales and (b) the relative energy ρ corresponding to the interval of synchronized time scales versus the coupling parameter ε for two coupled Rössler systems.

time scale s_2 in the master system is small, while that in the slave system is large and the former system cannot induce the corresponding phase dynamics in the latter system, so that the time scales s_2 remain nonsynchronized. As the coupling parameter grows, the interval of synchronized time scales $[s_m, s_b]$ expands and, when all time scales are synchronized, the combined system exhibits lag synchronization.

This pattern of synchronization of the time scales is qualitatively illustrated in Fig. 2a, which shows plots of the upper (s_b) and lower (s_m) boundaries versus the coupling parameter ε for the interval of time scales satisfying synchronization conditions (5) and (6). The regime of chaotic synchronization is set at $\varepsilon \simeq 0.1$, for which a certain interval $\Delta s = s_b - s_m$ appears featuring the phase entrainment. As the ε value increases, the interval of synchronized time scales Δs increases and, eventually, all time scales become synchronized (lag synchronization).

A convenient characteristic for the description of the degree of synchronization of two chaotic subsystems is offered by the relative energy of the wavelet spectrum corresponding to the synchronized time scales [13]:

$$\rho = \int_{s_m}^{s_b} E(s)ds \Big/ \int_0^{\infty} E(s)ds, \qquad (8)$$

where $E(s)$ is the integral distribution of the wavelet spectrum energy with respect to the time scales determined according to formula (4). The corresponding dependence is presented in Fig. 2b. As can be seen, an increase in the coupling parameter ε is accompanied by an increasing fraction of the energy of the chaotic process corresponding to the synchronized time scales. For large coupling parameters ($\varepsilon > 1.5$), the relative energy $\rho(\varepsilon)$ tends to unity, which implies that almost all the energy of chaotic oscillations is concentrated in the interval of synchronized time scales and that the system, as was noted above, is in the regime of lag synchronization. In other words, the behavior of coupled chaotic oscillators in the regime of generalized synchronization is, from the standpoint of time scale synchronization, fully analogous to their behavior in the case of phase synchronization (see [13, 14]).

Thus, various regimes of chaotic synchronization (phase, generalized, lag, and complete synchronization) are determined by the synchronous behavior of a certain interval in the time scales. In other words, we may ascertain that coupled chaotic oscillators exhibit a common type of synchronous behavior called time scale synchronization, whereby all the other types of chaotic synchronization are particular cases of the time scale synchronization.

Acknowledgments. This study was supported by the Federal Special Program "Integration," the Program of Support for Leading Scientific Schools in Russia, and the Science and Education Center "Nonlinear Dynamics and Biophysics" at Saratov State University (sponsored by the US Civilian Research and Development Foundation for the Independent States of the Former Soviet Union, CRDF award No. REC-006). One of the authors (A.E.H.) gratefully acknowledges support from the "Dynasty" Foundation and the International Center for Basic Research in Physics (Moscow).

REFERENCES

1. V. S. Afraĭmovich, V. I. Nekorkin, G. V. Osipov, and V. D. Shalfeev, in *Stability, Structures, and Chaos in Nonlinear Synchronization Networks*, Ed. by A. V. Gaponov-Grekhov and M. I. Rabinovich (Inst. Prikl. Fiz., Akad. Nauk SSSR, Gorki, 1989) [in Russian].
2. E. Rosa, W. B. Pardo, C. M. Ticos, *et al.*, Int. J. Bifurcation Chaos Appl. Sci. Eng. **10**, 2551 (2000).
3. D. I. Trubetskov and A. E. Hramov, Radiotekh. Élektron. (Moscow) **48**, 116 (2003).
4. V. S. Anishchenko, A. G. Balanov, N. B. Janson, *et al.*, Int. J. Bifurcation Chaos Appl. Sci. Eng. **10**, 2339 (2000).
5. R. C. Elson *et al.*, Phys. Rev. Lett. **81**, 5692 (1998).
6. A. S. Dmitriev and A. I. Panas, *Dynamical Chaos. New Information Facilities for Communication Systems* (Fizmatlit, Moscow, 2002) [in Russian].
7. N. F. Rulkov, M. M. Sushchik, L. S. Tsimring, and H. D. I. Abarbanel, Phys. Rev. E **51**, 980 (1995).

8. L. Kocarev and U. Parlitz, Phys. Rev. Lett. **76**, 1816 (1996).
9. A. Pikovsky, M. Rosenblum, and J. Kurths, *Synchronization: A Universal Concept in Nonlinear Sciences* (Cambridge Univ. Press, 2001).
10. V. S. Anshchenko, V. Astakhov, A. Neiman, T. Vadivasova, and L. Schimansky-Geier, *Nonlinear Dynamics of Chaotic and Stochastic Systems. Tutorial and Modern Developments* (Springer-Verlag, Heidelberg, 2001).
11. M. G. Rosenblum, A. S. Pikovsky, and J. Kurths, Phys. Rev. Lett. **78**, 4193 (1997).
12. L. M. Pecora and T. L. Carroll, Phys. Rev. A **44**, 2374 (1991).
13. A. A. Koronovskiĭ and A. E. Hramov, Pis'ma Zh. Éksp. Teor. Fiz. **79**, 391 (2004) [JETP Lett. **79**, 316 (2004)].
14. A. A. Koronovskiĭ, D. I. Trubetskov, and A. E. Hramov, Dokl. Akad. Nauk **395**, 143 (2004) [Dokl. Phys. **49**, 143 (2004)].
15. A. A. Koronovskiĭ and A. E. Hramov, *Continuous Wavelet Analysis and Its Applications* (Fizmatlit, Moscow, 2003) [in Russian].
16. H. D. I. Abarbanel, N. F. Rulkov, and M. Sushchik, Phys. Rev. E **53**, 4528 (1996).
17. L. M. Pecora, T. L. Carroll, and J. F. Heagy, Phys. Rev. E **52**, 3420 (1995).
18. Z. Zheng and G. Hu, Phys. Rev. E **62**, 7882 (2000).
19. T. E. Vadivasova and V. S. Anishchenko, Radiotekh. Élektron. (Moscow) **49**, 76 (2004).

Translated by P. Pozdeev